

BRILLOUIN SCATTERING IN  $\text{EU}^{3+}$ -DOPED  
ALKALI-SILICATE GLASSES

By

GEORGE HENRY GANGWERE

Bachelor of Science  
Southwest Missouri State University  
Springfield, Missouri  
1976

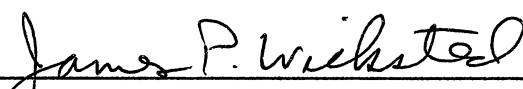
Master of Science  
Kansas State University  
Manhattan, Kansas  
1981

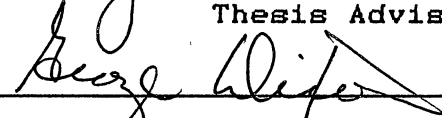
Submitted to the Faculty of the  
Graduate College of the  
Oklahoma State University  
in partial fulfillment of  
the requirements for  
the Degree of  
DOCTOR OF PHILOSOPHY  
December, 1990

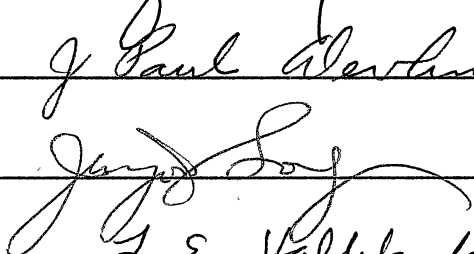
Thesis  
1990 D  
G 1976  
1972


BRILLOUIN SCATTERING IN  $\text{Eu}^{3+}$ -DOPED  
ALKALI-SILICATE GLASSES

Thesis Approved:

  
\_\_\_\_\_  
Thesis Adviser

  
\_\_\_\_\_  
of Paul Alvarini

  
\_\_\_\_\_  
L. E. Valukuta

  
\_\_\_\_\_  
Dean of the Graduate College

## ACKNOWLEDGMENTS

I wish to express my sincere gratitude to my dissertation advisor, Dr. Jim Wicksted, for his advice, guidance, and patience throughout this project. I would also like to thank Dr. G. S. Dixon, Dr. L. E. Halliburton, Dr. J. J. Song, and Dr. J. P. Devlin for serving on my dissertation committee.

I want to thank my parents for their support and encouragement throughout my student years. And to my wife Patricia, for her love and encouragement over the last several years.

Financial support for this work was provided in part by a grant from the Army Center for Night Vision and Electro-optics No. DAAB07-88-C-F407.

## TABLE OF CONTENTS

Chapter	Page
I. INTRODUCTION. . . . .	1
Previous Studies . . . . .	3
Present Study. . . . .	5
II. EXPERIMENTAL APPARATUS AND PROCEDURE. . . . .	7
Sample Preparation . . . . .	7
Apparatus. . . . .	8
Procedure. . . . .	11
Brillouin Shifts. . . . .	17
Intensity Measurements. . . . .	21
III. THEORETICAL ANALYSIS. . . . .	32
Equations of Motion. . . . .	32
The Phonon Frequency and Wavevector. . . . .	35
The Rayleigh Ratio . . . . .	37
Intensities Relative to Fused Quartz . . . . .	48
IV. EXPERIMENTAL RESULTS AND ANALYSIS . . . . .	53
Brillouin Shifts, Velocities and Elastic Constants. . . . .	53
Photo-Elastic Constants. . . . .	61
Optical Absorption . . . . .	68
V. DISCUSSION AND SUMMARY. . . . .	71
Fused Quartz . . . . .	71
Alkali Silicate Glasses. . . . .	72
Visible Absorption . . . . .	76
Elastic Constants. . . . .	77
Photo-Elastic Constants. . . . .	78
The Landau-Placzek Ratio . . . . .	89
The Density Derivative of the Optical Dielectric Constant. . . . .	89
Summary. . . . .	96
REFERENCES . . . . .	98

Chapter	Page
APPENDIX A - THE COMPUTER ANALYSIS PROGRAM . . . . .	101
Background . . . . .	101
Peak Channel . . . . .	102
Peak Area. . . . .	102
Full-Width at Half-Maximum . . . . .	103
The Centroid . . . . .	103
The Average Area . . . . .	104
The Free Spectral Range and Finesse. . . . .	104
The Brillouin Shift and Plate Separation . . . . .	105
Listing of the Program . . . . .	106
APPENDIX B - APPROXIMATIONS AND CORRECTIONS TO THE INTENSITY RATIO . . . . .	111
The Volume Ratio . . . . .	111
Solid Angle Correction . . . . .	116
Back Reflection. . . . .	120
Uncertainty in the Velocity. . . . .	122

## LIST OF TABLES

Table	Page
I. Composition of Glass Samples (Mole %) . . . . .	2
II. Results of Fused Quartz Measurements. . . . .	14
III. Densities, Refractive Index and Color of the Glasses and Tolune . . . . .	16
IV. Absorption Coefficients and Regression Analysis Parameters . . . . .	27
V. Brillouin Intensities Relative to Fused Quartz. . . . .	31
VI. Velocities, Polarizations and Brillouin Scattering Tensors for Glasses. . . . .	43
VII. Room Temperature Brillouin Shifts . . . . .	55
VIII. Room Temperature Sound Velocities . . . . .	55
IX. Room Temperature Elastic Constants. . . . .	57
X. Bulk Modulus, Young's Modulus and Poisson's Ratio . . . . .	60
XI. Room Temperature Photo-Elastic Constants. . . . .	62
XII. Landau-Placzek Ratios and Attenuation Coefficients. . . . .	65
XIII. Figures-of-Merit. . . . .	67
XIV. Quantities Used in the Expressions for the Photo-Elastic Constants . . . . .	82
XV. Numerical Values Found in the Expressions for the Photo-Elastic Constants . . . . .	82
XVI. Values for the Density Derivative of the Dielectric Constant . . . . .	92

Table	Page
XVII. Strain Polarizability Constants . . . . .	95
XVIII. Correction Factors. . . . .	117



## LIST OF FIGURES

Figure	Page
1. Experimental Setup for Brillouin Scattering Experiments. . . . .	9
2. Brillouin Spectrum of the $\text{Rb}_2\text{O-SiO}_2$ Glass. . . . .	12
3. Three Orders of the Vertical-Unpolarized Brillouin Spectrum of Fused Quartz. . . . .	18
4. Illustration of the Method used to Determine the Brillouin Shifts. . . . .	19
5. Top View of the Sample Showing the Distance Traveled by the incident and Scattered Light . . . . .	26
6. Natural Logarithm Versus $h$ for the $\text{K}_2\text{O-SiO}_2$ Glass Sample and for Fused Quartz . . . . .	29
7. The Brillouin Scattering Process. . . . .	36
8. Brillouin Scattering Geometry . . . . .	41
9. Polarized Brillouin Scattering Spectra of the $\text{Na}_2\text{O-SiO}_2$ Glass . . . . .	45
10. Polarized Brillouin Spectra of the $\text{Na}_2\text{O-SiO}_2$ Glass. . . . .	46
11. Top View of the Sample Showing the Incident, Transmitted, and Scattered Light. . . . .	49
12. Elastic Constants Versus the Molecular Weight of the Glasses . . . . .	58
13. Photo-Elastic Constants Versus the Molecular Weight of the Glasses . . . . .	62
14. Natural Logarithm of $I_s/I_0$ Versus $h$ . . . . .	69

Figure	Page
15. Two-Dimensional Schematic of the Structures of Crystalline $\text{SiO}_2$ and $\text{SiO}_2$ Glass. . . . .	73
16. The Radial Distribution Function and Two-Dimensional Schematic of the Structures of $\text{SiO}_2$ Glass and $\text{M}_2\text{O-SiO}_2$ Glass. . . . .	86
17. Top View of the Scattering Volume . . . . .	113
18. Top View of the Sample Showing the Collection Solid Angle. . . . .	118
19. The Top View of the Sample for the Calculation of the Uncertainty in the Velocity. . . . .	124

## CHAPTER I

### INTRODUCTION

The focus of this study centers around five different silicate based glasses. The glasses are predominately amorphous  $\text{SiO}_2$  with the addition of three network modifiers, two of which are the same in each sample, and the rare-earth  $\text{Eu}^{3+}$  as a dopant ion. One of three modifier ions of each glass was changed through the series of alkali-metal ions Li, Na, K, Rb, and Cs. Table I lists the five glasses with their chemical composition in mole %.

The purpose of the modifying ions, in most cases, is to modify the structure of the glass in a way suitable for a specific application. Some possible applications are discussed below. The  $\text{Eu}^{3+}$  dopant ions are introduced as a means of producing very localized structural changes that allow for the creation of laser induced refractive-index gratings. This topic is discussed in more detail later.

In the last twenty years there has been some interest in the use of crystals and glasses as laser hosts, acousto-optic light modulators, opto-optical deflectors (Sincerbox and Rossen (1983)), and photo-optical switches (Tanaka and Odajima (1981)) to mention just a few. (See Pinnow (1972) and references within for additional

TABLE I  
COMPOSITION OF GLASS SAMPLES (MOLE %)

Sample ID #	Network Formers	Network Modifiers	Eu Content
K-2620	70.0 SiO <sub>2</sub>	15.0 Li <sub>2</sub> O 5.0 ZnO 5.0 BaO	5.0 Eu <sub>2</sub> O <sub>3</sub>
K-2619	70.0 SiO <sub>2</sub>	15.0 Na <sub>2</sub> O 5.0 ZnO 5.0 BaO	5.0 Eu <sub>2</sub> O <sub>3</sub>
K-2721	70.0 SiO <sub>2</sub>	15.0 K <sub>2</sub> O 5.0 ZnO 5.0 BaO	5.0 Eu <sub>2</sub> O <sub>3</sub>
K-2756	70.0 SiO <sub>2</sub>	15.0 Rb <sub>2</sub> O 5.0 ZnO 5.0 BaO	5.0 Eu <sub>2</sub> O <sub>3</sub>
K-2757	70.0 SiO <sub>2</sub>	15.0 Cs <sub>2</sub> O 5.0 ZnO 5.0 BaO	5.0 Eu <sub>2</sub> O <sub>3</sub>

applications). In all of these applications, the elasto-optic effect plays an important role. The elasto-optic effect is the coupling of the index of refraction to the mechanical strain in the glass (Nye (1981)). The mechanical strain in the glass can be produced in a number of ways. It can be permanently frozen-in at the time of formation of the glass or it can be caused by acoustic phonon waves either thermal in origin or artificially introduced through a transducer. The mechanical strain can also be introduced through laser induced structural changes of which thermal lensing and refractive index gratings are examples. In any case, an incident laser beam will interact with the changes in the local index of refraction.

Some of the applications involving refractive index gratings in rare-earth doped glasses using four-wave mixing techniques include holographic storage, demultiplexing multifrequency laser beams, and signal modulation (Behrens and Powell et al. (1989)).

#### Previous Studies

Four-wave mixing techniques have been used to produce permanent and transient refractive-index gratings in the same glasses used in this study and listed in Table I (Behrens et al. (1989) and Gang and Powell (1985)). The gratings were produced by splitting the output of a laser beam and crossing the two beams inside the sample. The

production of the gratings can be verified by directing a probe laser beam, of different wavelength than the write beams, into the region of the sample where the gratings were produced. The probe beam is then Bragg diffracted and the scattered intensity measured with a photomultiplier tube. It has been shown (Behrens et al. (1989)) that the scattering efficiency from these induced gratings is dependent on the  $\text{Eu}^{3+}$  concentration, with no grating produced in those samples with little or no  $\text{Eu}^{3+}$  dopant. Also, it has been found that the scattering efficiency decreases as the modifier ion is systematically changed from Li to Cs even though the  $\text{Eu}^{3+}$  content is believed to be the same in each sample.

The effect the modifying ions and  $\text{Eu}^{3+}$  ions have on the scattering efficiency was explained using a simple double-minimum potential well model where both the network former and the modifier ions move in the environment of the  $\text{Eu}^{3+}$  ion creating a double well for the electronic levels of the  $\text{Eu}^{3+}$  ion. During the creation of the gratings, the write beams, which are in resonance with the  ${}^7\text{F}_0 \rightarrow {}^5\text{D}_2$  absorption transition of the  $\text{Eu}^{3+}$  ion excite the ions into a higher energy state. The ions decay by way of the non-radiative transition  ${}^5\text{D}_2 \rightarrow {}^5\text{D}_0$  which produces several high energy phonons. The resultant local heating caused by the phonons is then believed to be responsible for the structural changes that produce the gratings.

Additional information on the formation of the

gratings and of the structure of the glasses can be obtained from Raman and Brillouin scattering experiments. Raman scattering experiments have already been done in some of these glasses (Durville et al. (1987)) but to date no Brillouin scattering experiments have been reported.

Schroeder (1980), studied the index of refraction/density relationship of the photo-elastic constants for several families of binary and ternary silicate glasses using Brillouin scattering. He found that the theoretical expressions for the photo-elastic constants as derived by Mueller (1935), Carleton (1972), and Sipe (1978) could qualitatively account for the changes in the photo-elastic constants as the amount of alkali-oxide concentration was changed in the host glass. From the measured values of the photo-elastic constants  $P_{12}$  and  $P_{44}$ , the density derivative of the optical dielectric constant  $(\rho \frac{\partial \epsilon}{\partial \rho})$  was calculated and compared with that value predicted by several different theories. It was found that the Carleton model was able to provide an upper and lower bound to the measured value of the density derivative.

#### Present Study

We report in this dissertation the results of Brillouin scattering experiments in the same glasses as was used in the four-wave mixing experiments mentioned in the last section. The elastic constants and photo-elastic constants for these glasses were measured at room

temperature. The photo-elastic constants were measured by comparing the scattering intensity of the longitudinal acoustic (LA) and transverse acoustic (TA) peaks to that of fused quartz. (Fused quartz with its known photo-elastic constants was used as a standard scatterer).

The measured values of the photo-elastic constants are compared to Carleton's theoretical expressions for photo-elastic constants in glasses. The photo-elastic constants were also used to calculate the density derivative of the optical dielectric constant, mentioned in the last section, for the five glasses listed in Table I. Our results are compared with the Lorentz-Lorenz and the Drude expressions for the density derivative. The strain polarizability constant, a quantity that measures the amount of strain induced polarizability in the glass, was calculated for each sample. The figures-of-merit and Landau-Placzek ratios of the glasses as well as Young's modulus, Poisson's ratio, and acoustic attenuation coefficients are also reported.



## CHAPTER II

### EXPERIMENTAL APPARATUS AND PROCEDURE

In this chapter the equipment used in the Brillouin scattering experiments will be discussed and the procedure outlined. But first, a few words on sample preparation.

#### Sample Preparation

The glass samples listed in Table I on page 2, were prepared by the National Bureau of Standards and were provided to us by Dr. Richard C. Powell of the Physics Department of Oklahoma State University. The samples were cut from larger pieces so that two of the narrow width faces intersected at a 60° prism angle. This facilitated the measurement of the index of refraction. (Cutting the samples in this way did not affect the scattering experiments since these experiments were done on the bottom half of the samples where they were rectangular in shape). Except for the 60° prism angle, the samples were cut into a near rectangular shape of dimensions of about  $1 \times 0.5 \text{ cm}^3$ . Each sample was then polished by hand to optical quality.

The fused quartz sample, used as the standard, was cut from a circular disk part of a stock of disks normally

used for high quality windows. After cutting, the sample was repolished to optical quality. Liquid toluene from Fisher Scientific was used to calibrate the fused quartz standard. Before using, the toluene was filtered several times using filter paper to remove sources of elastic scattering.

### Apparatus

Figure 1 shows the experimental setup used in the measurements of the elastic constants and the photo-elastic constants of the  $\text{Eu}^{3+}$ -doped silicate glasses.

All of the experiments were done at room temperature of about  $25^{\circ}\text{C}$ . On any given day, the temperature in the room was stable to less than about  $\pm 1^{\circ}\text{C}$ . However, over a period of more than a year, the temperature varied by about  $\pm 3^{\circ}\text{C}$  due to the effects of air conditioning and heating. Since the Brillouin scattering intensity is proportional to the absolute temperature this fluctuation of about  $3^{\circ}\text{C}$  amounts to an uncertainty of around  $\pm 1\%$ . The elastic constants, on the other hand, are independent of temperature in this temperature range.

The single mode output of a Spectra-Physics model 2020 argon-ion laser operating at  $5145\text{\AA}$ , was focused into the sample to be studied by 50cm focal length lens. The power used in these experiments depended on the situation and the type of experiment being conducted. Usually it was between 100mW and 250mW. A simple experiment where

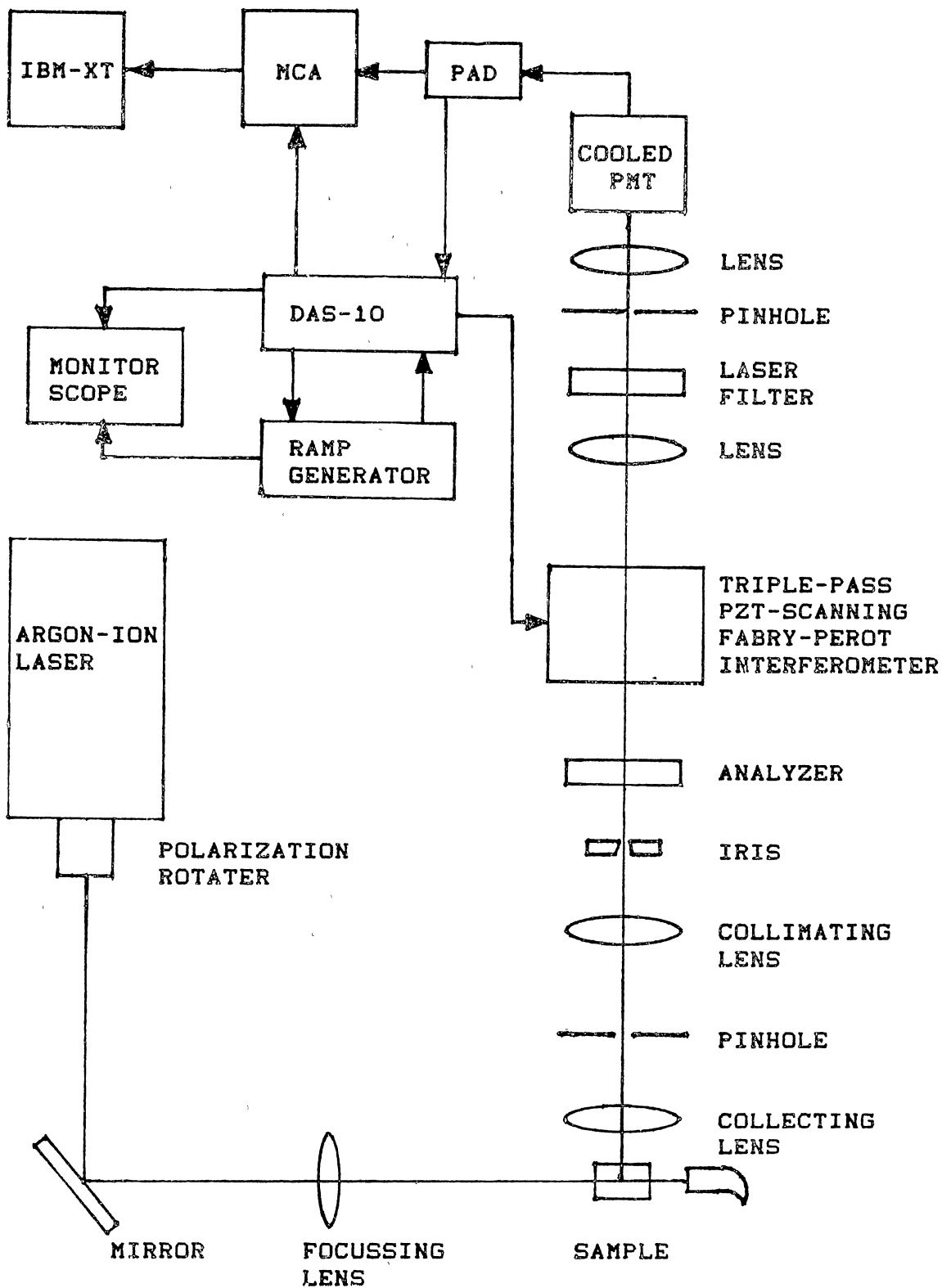


Figure 1. Experimental Setup for Brillouin Scattering Experiments.

the Brillouin intensity was measured as a function of power was performed on the more absorbing samples. It was determined that no noticeable heating of the sample was taking place at powers of 250mW or less.

The scattered light was collected at 90° by an Olympus 55mm camera lens, spatially filtered using a pinhole and collimated using an Olympus 50mm camera lens. The size of the pinhole varied depending on the situation and the experiment being conducted but was typically 100µm. The collimated light was passed through a stabilized (using a Burleigh DAS-10 stabilization unit and RC-43 ramp generator) triple-pass Burleigh model RC-110 Fabry-Perot interferometer. The Fabry-Perot output was then focused onto the cathode of a cooled ITT FW-130 photomultiplier tube.

The output pulses of the photomultiplier tube were sent both to a Canberra model 3502 multichannel analyzer (MCA) for display of the spectrum and to a Canberra amplifier-discriminator (PAD) for use by the stabilization unit of the Fabry-Perot. The spectrum collected in the (MCA) could then be sent to an IBM PC/XT 80286 computer for analysis and storage of the data. A computer data base (Smart Integrated Software (1988)) was used to record the experimental parameters and equipment settings for each experimental run.

A computer program written in IBM Advanced BASIC was used to analyze and plot the data received from the (MCA).

A listing of the program and an explanation of the algorithms used in the program can be found in Appendix A. In addition to this program, a commercial plotting routine (Plotit (1989)) was obtained to quickly produce publishable quality plots on a Hewlett Packard ColorPro plotter. Figure 2 shows a plot of a typical room temperature Brillouin spectrum of the  $\text{Rb}_2\text{O-SiO}_2$  sample. (For brevity, the five glasses used in this study will be referred to as  $\text{M}_2\text{O-SiO}_2$  where  $\text{M} = \text{Li}, \text{Na}, \text{K}, \text{Rb},$  and  $\text{Cs}$  even though each glass contains additional materials). The spectrum shows both the longitudinal acoustic (LA) and transverse acoustic (TA) peaks and the central Rayleigh peak. In this plot a smooth curve was drawn through the data points. The interpretation of the spectrum will be discussed in Chapter 3.

### Procedure

In this section, the methods used to measure the plate separation of the Fabry-Perot interferometer, the index of refraction of the samples and the densities will be discussed.

The plate separation of the Fabry-Perot must be known in order to determine the Brillouin shifts. Whenever the plate separation was changed, a Brillouin spectrum of fused quartz was taken. This spectrum in conjunction with the known LA Brillouin shift of fused quartz was then used to determine the plate separation using the same

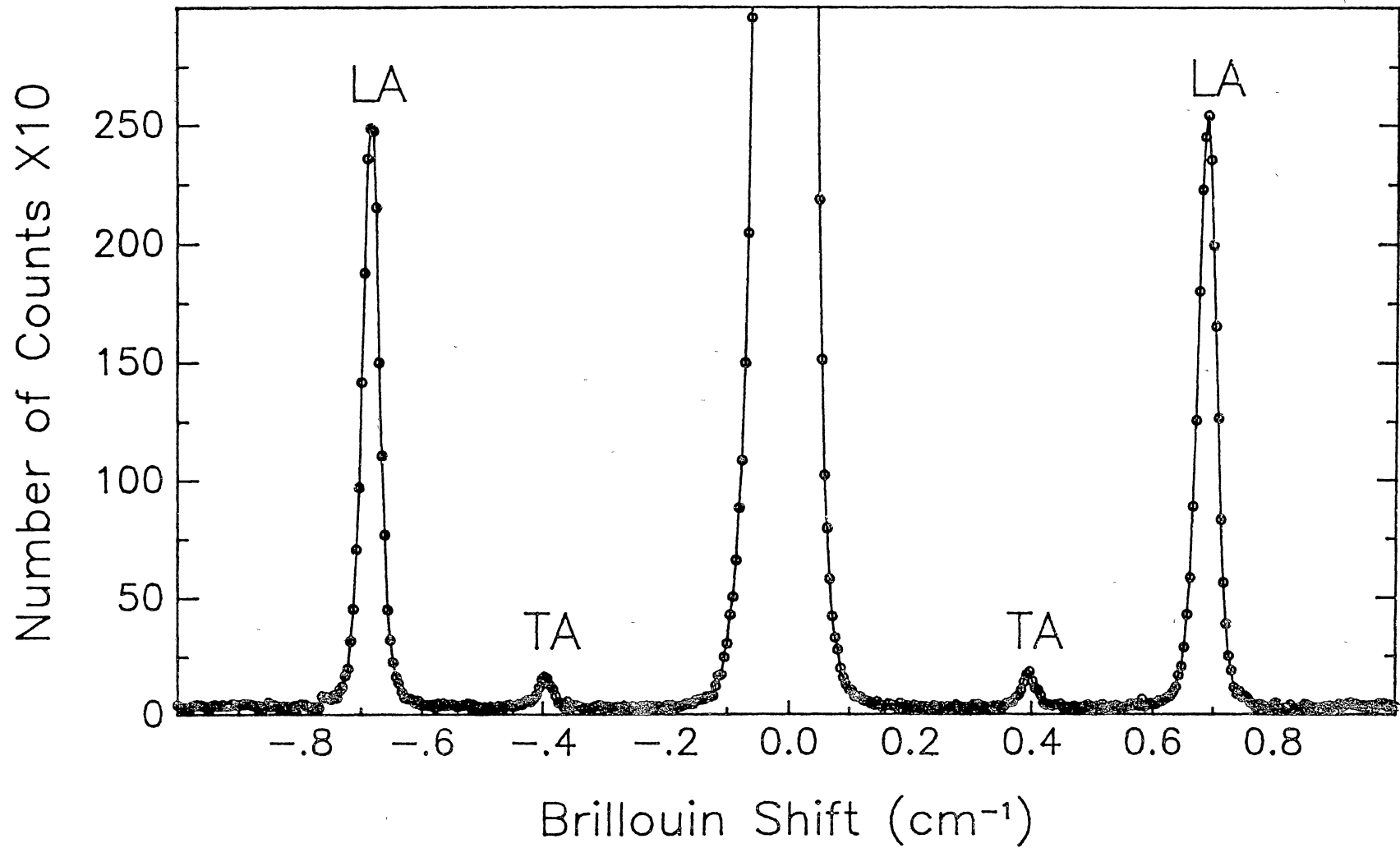


Figure 2. Brillouin Spectrum of the Rb<sub>2</sub>O-SiO<sub>2</sub> Glass.

analysis computer program mentioned earlier.

The LA shift of fused quartz, used in the analysis program, was the average value of a number of independent measurements where the plate separation was measured using a traveling microscope. The results compared very well with published results. Table II lists the results of our measurements on fused quartz as well as the results obtained by other researchers using Brillouin spectroscopy (Schroeder (1980) and Schroeder (1985)).

The computer program used to analyze the data had several functions. It was first used to analyze the fused quartz data to determine the plate separation of the Fabry-Perot. With the knowledge of the plate separation, it was used to determine the Brillouin shifts of the glass samples. The program also printed-out the intensities of the Rayleigh and Brillouin peaks as well as peak centroids, the full-width at half-maximum of each peak, the free spectral range, the finesse, and the Landau-Placzek ratio.

The Brillouin shifts of the glass samples were measured in this way, over a period of several years using several different plate separations. (Using different plate separations was necessary to make sure that the Brillouin peaks were not overlapped into adjoining orders). The plate separations used in these experiments varied between about 0.257cm and 0.282cm.

The expression for the phonon velocity is,

TABLE II  
RESULTS OF FUSED QUARTZ MEASUREMENTS

Source	$\Delta\omega_{TA}$ ( $\text{cm}^{-1}$ )	$\Delta\omega_{LA}$ ( $\text{cm}^{-1}$ )	n	$\rho$ ( $\text{g}/\text{cm}^3$ )
This Report $\lambda_0 = 5145\text{\AA}$	0.504	0.801	1.462	2.207
Schroeder (1980) $\lambda_0 = 6328\text{\AA}$			1.4577	2.2035

	$V_{TA}$ ( $\times 10^5 \text{cm/s}$ )	$V_{LA}$ ( $\times 10^5 \text{cm/s}$ )	$C_{44}$ ( $\times 10^{10} \text{dyne}/\text{cm}^2$ )	$C_{11}$ ( $\times 10^{10} \text{dyne}/\text{cm}^2$ )
This Report $\lambda_0 = 5145\text{\AA}$	3.76	5.98	31.2	78.9
Schroeder (1985) $\lambda_0 = 6328\text{\AA}$	3.7487	5.9442	30.97	79.00

	$P_{12}$	$P_{44}$
This Report $\lambda_0 = 5145\text{\AA}$	0.279	-0.0792
Schroeder (1980) $\lambda_0 = 6328\text{\AA}$	0.270	-0.0718



$$v = \frac{\Delta\omega\lambda_0 c}{4\pi n \sin\left(\frac{\phi}{2}\right)} \quad (2.1)$$

where  $\Delta\omega$  is the Brillouin shift,  $\lambda_0$  is the laser wavelength,  $c$  the speed of light,  $n$  the index of refraction of the sample, and  $\phi$  is the scattering angle. As can be seen, in order to determine the acoustic velocities from which the elastic constants can be determined, one needs among other things, the knowledge of the index of refraction. As has already been mentioned, the samples were cut so that two of the faces intersected so as to make a prism angle of  $60^\circ$ . The index of refraction was measured using a standard Gaertner-Peck spectrometer designed to use the common refractive angle minimum deviation method. The procedure was complicated by the non-uniformity of the samples. The image of the slit after passing through the sample, as seen through the telescope of the spectrometer, was bent and distorted for most of the glasses leading to a higher uncertainty in the indices than would otherwise be expected from this method.

The results of the index of refraction and density measurements for the five glasses, fused quartz, and toluene are given in Table III.

To determine the elastic constants,  $C_{11}$  and  $C_{44}$  the density  $\rho$  of the samples must be measured as can be seen from the following equations,

$$\begin{aligned} C_{11} &= \rho v_{LA}^2 \\ C_{44} &= \rho v_{TA}^2 \end{aligned} \quad (2.2)$$

The densities were measured using the buoyancy

TABLE III  
 DENSITIES, REFRACTIVE INDEX, AND  
 COLOR OF THE GLASSES AND TOLUENE

Sample	Density (g/cm <sup>3</sup> )	Index of Refraction (5145A)	Color
Li <sub>2</sub> O-SiO <sub>2</sub>	3.22 ± 0.03	1.604 ± 0.005	Brown
Na <sub>2</sub> O-SiO <sub>2</sub>	3.21 ± 0.03	1.583 ± 0.005	Brown
K <sub>2</sub> O-SiO <sub>2</sub>	3.15 ± 0.03	1.584 ± 0.005	Dark Brown
Rb <sub>2</sub> O-SiO <sub>2</sub>	3.47 ± 0.03	1.573 ± 0.005	Light Brown
Cs <sub>2</sub> O-SiO <sub>2</sub>	3.74 ± 0.03	1.591 ± 0.005	Light Brown
SiO <sub>2</sub>	2.21 ± 0.03 <sup>1</sup>	1.462 ± 0.001	Clear
Toluene	0.8669 <sup>2</sup>	1.493 ± 0.001 <sup>3</sup>	Clear

<sup>1</sup>Pan (1989)

<sup>2</sup>CRC Handbook (1987)

<sup>3</sup>Bouchalkha (1989)

principle with distilled water as the working fluid. In this method one is able to determine the volume of the irregularly shaped glass sample by measuring the change in weight as the sample is submerged into the working fluid.

### The Brillouin Shifts

In this section the method used by the analysis program to measure the Brillouin shifts is discussed.

Before taking data, the ramp amplitude of the DAS-10 was adjusted to display three orders of the Fabry-Perot output below the ramp. (The ramp amplitude controls the voltage range sent to the piezoelectric stacks on one of the Fabry-Perot plates for one sweep. Thus a larger voltage range translates into a larger movement of one plate toward the other allowing the Fabry-Perot to scan through several orders). Figure 3 shows a typical vertical-unpolarized Brillouin spectrum of intensity versus channel number of the fused quartz sample taken at room temperature. In this plot a smooth curve was drawn through the data points without showing the points. The figure shows three orders with the very intense Rayleigh peaks off scale and the LA and smaller TA peaks clearly shown. Each data set received from the multichannel analyzer consisted of 1024 channels.

Figure 4 illustrates the method used to determine the Brillouin shifts from the experimental data. The free spectral range (FSR) is defined as the range of

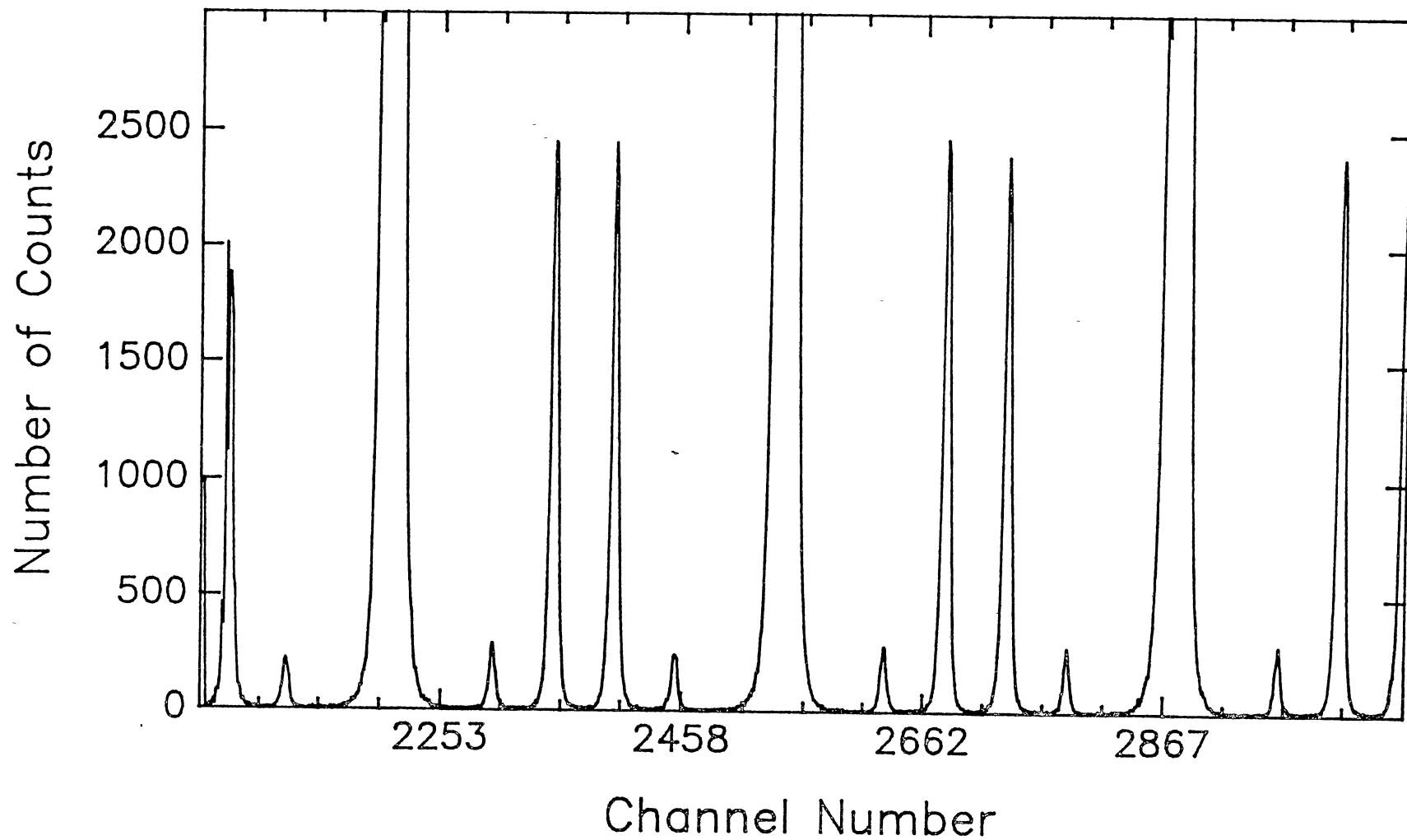


Figure 3. Three Orders of the Vertical-Unpolarized Brillouin Spectrum of Fused Quartz.

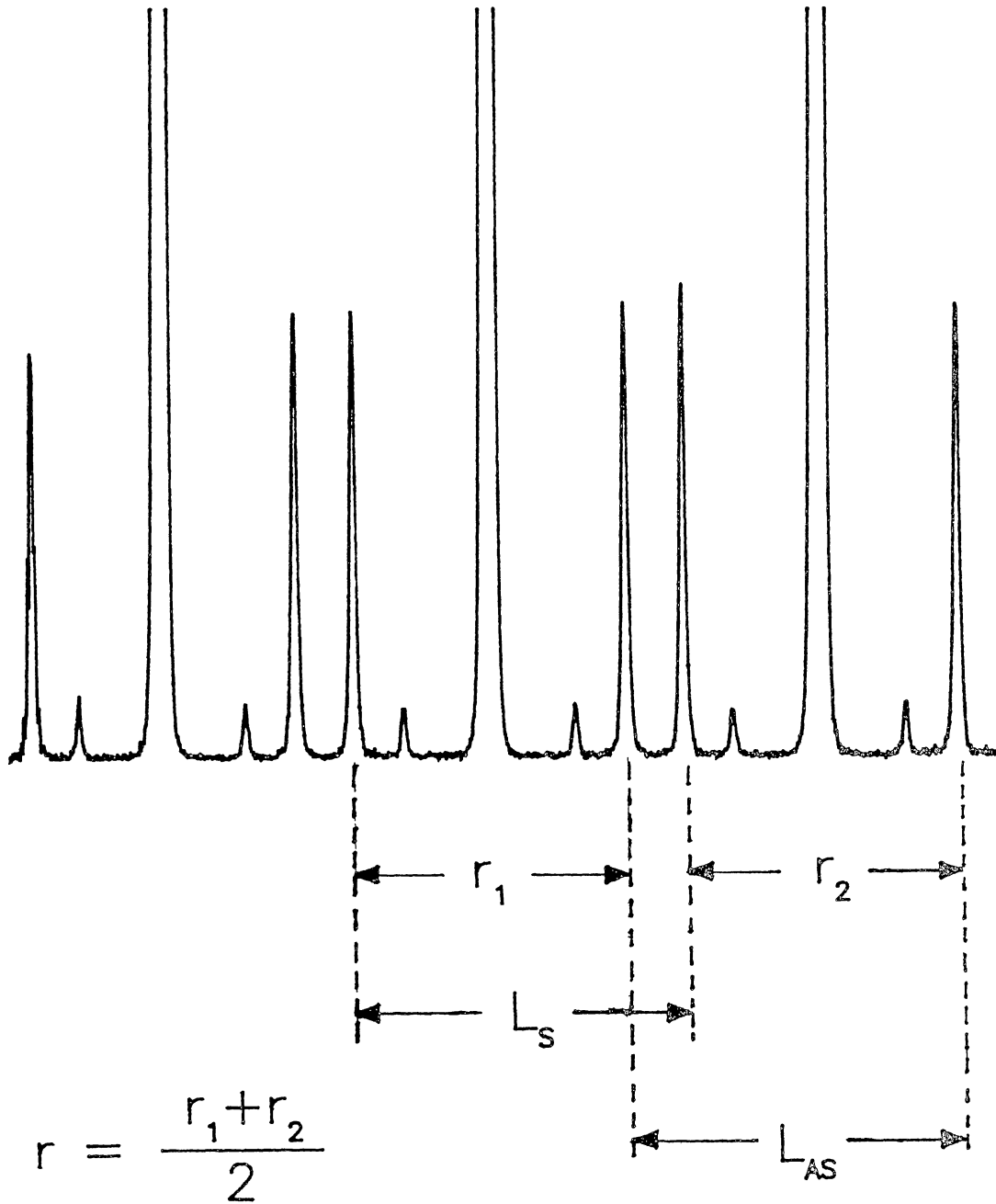


Figure 4. Illustration of the Method used to Determine the Brillouin Shifts.

frequencies that can be observed in one order without overlap into the next order. In units of  $\text{cm}^{-1}$ , the free spectral range of the Fabry-Perot is defined as (Hecht (1975)),

$$\text{FSR} = \frac{1}{2d} \quad (2.3)$$

where  $d$  is the Fabry-Perot plate separation in centimeters. Letting  $\Delta\omega_{\text{LA}}$  represent the actual Brillouin shift in units of  $\text{cm}^{-1}$ , we can set the ratio of the Brillouin shift to the FSR, equal to the ratio of the average number of channels between the Stokes and anti-Stokes Brillouin peaks  $r$ , to the sum of the average number of channels between the anti-Stokes peaks  $L_{\text{AS}}$  and the average number of channels between the Stokes peaks  $L_{\text{S}}$ ,

$$\frac{\Delta\omega_{\text{LA}}}{\text{FSR}} = \frac{r}{(L_{\text{AS}} + L_{\text{S}})} \quad (2.4)$$

Solving for the Brillouin shift and using Equation (2.3) we get,

$$\Delta\omega_{\text{LA}} = \frac{r}{2d(L_{\text{AS}} + L_{\text{S}})} \quad (2.5)$$

In Appendix A the reader will find the algorithms used by the analysis program to compute the centroids of the Brillouin peaks used to calculate  $L_{\text{AS}}$ ,  $L_{\text{S}}$ , and  $r$  used in the Brillouin shift calculations.

The free spectral range in our experiments depended on the plate separation but was typically around  $2.0\text{cm}^{-1}$  or  $6.0 \times 10^{10}\text{Hz}$ . The finesse of the instrument depended on the quality of the alignment and ranged from the low to upper fifties and occasionally in the low sixties.

All of the data taken in these experiments were recorded in a computerized spreadsheet (Smart Integrated Software (1989)). The spreadsheet was then used to do all of the tedious calculations such as mean values, uncertainties, and other calculations involving the Brillouin shifts and the elastic constants.

Now that the Brillouin shifts have been determined, the index of refraction and the density can be used to calculate the velocities using Equation (2.1) and the elastic constants using Equation (2.2).

#### Intensity Measurements

In order to determine the photo-elastic constants it is necessary to measure the integrated areas of the Brillouin peaks of the glass samples relative to some standard such as fused quartz with known photo-elastic constants taken under identical experimental conditions. The method of comparing to a standard is the preferred method over measuring the absolute intensities since this would require the knowledge of experimental conditions which are difficult to measure, in practice, with any degree of accuracy.

The photo-elastic constants of fused quartz have been measured previously by Schroeder (1980). Schroeder determined the photo-elastic constants by comparing the scattered intensities of fused quartz to liquid toluene

and water. We decided to repeat these experiments using toluene as a check of our experimental apparatus and procedure.

$P_{12}^T$  of toluene can be determined by comparing two relations for the density derivative of the optical dielectric constant at constant entropy for a pure liquid. The first of these expressions was derived by Fabelinskii (1968) from thermodynamic derivations of the scattered intensity from adiabatic (Brillouin components) and isobaric (Rayleigh component) density fluctuations in pure liquids. The second expression can be obtained by comparing the theoretical expression for the (LA) Brillouin intensity for isotropic materials (see Chapter III for the derivation), to the thermodynamic calculation found in Fableinskii,

$$\begin{aligned} \left( \rho \frac{\partial \epsilon}{\partial \rho} \right)_s &= \left( \frac{1 \partial \epsilon}{\sigma \partial T} \right)_p \left( \frac{\sigma^2 v^2 T}{R_{LP} C_p} \right)^{\frac{1}{2}} \\ &= n^4 P_{12}^T . \end{aligned} \quad (2.6)$$

In Equation (2.6),  $\sigma$  is the coefficient of volume expansion,  $v$  the velocity of hypersound,  $T$  the absolute temperature,  $C_p$  the specific heat at constant pressure,  $\rho$  the density,  $n$  is the index of refraction,  $\left( \frac{1 \partial \epsilon}{\sigma \partial T} \right)_p$  is the temperature coefficient of the dielectric constant at constant pressure, and  $R_{LP}$  is the Landau-Placzek ratio. The Landau-Placzek ratio is defined as the ratio of the intensity of the Rayleigh peak to that of the total



Brillouin intensities,

$$R_{LP} = \frac{I_R}{2I_B} . \quad (2.7)$$

In determining  $P_{12}^T$  from Equation (2.6), we used Fabelinskii's listed values for  $C_p = 1.68 \times 10^7 \text{erg/deg}$ ,  $\sigma = 106 \times 10^{-5} \text{deg}^{-1}$ , and the temperature coefficient of the dielectric constant  $-1.74$ . We used our values for the hypersonic velocity  $v = 1.34 \times 10^5 \text{cm/s}$  and  $R_{LP} = 0.42$  that were obtained from the Brillouin spectrum. These values for  $v$  and  $R_{LP}$  compare very well with values found in the literature. Fabelinskii listed a value for  $v$  of  $1.38 \times 10^5 \text{cm/s}$  and used the top part of Equation (2.6) along with an independently measured value of the density derivative of the dielectric constant, to compute  $R_{LP}$  obtaining a value of 0.44. Our directly measured value of 0.42 compares favorably with Fabelinskii's calculated value and other directly measured values from Brillouin scattering of 0.42 (Cummins et al. (1966)) and 0.415 (Schroeder (1980)). The velocity and the Landau-Placzek ratio from our measurements were measured at a temperature of 293K and the index of refraction was measured at a wavelength of  $5145 \text{\AA}$  giving a value of 1.493.

Using these values for  $v$ ,  $n$ , and  $R_{LP}$  and those listed in Fabelinskii for  $C_p$ ,  $\sigma$ , and  $\left(\frac{\partial \epsilon}{\partial T}\right)_p$ , we obtained a value of 1.61 for the density derivative of the dielectric constant which compares well with Fabelinskii's listed value of 1.60.

Using the bottom half of Equation (2.6), we were able to determine  $P_{12}^T$  using our value for the index of

refraction. The result is  $P_{12}^T = 0.322$  which compares very well with Schroeder's result of 0.3225. Using our value for the photo-elastic constant of toluene we then compared the toluene Brillouin intensities to the (LA) Brillouin intensities of fused quartz to get  $P_{12}^0$  (the superscript "o" refers to the fused quartz value). With the fused quartz standard calibrated, we then proceeded to measure the photo-elastic constants of the  $\text{Eu}^{3+}$ -doped glass samples. The details of the procedure used to measure the photo-elastic constants will be discussed in Chapter III.

In the calibration of fused quartz just discussed and in subsequent intensity measurements with the other glass samples, the integrated areas of the Brillouin peaks must be calculated. The areas were determined by adding-up the total number of counts in each channel, minus the background, within a region-of-interest that included the peak in question. The area used in subsequent calculations, was the average of five of the right most peaks within the three orders shown in Figure 3 on page 18. The background was determined from that region of the spectrum that had the fewest number of counts, frequently the region between the LA peaks.

The procedure would then be to take a spectrum of fused quartz and then under the exact same conditions, except for focusing due to the difference in the index of refraction, take a spectrum of one of the glass samples.

Then from the computer print-out of the areas, calculate the ratio of the Brillouin area of the glass sample to that of fused quartz. The results could then be used to determine the photo-elastic constants. More will be said on this in Chapter III.

The above procedure was complicated by the fact that the glass samples were absorbing in the 5145Å region of the spectrum. As a result of this absorption, the intensity of the Brillouin peaks depended on the position of the scattering volume within the sample. Therefore, as many as twelve runs were made at different positions inside each sample. In this way we could extrapolate the intensities to that point in the sample where the scattering volume is very close to both the entrance surface where the laser beam enters the sample and to the exit surface where the scattered light leaves the sample.

Referring to Figure 5, the areas were fit to the following equation,

$$I = I_0 e^{-\alpha h} \quad (2.8)$$

where  $\alpha$  is the absorption of the material in  $\text{cm}^{-1}$  and  $h = x+z$  is the sum of the distance the laser beam travels through the sample to the scattering volume  $z$  and the distance the scattered light travels from the scattering volume to the point where it leaves the sample  $x$ . A linear regression routine, part of a graph plotting program (Plotit (1989)), was used to determine  $\alpha$ ,  $I_0$  and to plot the results. Table IV lists the absorption and

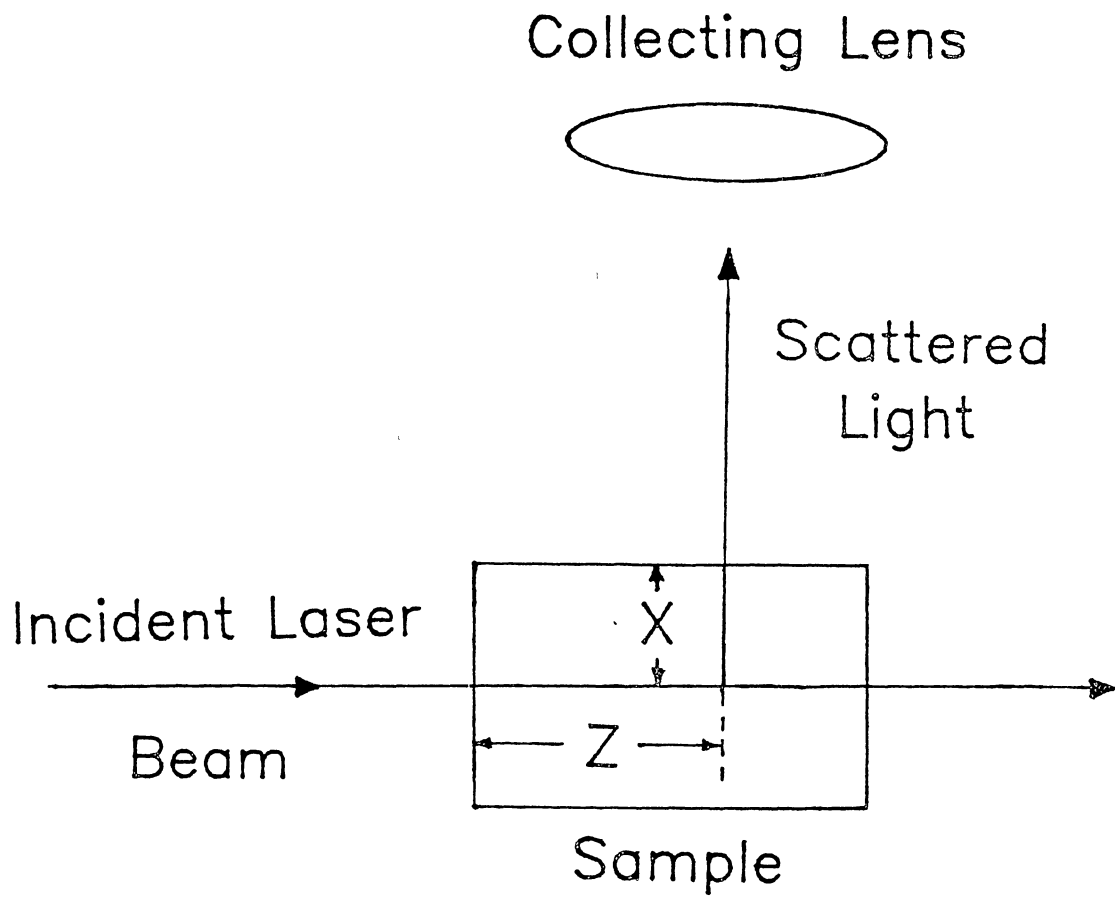


Figure 5. Top View of the Sample Showing the Distance Traveled by the Incident and Scattered Light.

TABLE IV  
ABSORPTION COEFFICIENTS AND REGRESSION  
ANALYSIS PARAMETERS

Sample	$\alpha$ ( $\text{cm}^{-1}$ )	Standard Error ( $\text{cm}^{-1}$ )	Correlation Coefficient
$\text{Li}_2\text{O}-\text{SiO}_2$	0.6	$\pm 0.1$	0.940
$\text{Na}_2\text{O}-\text{SiO}_2$	1.49	$\pm 0.04$	0.997
$\text{K}_2\text{O}-\text{SiO}_2$	1.98	$\pm 0.08$	0.995
$\text{Rb}_2\text{O}-\text{SiO}_2$	0.24	$\pm 0.02$	0.953
$\text{Cs}_2\text{O}-\text{SiO}_2$	0.43	$\pm 0.03$	0.971
$\text{SiO}_2$	0.04	$\pm 0.02$	0.531

regression analysis parameters for the glass samples and for fused quartz.

After taking data in the glass sample, fused quartz runs were taken under the same experimental conditions and a similar analysis with the Plotit program gave values of  $I_0^0$  and  $\alpha^0$  for fused quartz. The ratios of the areas  $I_0/I_0^0$ , were then computed and entered into the spreadsheet for calculation of the photo-elastic constants. Figure 6 shows a plot of  $\ln(A)$  vs.  $h$  for the  $K_2O-SiO_2$  and fused quartz samples showing the area ratio  $\beta$  at the top of the figure along with the expected uncertainty. Also shown are the values for the absorption coefficient and extrapolated intensity along with their respective uncertainties.

The uncertainties were computed from the linear regression standard error determined by the regression program of Plotit.

This is not the whole story however. In the case of fused quartz the absorption was small enough so that the intensity of the incident laser light that was lost at the entrance face due to reflection was almost totally compensated for by the back reflection from the exit face. In the case of the high absorbing samples, this back reflection from the exit face did not compensate as much for that intensity lost at the entrance face as it did for fused quartz. The difference amounted to as much as a 3% decrease in the laser intensity inside the high

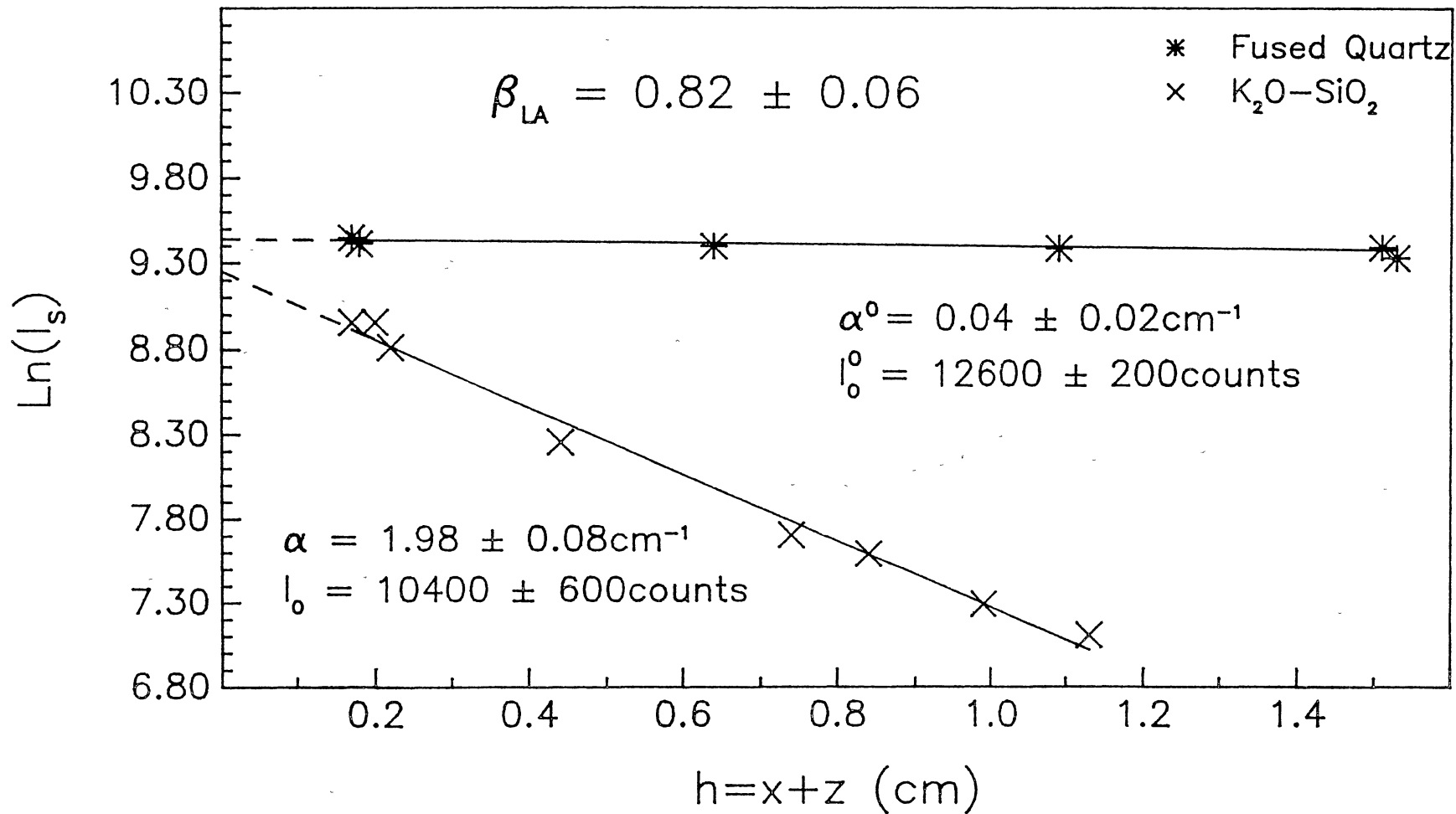


Figure 6. Natural Logarithm Versus  $h$  for the  $\text{K}_2\text{O}-\text{SiO}_2$  Glass Sample and for Fused Quartz.

absorbing sample compared to that of fused quartz. The corresponding corrections for each sample were made to the intensity ratios. These and other corrections are discussed in detail in Appendix B.

In the case of the  $\text{Rb}_2\text{O-SiO}_2$  sample, the sample had been cut inadvertently so as to direct the back reflection down and away from the laser beam inside the sample. The correction to the area in this case was on the order of 3%.

Table V lists the intensity ratios for the five glasses studied in this report. These values have been corrected for the back reflection and this explains why  $\beta_{\text{LA}}$  for  $\text{K}_2\text{O-SiO}_2$  listed in the table is different from that shown at the top of Figure 6. Details of the back reflection correction plus other correction factors are given in Appendix B.



TABLE V  
BRILLOUIN INTENSITIES RELATIVE  
TO FUSED QUARTZ

Sample	$\beta_{TA}$	$\beta_{LA}$
$Li_2O-SiO_2$	0.55	0.60
$Na_2O-SiO_2$	0.71	0.93
$K_2O-SiO_2$	0.52	0.84
$Rb_2O-SiO_2$	0.46	1.15
$Cs_2O-SiO_2$	0.37	1.36

## CHAPTER III

### THEORETICAL ANALYSIS

#### Equations of Motion

In this first section the solutions to the equations of motion for an elastic medium are discussed for the general case applicable to both crystals and glasses. In the next section, the Brillouin frequency and wavelength are discussed and in the final section, the Rayleigh ratio will be evaluated for glass materials. Since this is a report on Brillouin scattering in glasses, the few examples cited will use glass as the model.

It can be shown (Nye (1981)) by application of Newton's second law, that the equations of motion for an elastic medium of density  $\rho$  expressed in terms of the stress can be written as,

$$\rho \ddot{u}_j = \sum_{i=1}^3 \frac{\partial \sigma_{ij}}{\partial x_i} \quad (j=1, 2, 3) \quad (3.1)$$

where  $u_j$  is the displacement from equilibrium in the  $x_j$  direction and  $\sigma_{ij}$  are the elements of the stress tensor. Equation (3.1) is the fundamental equation that relates the spatial variation of the stress in the material with the acceleration of its parts. It is the beginning point

of the study of elastic waves in crystals and in glasses (Nye (1981)).

The relationship between the stress and the strain tensors in the harmonic approximation (Hooke's law) is given by (Nye (1981)),

$$\sigma_{ij} = \sum_{k=1}^3 \sum_{l=1}^3 C_{ijkl} s_{kl} \quad (i, j=1, 2, 3) \quad (3.2)$$

where the  $C_{ijkl}$  are called the elastic stiffness constants and the  $s_{kl}$  are the elements of the strain tensor. Using Equation (3.2) and assuming a plane wave solution for  $u_j$ , Equation (3.1) can be written in the long wavelength limit as (Cummins and Schoen (1972)),

$$\sum_{k=1}^3 \sum_{l=1}^3 \sum_{m=1}^3 \left[ C_{ijkl} \frac{q_l q_m}{q^2} - \rho v^2 \delta_{jk} \right] u_k^0 = 0 \quad (j=1, 2, 3). \quad (3.3)$$

Equation (3.3) represents three equations, one for each value of  $j$ . The three eigenvalues of the determinant of the coefficients of  $u_k^0$  in Equation (3.3), give the velocities in the long wavelength limit of the three acoustic modes,

$$\rho v_j^2 = C_j \quad (j=1, 2, 3). \quad (3.4)$$

The  $C_j$  are in general, complicated linear combinations of the elastic constants. Only for phonons propagating in high symmetry directions of crystals will the left side of Equation (3.4) be equal to a single elastic constant.

The number of non-zero elastic constants depends on the symmetry of the material. Glasses are isotropic and as a result the stress produced by a small strain can be described by just two independent elastic constants

$C_{11}$  and  $C_{44}$ . (Where the more convenient six-component notation has been used for the elastic constants). The Cauchy relation  $2C_{44} = C_{11} - C_{12}$  allows one to determine  $C_{12}$ . (Schroeder (1977)).

The displacement eigenvectors associated with each velocity eigenvalue can be found by substituting the  $v_j$  back into the equations of motion. In glasses, the displacement vectors  $\vec{u}$  will be either parallel or perpendicular to the phonon wavevector  $\vec{q}$ .

As an example, let the phonon wavevector  $\vec{q}$  be in the x direction of an arbitrarily chosen rectangular coordinate system in a glassy material. In this case,  $q=q_x$  and  $q_y=q_z=0$ . From Equation (3.3), we get,

$$\begin{aligned} (C_{11} - \rho v_1^2) u_x^0 &= 0 \Rightarrow v_1^2 = \frac{C_{11}}{\rho}, & u_x^0 \parallel q_x \\ (C_{44} - \rho v_2^2) u_y^0 &= 0 \Rightarrow v_2^2 = \frac{C_{44}}{\rho}, & u_y^0 \perp q_x \\ (C_{44} - \rho v_3^2) u_z^0 &= 0 \Rightarrow v_3^2 = \frac{C_{44}}{\rho}, & u_z^0 \perp q_x. \end{aligned} \quad (3.5)$$

Thus, for glasses there is one longitudinal mode and one degenerate transverse mode for the phonon propagating in the x direction. Since it makes no difference which direction we choose to point the x axis in isotropic materials, we would expect to get the same result for any other direction in the glass. In crystals however, the results can be very different for other directions of propagation of the phonon being probed. In general there are three distinct modes giving three separate eigenvalues in crystals.

### The Phonon Frequency and Wavevector

To this point, we have seen that the equations of motion can be solved to obtain an expression for the phonon velocities in terms of the elastic constants. The next step is to find out how the velocities are experimentally measured.

Brillouin scattering is the inelastic scattering of photons. Quantum mechanically, Brillouin scattering is a three part process. Referring to Figure 7, an incident photon of energy  $\hbar\omega_i$  is absorbed resulting in the creation of a scattered photon of energy  $\hbar\omega_s$ , accompanied by the creation (Stokes) or destruction (anti-Stokes) of a phonon of energy  $\hbar\Omega$ . Conservation of energy and momentum in the process give rise to the following selection rules;

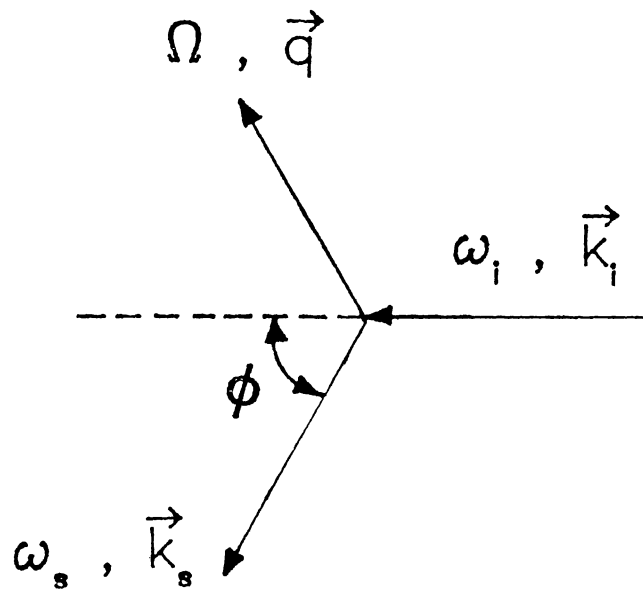
$$\begin{aligned}\omega_i &= \omega_s \pm \Omega \\ \vec{k}_i &= \vec{k}_s \pm \vec{q}\end{aligned}\quad (3.6)$$

where  $\Omega$  is the phonon frequency,  $\vec{q}$  is the phonon wavevector and the subscripts "i" and "s" refer to the incident and scattered light components respectively.

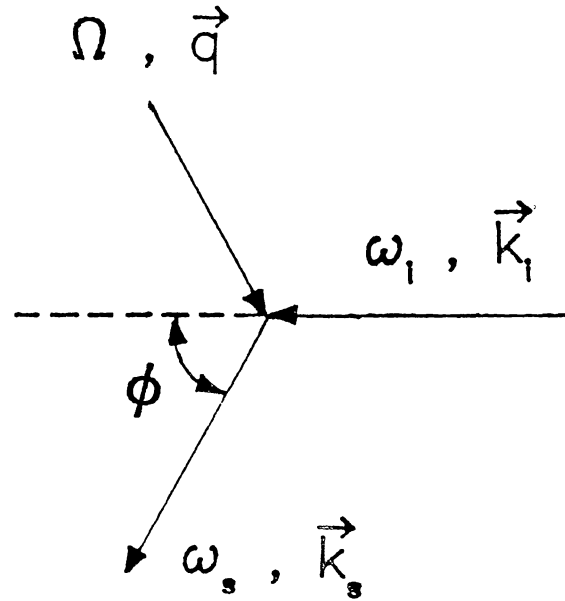
It can be shown that the wavevector of the phonon in terms of the index of refraction of the sample  $n$ , the wavelength of the incident light  $\lambda_0$  and the scattering angle  $\phi$  can be written as,

$$q = \frac{4\pi n}{\lambda_0} \sin \frac{\phi}{2} . \quad (3.7)$$

It is important to realize that the phonon wavevector probed in Brillouin spectroscopy is completely determined by the experimental geometry (i.e.  $\phi$ ) and parameters.



Phonon Creation  
(Stokes Process)



Phonon Destruction  
(Anti-Stokes Process)

Figure 7. The Brillouin Scattering Process.

The direction chosen for  $\vec{q}$  in crystals is important because, as has already been mentioned, the solutions to the equations of motion are simple only in high symmetry directions of the crystal. In glasses, the direction of  $\vec{q}$  is unimportant because of the isotropic nature of these materials.

The maximum value of  $q$  is typically on the order of  $10^5 \text{ cm}^{-1}$  as compared with the typical crystal Brillouin zone width of  $10^8 \text{ cm}^{-1}$ .

Experimentally, the Brillouin shifts  $\Delta\omega = \omega_i - \omega_s$ , which are equal to the phonon angular frequencies  $\omega$  (see Equation (3.6)), are determined from a Brillouin spectrum obtained using a single mode laser of known wavelength and a Fabry-Perot interferometer.

In general the Brillouin shifts can be determined from the spectrum with the knowledge of the plate separation of the Fabry-Perot (see Equation (2.5)). Using the Brillouin shifts, the velocities can be determined using  $v = \frac{\Delta\omega}{q}$  and Equation (3.7) to get,

$$v = \frac{\Delta\omega c \lambda_0}{4\pi n \sin\left(\frac{\phi}{2}\right)}. \quad (3.8)$$

And finally the elastic constants can be determined using Equation (3.5).

#### The Rayleigh Ratio

Thus far we have seen how the elastic constants can be determined by measuring the acoustic phonon

velocities. However, we still need to determine how to identify the peaks in the Brillouin spectrum with the different phonon modes. For example, how is it determined which pair of peaks in Figure 2 correspond to the transverse phonon mode?

The answer to this question lies in the Rayleigh ratio or the differential cross section per unit volume. In this section the Rayleigh ratio is discussed and it is shown how it can be used to determine the polarization of the scattered light produced by the different phonon modes. In general, by using an analyzer before the Fabry-Perot, only certain pairs of peaks will show up in the spectrum. The calculation of the Rayleigh ratio will allow us to predict which peaks will appear for a given orientation of the analyzer.

To begin, consider laser light incident on a sample with electric field inside the sample given by,

$$\vec{E} = \hat{e} E_0 \exp[i(\vec{k}_i \cdot \vec{r} - \omega_i t)] \quad (3.9)$$

where  $\vec{k}_i$  is the incident wavevector,  $\omega_i$  the incident frequency and  $\hat{e}_i$  is the unit vector that describes the polarization of the incident light. The Rayleigh ratio is defined as the differential cross section per unit volume per unit incident intensity (Cummins and Schoen (1972)),

$$R = \frac{1}{V} \frac{d\sigma}{d\Omega} = \frac{R^2 I_s}{V I_i} \quad (3.10)$$

In Equation (3.10),  $I_s$  is the scattered intensity polarized in the  $\hat{e}_s$  direction,  $I_i$  is the incident



intensity polarized in the  $\hat{e}_1$  direction both inside the sample,  $V$  is the volume of the illuminated region being detected and  $R$  is the distance from the scattering volume to the collecting lens.

The exact form of the Rayleigh ratio can be derived in terms of the Brillouin scattering tensors  $\chi_1$  and other experimentally determined parameters (Cummins and Schoen (1972)). The elements of the Brillouin scattering tensors contain the photo-elastic constants (Pockel coefficients)  $P_{ijrs}$  that relate the change in the reciprocal dielectric constant  $\delta(\epsilon^{-1})$  and the strain  $s_{rs}$  produced by the acoustic phonons propagating through the material (Nye (1981)).

$$\delta(\epsilon^{-1})_{ij} = P_{ijrs} s_{rs} \quad (3.11)$$

It can be shown that the fluctuation of the dielectric constant can be written as (Born and Huang (1962)),

$$\delta\epsilon_{ij} = -\epsilon_{(0)ii}\epsilon_{(0)jj}P_{ijkl}s_{kl} \quad (3.12)$$

where  $\epsilon_{(0)ii}$  and  $\epsilon_{(0)jj}$  are the dielectric constants: ordinary and extraordinary for uniaxial crystals. In the case of glasses there is only one dielectric constant and these two quantities are equal to each other.

The Brillouin Rayleigh ratio is then derived (Cummins and Schoen (1972)) from the excess dipole moment per unit volume,  $P_i(r) = \frac{\delta\epsilon_{ij}E_j^0}{4\pi}$  where  $E_j^0$  is the amplitude of the electric field of the incident laser light. Assuming that the excitation of each acoustic mode is on the average in

thermal equilibrium at temperature T, then,

$$\langle (qu)^2 \rangle = \frac{K_B T}{2V\rho v^2} . \quad (3.13)$$

As a result we have,

$$R_j = \frac{K_B T \omega_s^4}{32\pi^2 c^4 \rho v_j^2} \left[ \hat{e}_s \cdot \chi_j \cdot \hat{e}_i \right]^2 \left( \frac{n_s}{n_i} \right) . \quad (3.14)$$

Equation (3.14) is the internal Rayleigh ratio of the  $j^{\text{th}}$  acoustic mode, where  $K_B$  is Boltzmann's constant, T is the sample temperature,  $\omega_s \approx \omega_i$  is the angular frequency of the scattered light, c is the speed of light,  $\rho$  is the density of the glass,  $v_j$  the velocity of the  $j^{\text{th}}$  phonon mode, and  $\hat{e}_s$  and  $\hat{e}_i$  are the unit vectors that describe the polarization of the scattered and the incident electric fields. The indices of refraction for the incident and scattered fields are given by  $n_i$  and  $n_s$  respectively. For glasses these two quantities are equal.

Equation (3.14) gives the scattering cross section for each acoustic mode in terms of the Brillouin tensors  $\chi_j$ . Values of the Brillouin scattering tensor and the elastic constants corresponding to the various eigenvalues  $\rho v_j^2$  have been tabulated for a number of phonon directions in a variety of crystal classes and for isotropic glasses by Cummins and Schoen (1972). Outlined below is an example of how to use these tabulated quantities.

Figure 8 shows the scattering geometry for a typical Brillouin scattering experiment in a glass. For this case, the eigenvalue, unit displacement vector, and Brillouin scattering tensor for a phonon propagating in

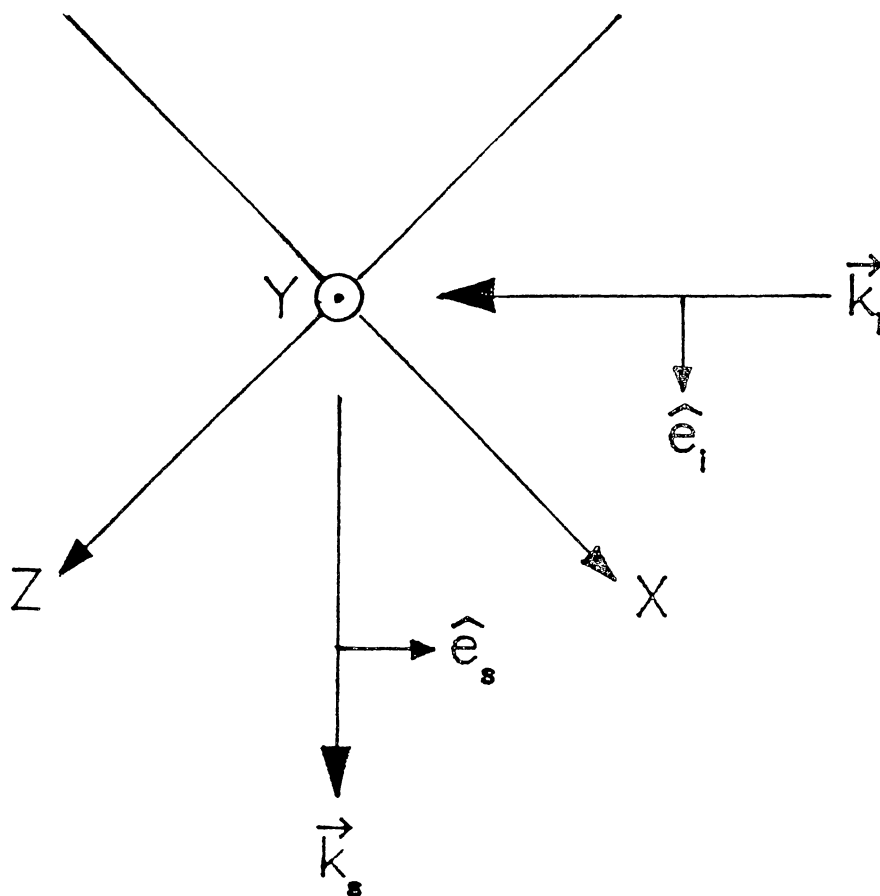


Figure 8. Brillouin Scattering Geometry.

the x direction, are given in Table VI.

Referring to Figure 8, there are four possible combinations for the polarization of the incident and scattered light:

$$\text{Incident light vertically polarized: } \hat{e}_i = \begin{pmatrix} 0 \\ 1 \\ 0 \end{pmatrix}$$

$$\text{Incident light horizontally polarized: } \hat{e}_i = \frac{1}{\sqrt{2}} \begin{pmatrix} 1 \\ 0 \\ 1 \end{pmatrix}$$

$$\text{Scattered light vertically polarized: } \hat{e}_s = (010)$$

$$\text{Scattered light horizontally polarized: } \hat{e}_s = \frac{1}{\sqrt{2}}(10\bar{1})$$

The next thing to do is to determine which combination of

$[\hat{e}_s \cdot \chi_j \cdot \hat{e}_i]$  from Equation (3.14) produces a

non-zero result. For the geometry shown in Figure 8,

there are four possibilities:

$$\text{i) } \underline{VV} \quad (0 \ 1 \ 0) \epsilon^2 \begin{pmatrix} P_{11} & 0 & 0 \\ 0 & P_{12} & 0 \\ 0 & 0 & P_{12} \end{pmatrix} \begin{pmatrix} 0 \\ 1 \\ 0 \end{pmatrix} = \epsilon^2 P_{12} ,$$

$$\text{ii) } \underline{HH} \quad \frac{1}{\sqrt{2}}(1 \ 0 \ \bar{1}) \epsilon^2 \begin{pmatrix} P_{11} & 0 & 0 \\ 0 & P_{12} & 0 \\ 0 & 0 & P_{12} \end{pmatrix} \frac{1}{\sqrt{2}} \begin{pmatrix} 1 \\ 0 \\ 1 \end{pmatrix} = \frac{\epsilon^2}{2}(P_{11} - P_{12}) = \epsilon^2 P_{44} ,$$

$$\begin{aligned} \text{iii) } \underline{VH} \quad \frac{1}{\sqrt{2}}(1 \ 0 \ \bar{1}) \epsilon^2 \begin{pmatrix} 0 & \frac{1}{2}(P_{11} - P_{12}) & 0 \\ \frac{1}{2}(P_{11} - P_{12}) & 0 & 0 \\ 0 & 0 & 0 \end{pmatrix} \begin{pmatrix} 0 \\ 1 \\ 0 \end{pmatrix} \\ = \frac{\epsilon^2}{2\sqrt{2}}(P_{11} - P_{12}) = \frac{1}{\sqrt{2}}\epsilon^2 P_{44} , \end{aligned}$$

$$\begin{aligned} \text{iv) } \underline{HV} \quad (0 \ 1 \ 0) \epsilon^2 \begin{pmatrix} 0 & \frac{1}{2}(P_{11} - P_{12}) & 0 \\ \frac{1}{2}(P_{11} - P_{12}) & 0 & 0 \\ 0 & 0 & 0 \end{pmatrix} \frac{1}{\sqrt{2}} \begin{pmatrix} 1 \\ 0 \\ 1 \end{pmatrix} \\ = \frac{\epsilon^2}{2\sqrt{2}}(P_{11} - P_{12}) = \frac{1}{\sqrt{2}}\epsilon^2 P_{44} . \end{aligned}$$

(3.15)

TABLE VI  
VELOCITIES, POLARIZATIONS AND BRILLOUIN  
SCATTERING TENSORS FOR GLASSES

---

$$\rho v^2 = C_{11}$$

$$\hat{u} = (1, 0, 0) \quad \text{Longitudinal}$$

$$\chi = \epsilon^2 \begin{pmatrix} P_{11} & 0 & 0 \\ 0 & P_{12} & 0 \\ 0 & 0 & P_{12} \end{pmatrix}$$

$$\rho v^2 = \frac{1}{2}(C_{11} - C_{12})$$

$$\hat{u} = (0, 1, 0) \quad \text{Transverse}$$

$$\chi = \epsilon^2 \begin{pmatrix} 0 & \frac{1}{2}(P_{11} - P_{12}) & 0 \\ \frac{1}{2}(P_{11} - P_{12}) & 0 & 0 \\ 0 & 0 & 0 \end{pmatrix}$$

$$\rho v^2 = \frac{1}{2}(C_{11} - C_{12})$$

$$\hat{u} = (0, 0, 1) \quad \text{Transverse}$$

$$\chi = \epsilon^2 \begin{pmatrix} 0 & 0 & \frac{1}{2}(P_{11} - P_{12}) \\ 0 & 0 & 0 \\ \frac{1}{2}(P_{11} - P_{12}) & 0 & 0 \end{pmatrix}$$


---

the incident and the scattered light are vertically polarized. Comparing this with the theoretical treatment above we see that this spectrum is the result of longitudinal acoustic (LA) phonons. In Figure 9c, the scattered light is horizontally polarized showing the transverse acoustic (TA) phonons. In Figure 10a the incident light is horizontally polarized and the scattered light is unpolarized. Figure 10b, shows the spectrum where the incident and scattered light are horizontally polarized showing the (LA) peaks with reduced intensity relative to that found in the VV spectrum. And finally, Figure 10c shows the (TA) peaks where the incident light is horizontally polarized and the scattered light is vertically polarized. In this case the (TA) intensity is the same as in the VH case.

Substituting the expressions for  $\left[ \hat{e}_s \cdot \chi_j \cdot \hat{e}_i \right]$  in Equation (3.15) into the equation for the Rayleigh ratio Equation (3.14), and using Equation (3.10) we arrive at the expressions for the intensity of the scattered light from the various Brillouin components,

$$I_{VV} = \frac{I_0}{R^2} e^4 \left( \frac{\omega_0}{c} \right)^4 \left( \frac{VK_{BT}}{32\pi^2} \right) \left( \frac{P_{12}^2}{C_{11}} \right), \quad (3.16a)$$

$$I_{HH} = \frac{I_0}{R^2} e^4 \left( \frac{\omega_0}{c} \right)^4 \left( \frac{VK_{BT}}{32\pi^2} \right) \left( \frac{P_{44}^2}{C_{11}} \right), \quad (3.16b)$$

$$I_{HV} = I_{VH} = \frac{I_0}{R^2} e^4 \left( \frac{\omega_0}{c} \right)^4 \left( \frac{VK_{BT}}{32\pi^2} \right) \left( \frac{P_{44}^2}{2C_{44}} \right). \quad (3.16c)$$

These are the expressions for the scattered light inside the glass and one must make corrections to obtain the corresponding expressions for outside the glass. In addition, the back reflection from the inside exit surface must be taken into account. This is the topic of a later section.

#### Intensities Relative to Fused Quartz

Figure 11 shows a top view of the sample with the laser beam of intensity  $I_0$  incident from the left. At the entrance surface a small fraction of the laser intensity is reflected and the rest is transmitted. The intensity just inside the sample is,

$$I(0,0) = TI_0 \quad (3.17)$$

where  $T$  is the transmittance and is given by,

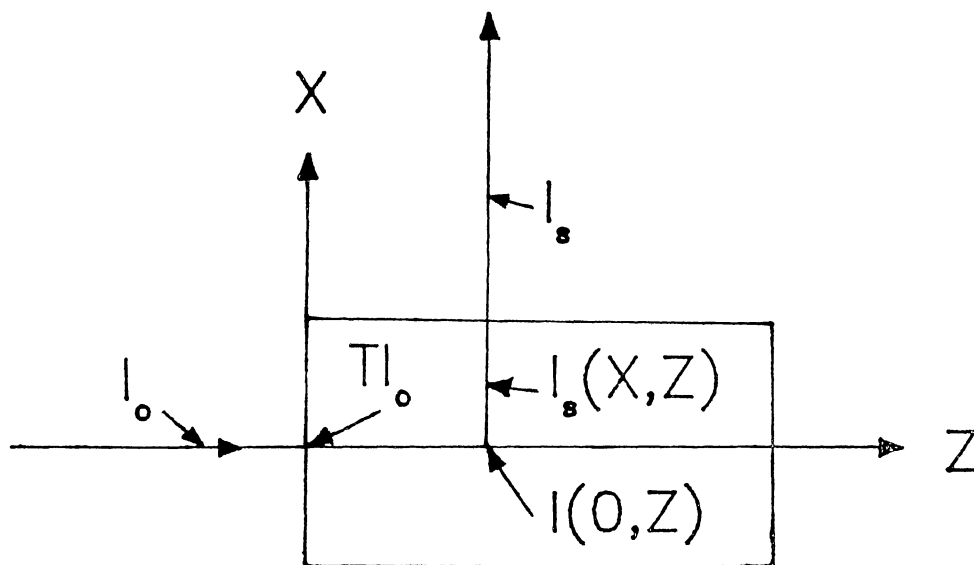
$$T = \frac{4n}{(n+1)^2 + \kappa^2} \quad (3.18)$$

where  $\kappa$  is the imaginary part of the index of refraction which can be neglected for relatively small absorption coefficients. The largest coefficient for our glasses is  $1.98\text{cm}^{-1}$  for  $\text{K}_2\text{O-SiO}_2$  which gives  $\kappa = 8.11 \times 10^{-6}$ .

Because of absorption, it is found that the intensity inside the sample decreases exponentially. The expression for the intensity of the laser beam inside the sample becomes (Loudon, (1965)),

$$I(0,z) = TI_0 e^{-\alpha z} \quad (3.19)$$

The Rayleigh ratio previously defined in Equation (3.10),



### Sample

Figure 11. Top View of the Sample Showing the Incident, Transmitted, and Scattered Light.



gives the value for the scattered intensity at the point  $(0, z)$  inside the sample,

$$I_s(0, z) = I(0, z) \left( \frac{d\sigma}{d\Omega} \right) \frac{1}{R^2} . \quad (3.20)$$

The scattered light at the point  $(x, z)$  inside the sample is,

$$I_s(x, z) = \pi I_o \left( \frac{d\sigma}{d\Omega} \right) \frac{1}{R^2} e^{-\alpha(x+z)} . \quad (3.21)$$

Outside the sample, the scattered light is,

$$I_s = I_o I_o' e^{-\alpha(x+z)} \quad (3.22)$$

where,

$$I_o' = \frac{\pi^2}{R^2} \left( \frac{d\sigma}{d\Omega} \right) . \quad (3.23)$$

As described in Chapter II, the photo-elastic constants were determined by comparing the Brillouin intensities of the glass samples to those of the standard fused quartz. This is done by first forming the ratio of the integrated intensity of the sample to that of fused quartz,

$$\beta = \frac{I_s}{I_s^0} = \frac{I_o I_o' e^{-\alpha(x+z)}}{I_o I_o' e^{-\alpha^0(x+z)}} \quad (3.24)$$

and then setting  $x = z = 0$ , so that Equation (3.24) reduces to,

$$\beta = \frac{I_o'}{I_o'^0} . \quad (3.25)$$

This is the quantity measured experimentally as described in detail in Chapter II. Using Equation (3.16a), Equation (3.23) and Equation (3.25) we arrive at an expression for the photo-elastic constant  $P_{12}$  of our glass sample in terms of the intensity ratio  $\beta$ ,

$$P_{12} = P_{12}^0 \left( \frac{V^0}{V} \right)^{\frac{1}{2}} \left( \frac{C_{11}}{C_{11}^0} \right)^{\frac{1}{2}} \left( \frac{n+1}{n^0+1} \right)^2 \left( \frac{n^0}{n} \right)^5 (\beta)^{\frac{1}{2}} . \quad (3.26)$$

Also used in the derivation of Equation (3.26) was the expression  $\epsilon = n^2$ . It is shown in Appendix B that the ratio of the volumes in the above expression is very nearly equal to one and can be neglected.

In the above discussion, no mention was made of the collection solid angle defined by the collection optics. That is, the amount of light received from the scattering volume, not only depends on the collecting optics but also on the index of refraction of the sample. It is shown in Appendix B that the solid angle correction to the intensity ratio in Equation (3.25) is such as to increase the measured intensity ratio  $\beta$ , by a factor of  $(n/n^0)^2$ .

In addition, the back reflection from the exit surface in the high absorbing glasses is not sufficient enough in intensity to compensate for that intensity lost due to reflection at the entrance surface. It is shown in Appendix B that this correction increases the intensity ratio  $\beta$  by,

$$\gamma = \frac{[1 + R^0 e^{-2\alpha^0 L^0}]}{[1 + R e^{-2\alpha L}]} \quad (3.27)$$

where  $R$  is the reflectivity,  $\alpha$  the absorption and  $L$  the length of the sample. The superscript "o" refers to the fused quartz values.

The value of  $\beta$  that should be used in Equation (3.26) is then,

$$\beta = \beta_{\text{meas.}} \left(\frac{n}{n^0}\right)^2 \gamma \quad (3.28)$$

As a result, Equation (3.26) for the photo-elastic

constant becomes,

$$P_{12} = P_{12}^0 \left( \frac{C_{11}}{C_{11}^0} \right)^{\frac{1}{2}} \left( \frac{n+1}{n^0+1} \right)^2 \left( \frac{n^0}{n} \right)^4 (\beta_{\text{meas.}} \nu)^{\frac{1}{2}} . \quad (3.29)$$

The expression for  $P_{44}$  can now be derived in terms of the TA to LA intensities of the sample,

$$P_{44} = P_{12} \left( \frac{V_{TA}}{V_{LA}} \right) \left[ 2 \left( \frac{I_{TA}}{I_{LA}} \right) \right]^{\frac{1}{2}} . \quad (3.30)$$

## CHAPTER IV

### EXPERIMENTAL RESULTS AND ANALYSIS

In this chapter we present the results of the Brillouin scattering experiments on the  $\text{Eu}^{3+}$ -doped glasses. In chapter V we will discuss these results in relation to what we think is physically happening in the glasses and to current theories of light scattering in glasses. In the first section of this chapter, the Brillouin shifts, velocities, and elastic constants will be discussed. In the next section, a discussion of the photo-elastic constants will be given. Included in each section will be discussions of quantities that can be determined from either the elastic constants or the photo-elastic constants. In addition, each section will include brief discussions in regards to error analysis for the different facets of the experiment.

#### Brillouin Shifts, Velocities, And Elastic Constants

The Brillouin shifts  $\Delta\omega_B$  were determined from the spectrum using Equation (2.5) on page 20,

$$\Delta\omega_B = \left( \frac{r}{L_{AS} + L_S} \right) \frac{1}{2d} \quad (4.1)$$

Table VII lists the average room temperature Brillouin shifts for all of the  $\text{Eu}^{3+}$ -doped silicate glasses. These values are the averages of at least 10 or more separate measurements. (Several different plate separations were used to insure that the Brillouin peaks were not overlapped into adjoining orders). The uncertainties were determined from the spread in the values by calculating the standard deviation. The uncertainties shown represent three standard deviations of the mean.

As can be seen, the TA and LA Brillouin shifts decrease by about 24% and 22% respectively as the modifier ion is changed through the series Li, Na, K, Rb, and Cs.

The units normally used for the Brillouin shifts are  $\text{cm}^{-1}$ . To express the Brillouin shifts in the more familiar frequency units of Hertz, all one needs to do is multiply by the speed of light in centimeters per second. Thus the frequencies of the acoustic phonons measured in these experiments are on the order of  $10^{10}\text{Hz}$  as compared to the laser frequency of around  $10^{14}\text{Hz}$ .

Table VIII lists the acoustic velocities calculated from the average Brillouin shifts using Equation (2.1) on page 15,

$$v = \frac{\lambda_0 c \Delta\omega_B}{4n\pi \cdot \sin\left(\frac{\phi}{2}\right)} \quad (4.2)$$

The uncertainties in the velocities are the result of a standard error analysis incorporating the measurement uncertainties in the Brillouin shifts  $\Delta(\Delta\omega)$ , indices of

TABLE VII  
ROOM TEMPERATURE BRILLOUIN SHIFTS

Sample	$\Delta\omega_{TA}$ ( $\text{cm}^{-1}$ )	$\Delta\omega_{LA}$ ( $\text{cm}^{-1}$ )
$\text{Li}_2\text{O-SiO}_2$	$0.489 \pm 0.007$	$0.833 \pm 0.009$
$\text{Na}_2\text{O-SiO}_2$	$0.446 \pm 0.002$	$0.767 \pm 0.001$
$\text{K}_2\text{O-SiO}_2$	$0.423 \pm 0.004$	$0.736 \pm 0.002$
$\text{Rb}_2\text{O-SiO}_2$	$0.395 \pm 0.001$	$0.687 \pm 0.001$
$\text{Cs}_2\text{O-SiO}_2$	$0.370 \pm 0.004$	$0.654 \pm 0.001$

TABLE VIII  
ROOM TEMPERATURE SOUND VELOCITIES

Sample	$V_{TA}$ ( $10^5$ cm/s)	$V_{LA}$ ( $10^5$ cm/s)
$\text{Li}_2\text{O-SiO}_2$	$3.31 \pm 0.05$	$5.66 \pm 0.05$
$\text{Na}_2\text{O-SiO}_2$	$3.07 \pm 0.05$	$5.29 \pm 0.05$
$\text{K}_2\text{O-SiO}_2$	$2.91 \pm 0.05$	$5.07 \pm 0.05$
$\text{Rb}_2\text{O-SiO}_2$	$2.74 \pm 0.05$	$4.76 \pm 0.05$
$\text{Cs}_2\text{O-SiO}_2$	$2.54 \pm 0.05$	$4.48 \pm 0.05$

refraction  $\Delta n$  and the scattering angle  $\Delta\phi$ . The error equation is given by,

$$\frac{\Delta v}{v} = \frac{\Delta(\Delta\omega)}{\Delta\omega} + \frac{\Delta n}{n} + \frac{\cos\frac{\phi}{2}}{2\sin\frac{\phi}{2}}\Delta\phi \quad (4.3)$$

where  $\Delta v$  is the uncertainty in the velocity due to the uncertainties in the directly measured quantities  $\Delta\omega$ ,  $n$ , and  $\phi$ . The values used for the measurement uncertainties are as follows;  $\Delta(\Delta\omega) = \pm 0.004\text{cm}^{-1}$  for the TA mode and  $\pm 0.002\text{cm}^{-1}$  for the LA mode,  $\Delta n = \pm 0.005$  and  $\Delta\phi = \pm 0.068\text{rad}$  ( $\sim 4^\circ$ ). The value used for  $\Delta\phi$  is the result of the analysis of the solid angle of collection given at the end of Appendix B. As it turns out the last term in Equation (4.1) dominates over the other two terms. It is more than ten times larger and as a result the uncertainty in the velocity is primarily due to the scattering solid angle.

Both acoustic velocities decrease by about the same percentage as do their respective Brillouin shifts reflecting the fact that the indices of refraction for the glasses vary by only about 2%.

In Table IX the elastic constants are listed as calculated from Equation (2.2) on page 15,

$$C = \rho v^2 \quad (4.4)$$

The uncertainties were determined in the same way as for the velocities using for  $\Delta\rho = \pm 0.03\text{g/cm}^3$ .

TABLE IX  
ROOM TEMPERATURE ELASTIC CONSTANTS

Sample	$C_{44}$ ( $10^{10}$ dyne/cm <sup>2</sup> )	$C_{11}$ ( $10^{10}$ dyne/cm <sup>2</sup> )
Li <sub>2</sub> O-SiO <sub>2</sub>	35.3 ± 0.5	103.5 ± 0.5
Na <sub>2</sub> O-SiO <sub>2</sub>	30.2 ± 0.5	89.5 ± 0.5
K <sub>2</sub> O-SiO <sub>2</sub>	26.7 ± 0.5	81.0 ± 0.5
Rb <sub>2</sub> O-SiO <sub>2</sub>	26.0 ± 0.5	78.7 ± 0.5
Cs <sub>2</sub> O-SiO <sub>2</sub>	24.1 ± 0.5	75.2 ± 0.5



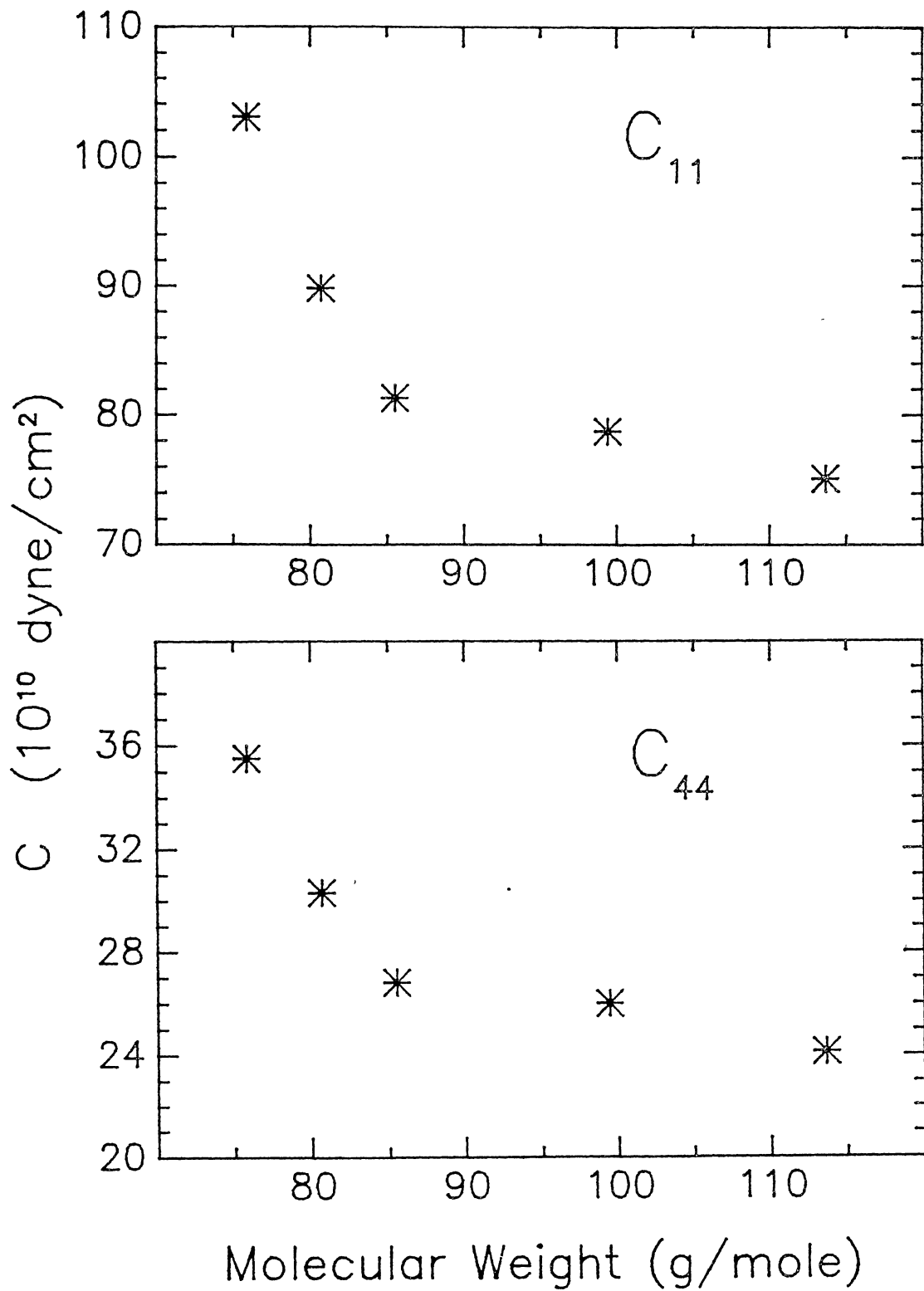


Figure 12. Elastic Constants Versus the Molecular Weight of the Glasses.

Both elastic constants,  $C_{11}$  and  $C_{44}$  show a gradual decrease of approximately 27% and 32% respectively as the size and mass of the modifier ion increases through the series Li, Na, K, Rb, and Cs. In Figure 12 the LA and TA elastic constants are graphed versus the molecular weight of the glass samples.

There are several quantities that can be calculated from the elastic constants. The first of these is Young's modulus, the ratio of the applied stress to the fractional change in dimension. In terms of the elastic constants, Young's modulus is given by (Christman (1988)),

$$Y = \frac{C_{44}(3C_{11}-4C_{44})}{(C_{11}-C_{44})} \quad (4.5)$$

The second is Poisson's ratio, the measure of the change in dimensions perpendicular to the direction of the applied force. Poisson's ratio is given by (Christman (1988)),

$$\sigma = \frac{(C_{11}-2C_{44})}{2(C_{11}-C_{44})} \quad (4.6)$$

The third quantity is the adiabatic bulk modulus, the reciprocal of the compressibility. The compressibility is defined as the fractional change in volume due to an applied pressure. The bulk modulus is given by (Christman (1988)),

$$\beta = C_{11} - \frac{4}{3}C_{44} \quad (4.7)$$

Table X shows the calculated values of these quantities for the five glasses along with some other materials for

TABLE X  
 BULK MODULUS, YOUNG'S MODULUS AND  
 POISSON'S RATIO

Sample	Adiabatic Bulk Modulus ( $10^{10}$ dyne/cm <sup>2</sup> )	Young's Modulus ( $10^{10}$ dyne/cm <sup>2</sup> )	Poisson's Ratio
Li <sub>2</sub> O-SiO <sub>2</sub>	56.1	87.4	0.24
Na <sub>2</sub> O-SiO <sub>2</sub>	49.3	75.2	0.24
K <sub>2</sub> O-SiO <sub>2</sub>	45.4	67.0	0.25
Rb <sub>2</sub> O-SiO <sub>2</sub>	44.0	65.3	0.25
Cs <sub>2</sub> O-SiO <sub>2</sub>	43.1	60.9	0.26
SiO <sub>2</sub>	37.2 <sup>1</sup>	73.2 <sup>1</sup>	0.17 <sup>1</sup>
SiO <sub>2</sub>	36.57 <sup>2</sup>	72.45 <sup>2</sup>	0.170 <sup>2</sup>
B <sub>2</sub> O <sub>3</sub>	12.83 <sup>2</sup>	15.37 <sup>2</sup>	0.300 <sup>2</sup>

<sup>1</sup>This report

<sup>2</sup>Schroeder (1977)

comparison. As can be seen, Young's modulus and the adiabatic bulk modulus both decrease as the size of the modifying ion is increased. Poisson's ratio on the other hand, increases very slightly.

#### Photo-Elastic Constants

Table XI lists the measured photo-elastic constants for the five glasses.  $P_{12}$  and  $P_{44}$  were measured directly from the vertical-unpolarized Brillouin spectrum as described in Chapters II and III, whereas  $P_{11}$  was determined from the Cauchy relation,

$$P_{11} = 2P_{44} + P_{12} . \quad (4.8)$$

The photo-elastic constants for other materials are also shown in Table XI for comparison. The uncertainties are not shown but are estimated to be approximately 10%.

Figure 13 is a plot of the photo-elastic constants versus the molecular weight of the glasses. Except for the decrease in going from Na to K,  $P_{12}$  increases by about 31% from Li to Cs, and  $P_{44}$  increases, though not continuously, by about 35%. However, we have assumed here that  $P_{44}$  is negative consistent with that found in most glasses (Schroeder (1980)). (More will be said on this in Chapter V in relation to Carleton's theory of photoelasticity). The absolute value of  $P_{44}$  decreases reflecting the fact that the intensity of the TA peaks actually decreases as the size of the modifier ions is increased.

TABLE XI  
ROOM TEMPERATURE PHOTO-ELASTIC CONSTANTS

Sample	$P_{12}$	$ P_{44} $	$P_{11}$
$\text{Li}_2\text{O-SiO}_2$	0.191	0.0518	0.087
$\text{Na}_2\text{O-SiO}_2$	0.230	0.0520	0.126
$\text{K}_2\text{O-SiO}_2$	0.207	0.0410	0.125
$\text{Rb}_2\text{O-SiO}_2$	0.244	0.0428	0.158
$\text{Cs}_2\text{O-SiO}_2$	0.251	0.0339	0.183
Fused quartz	0.270 <sup>1</sup>		0.126 <sup>1</sup>
Fused quartz	0.279 <sup>2</sup>		0.121 <sup>2</sup>
Dense flint	0.256 <sup>3</sup>		0.232 <sup>3</sup>
Water	0.31 <sup>3</sup>		0.31 <sup>3</sup>
Lucite	0.28 <sup>3</sup>		0.30 <sup>3</sup>
Polystyrene	0.31 <sup>3</sup>		0.30 <sup>3</sup>
Toluene	0.322 <sup>2</sup>		

<sup>1</sup>Schroeder (1980)

<sup>2</sup>This report

<sup>3</sup>Pinnow (1972)

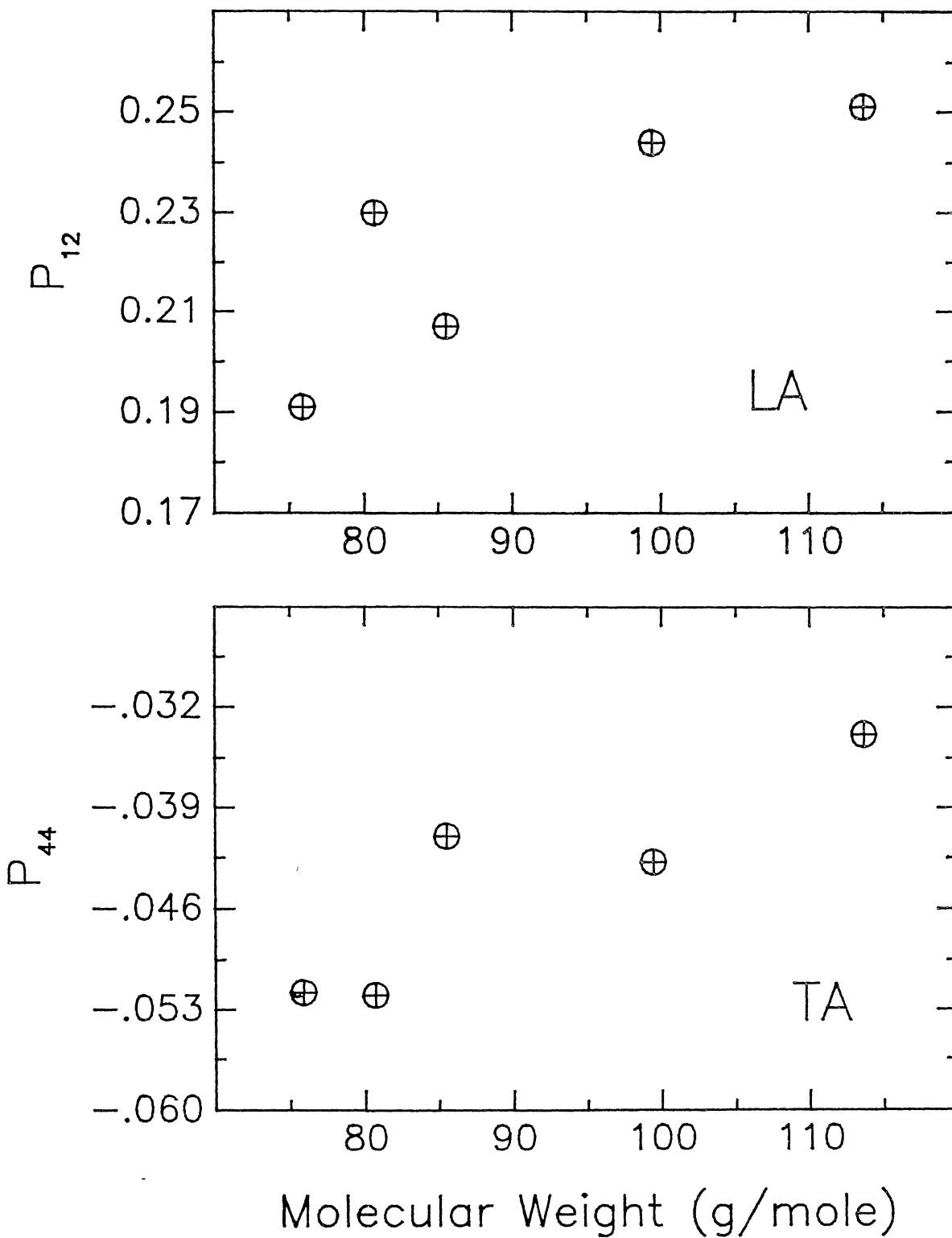


Figure 13. Photo-Elastic Constants Versus the Molecular Weight of the Glasses.

Other quantities of interest related to the intensities are the Landau-Placzek ratio and the Rayleigh and Brillouin scattering losses. The Landau-Placzek ratio is given by,

$$R_{LP} = \frac{I_R}{2I_{LA}} \quad (4.9)$$

where  $I_R$  is the integrated intensity of the Rayleigh line and  $I_{LA}$  is the total integrated intensity of the longitudinal Brillouin peaks. Table XII shows the results for our glasses and for some other materials as well. As can be seen, the Landau-Placzek ratio decreases steadily from Li to Cs. In the  $\text{Li}_2\text{O-SiO}_2$  glass, the Rayleigh scattering was so intense that neutral density filters had to be used during the experiments to prevent flooding of the photomultiplier tube. In the  $\text{K}_2\text{-SiO}_2$  glass, there were numerous flares making it difficult, but not impossible, to find a quiet spot for the location of the scattering volume. Bright flares of this kind were absent from the other glasses. In all cases the value listed in Table XII for  $R_{LP}$  is the smallest value obtained after many runs.

The Brillouin scattering loss is given by (Schroeder (1977)),

$$\alpha_B = \frac{8\pi^3}{3} \frac{K_B T}{\lambda^4} (n^4 p_{12})^2 \frac{1}{\rho v_{LA}^2} \quad (4.10)$$

where  $\lambda$  is the laser wavelength,  $\rho$  is the density,  $K_B$  is Boltzmann's constant,  $T$  is the absolute temperature,  $n$  the index of refraction, and  $v_{LA}$  is the longitudinal acoustic velocity. From Table XII we see that  $\alpha_B$  increases by

TABLE XII  
 LANDAU-PLACZEK RATIOS AND ATTENUATION  
 COEFFICIENTS

Sample	$R_{LP}$	$\alpha_B$ ( $\text{cm}^{-1}$ )	$\alpha_S$ ( $\text{cm}^{-1}$ )
$\text{Li}_2\text{O-SiO}_2$	23500	0.336	7890
$\text{Na}_2\text{O-SiO}_2$	109	0.491	66.7
$\text{K}_2\text{O-SiO}_2$	87.9	0.442	59.8
$\text{Rb}_2\text{O-SiO}_2$	54.5	0.613	34.5
$\text{Cs}_2\text{O-SiO}_2$	39.0	0.724	31.1
$\text{SiO}_2$	21.6	0.404	9.13



over 100% from Li to Cs, even though it decreases slightly from Na to K.

The Rayleigh scattering loss is given by (Schroeder (1977)),

$$\alpha_R = \alpha_B (R_{LP} + 1) \quad (4.11)$$

with values listed in Table XII. The Rayleigh scattering loss decreases from Li to Cs. The units for  $\alpha_B$  and  $\alpha_S$  are  $\text{cm}^{-1}$ . Alternatively, they can be expressed in decibels per kilometer by multiplying by  $4.34 \times 10^5$ .

The acousto-optic figure-of-merit is a quantity that appears in a number of expressions describing photo-elastic interactions in materials (Pinnow (1972)). The figure-of-merit, measured relative to some standard, characterizes a material as to its suitability for use as control devices such as laser beam deflectors, light modulators, and Q-switches requiring a large photo-elastic interaction and large figure-of-merit, or as solid-state laser hosts and glass used for lenses both requiring a small interaction.

There are three different forms of the figure-of-merit, they are,

$$\begin{aligned} M_1 &\equiv \frac{n^7 p^2}{\rho v} \\ M_2 &\equiv \frac{n^6 p^2}{\rho v^3} \\ M_3 &\equiv \frac{n^7 p^2}{\rho v^2} \end{aligned} \quad (4.5)$$

It is common practice to express the figures-of-merit relative to fused quartz. Expressed in this way  $M_1$ ,  $M_2$ , and  $M_3$  are all set equal to one for fused quartz.

TABLE XIII  
FIGURES-OF-MERIT

Sample	$M_1$ (X $7.88 \times 10^{-7}$ )	$M_2$ (X $1.51 \times 10^{-18}$ )	$M_3$ (X $1.32 \times 10^{-12}$ )
$\text{Li}_2\text{O-SiO}_2$	0.69	0.70	0.73
$\text{Na}_2\text{O-SiO}_2$	0.98	1.2	1.1
$\text{K}_2\text{O-SiO}_2$	0.85	1.1	1.0
$\text{Rb}_2\text{O-SiO}_2$	1.1	1.6	1.4
$\text{Cs}_2\text{O-SiO}_2$	1.2	2.0	1.6
<hr/>			
Fused quartz		1.0	
Dense flint		3.0 <sup>1</sup>	
Water		106 <sup>1</sup>	
Lucite		33 <sup>1</sup>	
Polystyrene		84 <sup>1</sup>	

<sup>1</sup>Pinnow (1972)

As can be seen in Table XIII, the figures-of-merit increase from Li to Cs but are not much larger than that of fused quartz. The figures-of-merit for some other isotropic materials, listed in the literature, are also shown for comparison. The conclusion is that the five glasses studied in our experiments are not well suited for acousto-optical applications that require a large photo-elastic interaction.

### Optical Absorption

Because of absorption, the intensity of the scattered light will depend on where the scattering volume is located within the sample. As a result, the absorption had to be taken into account when measuring the intensity ratios. The optical absorption was the largest for the  $K_2O-SiO_2$  glass and decreased in the series  $Na_2O-SiO_2$ ,  $Li_2O-SiO_2$ ,  $Cs_2O-SiO_2$ , and  $Rb_2O-SiO_2$ . Figure 14 shows a plot of  $\ln\left(\frac{I_s}{I_0}\right)$  vs.  $h$  for the five glasses. In this plot  $I_s$  is the scattered intensity of the LA peaks for a scattering volume at some position  $h$  within the sample. (The coordinate  $h$  is the sum of  $x$  and  $z$  where  $x$  is the distance the scattered light travels through the sample from the scattering volume to the exit surface and  $z$  is the distance the center of the scattering volume is from the entrance surface).  $I_0$  is the scattered intensity extrapolated to  $h = 0$ . The procedure used to do this is discussed in Chapter II. When the intensities are plotted

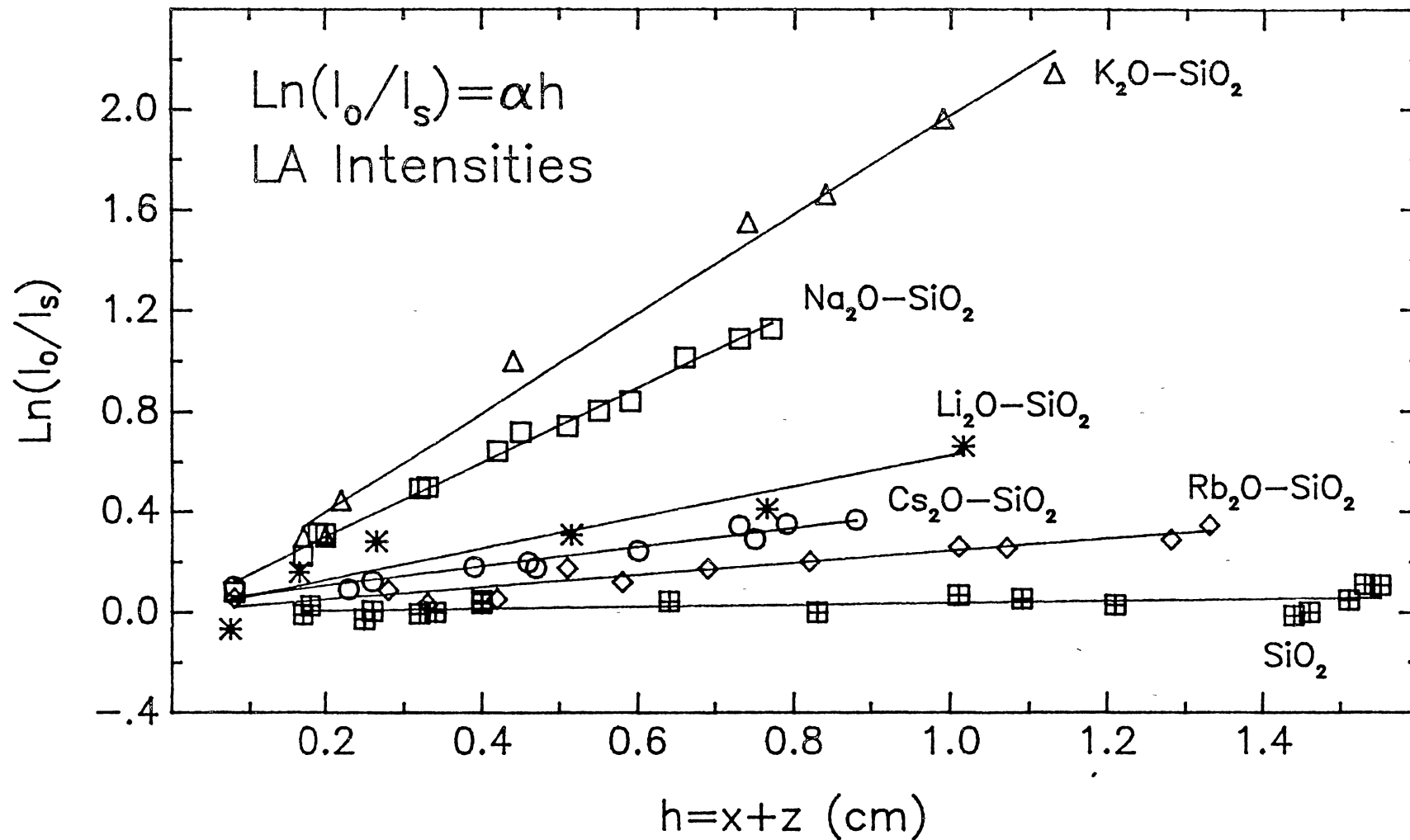


Figure 14. Natural Logarithm of  $I_s/I_0$  Versus  $h$ .  
 The Slope of the Line is Equal to the  
 Coefficient of Absorption of the Glass.

in this way the slope of the line is equal to the  
absorption coefficient  $\alpha$ .

## CHAPTER V

### DISCUSSION AND SUMMARY

The purpose of this chapter is to discuss the results of Brillouin scattering experiments in the  $\text{Eu}^{3+}$ -doped glasses in relation to what we think is physically responsible for the behavior of the data. Also included in this chapter is a discussion of the structure and properties of binary alkali silicate glasses.

Understanding the effects of changing the alkali ion in the base glass may help us in understanding these effects in our more complicated glasses. Finally in the last few sections we discuss the physical interpretation of the results of Brillouin scattering in these glasses. But first a description of the structure of fused quartz, which forms the base material for all of our glasses. Each glass studied for this dissertation contained 70%  $\text{SiO}_2$ .

#### Fused Quartz

Fused quartz has been studied extensively for many years, primarily because of its technological importance and its relatively simple composition (Kreidl (1983)). Fused quartz consists of a three dimensional network of

$\text{SiO}_4$  tetrahedra (Figure 15). Most of the tetrahedra in the network are bonded to four other tetrahedra at the O corners. These O atoms are referred to as bridging oxygens. The main difference between fused quartz and the crystalline form of  $\text{SiO}_2$  is the lack of repetitive orientation of the  $\text{SiO}_4$  tetrahedra. Fused quartz studies have shown that the most probable number of Si atoms in a ring of tetrahedra is five (Kreidl (1983)).

The bonding between the Si and O is believed to be mostly covalent in nature, however other bonding schemes may be involved as well. These include the double bond  $\text{O}=\text{Si}=\text{O}$  and the pure ionic bond  $\text{Si}^{4+}(\text{O}^{2-})_4$  (Kreidl (1983)). Some of the important distances in the  $\text{SiO}_2$  network are the Si-O (1.62Å), O-O (2.65Å), and Si-Si (3.12Å) bond lengths. The most probable Si-O-Si angle is  $144^\circ$  and the most probable O-Si-O angle is  $109^\circ$  with most angles being within 10% of these values.

#### Alkali Silicate Glasses

Most of the important glasses used today are silicate glasses that contain several different kinds of oxides (Kreidl (1983)). Binary glasses of the form  $\text{M}_2\text{O}-\text{SiO}_2$  where M = Li, Na, K, Rb, and Cs, limited in use due to their reactivity to water, have been studied in detail because of their relatively simple structure and to the insights they provide to the structure and properties of silicate glasses in general. In this section we present

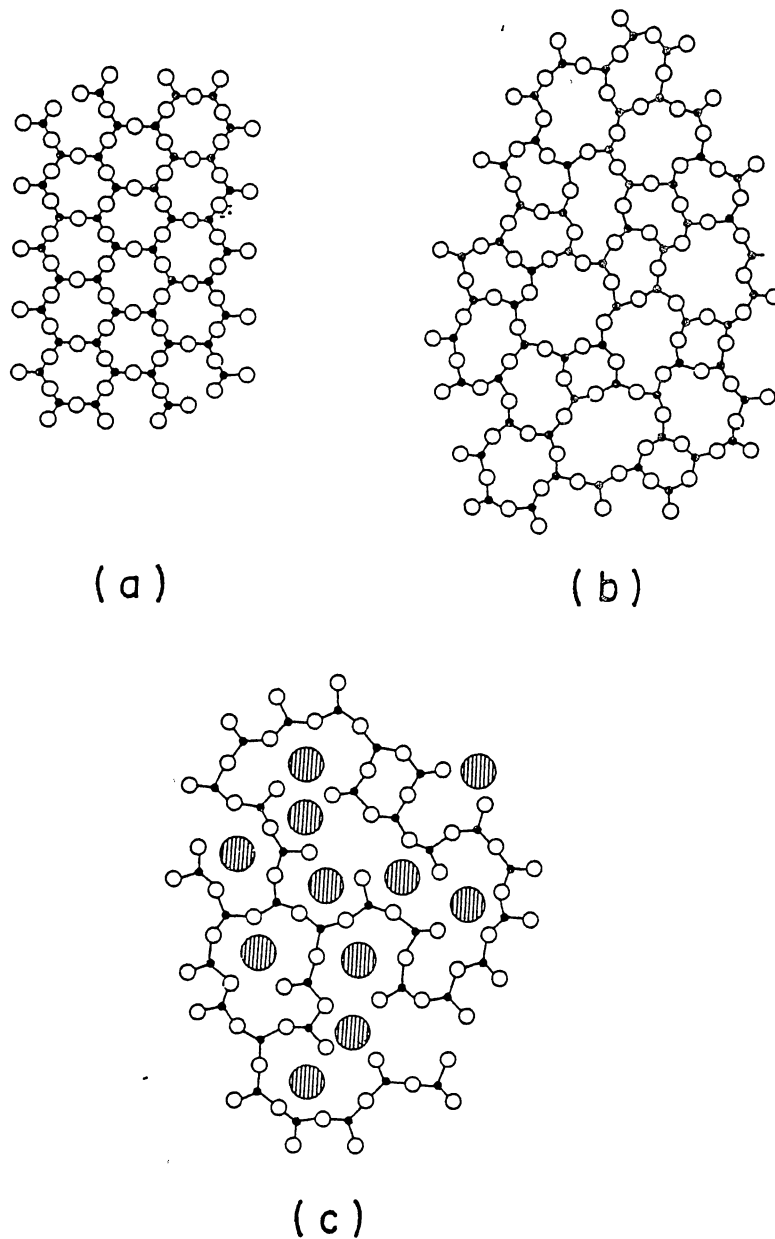


Figure 15. Two-Dimensional Schematic of the Structures of (a) Crystalline  $\text{SiO}_2$ , (b)  $\text{SiO}_2$  Glass, and (c)  $\text{M}_2\text{O-SiO}_2$  Glass. The Small Solid Circles are the Silicon Atoms, Open Circles the Oxygen Atoms, and the Large Shaded Circles the Alkali Atoms.



some of the results of studies on these binary silicate glasses. Most of the material in this section was taken from Kreidl (1983) who did an extensive review of studies in silicate glasses.

For each alkali oxide  $M_2O$  molecule added to  $SiO_2$ , an extra oxygen is added to the network and two non-bridging oxygens are produced (Figure 15). A non-bridging oxygen is an O bonded to only one Si atom instead of two as in pure  $SiO_2$ . Also bonded to the non-bridging oxygen is the cation  $M^+$  which tends to fill-up the cavities created by the tetrahedra rings. The distribution of alkali within the  $SiO_4$  network may not be uniform (Sigel (1977)), giving rise to regions of alkali rich clusters surrounded by mostly  $SiO_2$  regions.

In general the addition of  $M_2O$  serves to weaken the structure due to the appearance of the non-bridging oxygens. Increasing the concentration of  $M_2O$ , further weakens the structure until all the oxygens are non-bridging and the tetrahedra are isolated from each other. This weakening effect is more pronounced as the size of the alkali ion is increased. (Incidentally this effect is confirmed by our elastic constant values).

Measurements of the molar volume of binary alkali silicate glasses have shown that Na mostly fills the cavities of the  $SiO_4$  network, while Li additionally contracts the network because of its large field strength and small size while K, Rb, and Cs act to expand the

network. In general the density of alkali silicate glasses increases with increasing alkali concentration and increases with increasing mass of the alkali ion as the ions fill the cavities of the  $\text{SiO}_4$  network.

These observations on the molar volume in binary alkali silicate glasses are consistent with our measurements of the density of our glasses as shown in Table III on page 16. As can be seen, the density decreases slightly from Li to K before increasing noticeably from K to Cs. If the ions were simply filling the cavities without any distortion of the  $\text{SiO}_4$  network then the density would increase in the direction Li, Na, K, Rb, and Cs.

The index of refraction is generally higher in the alkali silicate glasses compared to pure fused quartz because of the higher polarizability of the alkali compared to oxygen and silicon and the higher polarizability of non-bridging oxygens. As a result, the index generally increases with increased concentration of the alkali ions. Lithium silicate glasses have relatively large indices of refraction due to their low molar volume. In our glasses the Li sample has the highest index of refraction with a value of 1.604 with the Rb sample with the smallest value measuring in at 1.573. Fused quartz, on the other hand, has an index of refraction of 1.462.

### Visible Absorption

Visible absorption in the glasses studied for this dissertation is believed to be due mostly, if not entirely, to the Eu ions (Dixon (1989)).  $\text{SiO}_2$  and alkali ions in  $\text{SiO}_2$  contribute to ultraviolet absorption (Sigel (1977)). However, different types of alkali ions may change the characteristics of the absorption due to the Eu ions (Vogel (1985)). Sigel reviewed the affect rare earth ions have on the visible absorption in oxide glasses. Each one of our glasses has 5% per mole  $\text{Eu}_2\text{O}_3$ . According to a table found in Sigel,  $\text{Eu}^{3+}$  in oxide glasses should produce no colorations while  $\text{Eu}^{2+}$  would produce a characteristic brown color. All of our glasses are brown with the K glass being the darkest followed by Na, Li, Cs, and Rb. Furthermore, there is a lack of uniformity in color and shading in some of the glasses noticeably the Li and Na samples. In fact the Li sample has blue streaks running through it, an indication of phase separation (Powell (1987)). If the Eu ion is the only source of absorption in these glasses then we could conclude that the K glass has the highest concentration of  $\text{Eu}^{2+}$  with Rb the least. On the other hand, the alkali ions may also be affecting the absorption to produce the observed colorations.

## Elastic Constants

As was mentioned in the last chapter, both elastic constants decrease as the size of the modifying ion is increased through the series Li, Na, K, Rb, and Cs (Table IX page 57). This decrease can be attributed to the decrease in field strength and the increase in size of the modifying ions from Li to Cs. This is consistent with results in simpler alkali silicate glasses discussed earlier. In the binary glasses, the weakening of the structure due to the appearance of non-bridging oxygens is amplified with increasing size of the alkali ion.

Young's modulus is defined as the ratio of the applied stress to the fractional change in dimension along the direction of the applied stress. Young's modulus decreases by about 30% from Li to Cs indicating that the glasses are becoming more elastic as the mass of the modifying ion is increased (Table X on page 60).

Born and Huang (1954) have shown that if each particle of a material is located at a center of symmetry and if the particles interact with each other through central forces then the so called Cauchy relation holds for cubic and isotropic materials,  $C_{12} = C_{44}$  ( $C_{11} = 3C_{44}$ ). None of the glasses studied in this report have the ratio  $C_{44}/C_{12}$  exactly equal to one. There is a general decrease in this ratio from Li to Cs with a value of 1.09 for the Li glass to 0.893 for the Cs glass. In pure  $\text{SiO}_2$  this

ratio is 1.89 reflecting the predominance of covalent bonding and the presence of non-central forces. The fact that this ratio is closer to one for our glasses may indicate an increase in the number of ionic bonds as a result of the additions of the modifying ions.

Poisson's ratio defined as the fractional change in dimension in the direction of the applied stress to the fractional change in dimension perpendicular to the applied stress can also be used as a measure of the degree of non-central forces and covalent bonding. If the Cauchy relation holds then Poisson's ratio reduces to 0.25 exactly. In covalently bonded fused quartz, Poisson's ratio is equal to 0.172 and in our samples it ranges from 0.240 for the Li glass to 0.264 for Cs (Table X on page 60).

#### Photo-Elastic Constants

In Chapter IV we pointed out that both photo-elastic constants showed a general increase as the size of the modifying ion was increased (Table XI on page 62). As we will see, unlike  $P_{12}$ ,  $P_{44}$  is negative. So an increase in value for  $P_{44}$  translates into a decrease in its absolute value. Referring to Equation (3.12), an increase in  $P_{12}$  indicates that the fluctuation of the dielectric constant, as a result of compressional sound waves, increases as the size and mass of the modifying ion increases. As for shear waves, the fluctuation of the dielectric constant decreases.

In the remainder of this section one of the few theoretical treatments found in the literature for the photo-elastic constants of glasses will be discussed. This model had its beginning with the dielectric formalism of Kirkwood and Yvon and was later extended to optical frequencies by Fixman (1955) and further refined by Carleton (1972). The model is for simple materials of optically isotropic and non-polar molecules. It is assumed that the location of each polarizable center is known and given by a number of multiparticle correlation functions. Even though the model is strictly applicable to simple materials, Carleton suggested that it could help characterize some of the features of more complex materials. Carleton derived expressions for the three photo-elastic constants  $P_{11}$ ,  $P_{12}$ , and  $P_{44}$

$$P_{11} = \frac{(n^2-1)^2}{n^4} \left( \frac{M}{4\pi\alpha\rho N_A} + \frac{4}{15} - \frac{14}{15} r \right) \quad (5.1)$$

$$P_{12} = \frac{(n^2-1)^2}{n^4} \left( \frac{M}{4\pi\alpha\rho N_A} - \frac{2}{15} - \frac{8}{15} r \right) \quad (5.2)$$

$$P_{44} = \frac{(n^2-1)^2}{n^4} \left( \frac{1}{5} - \frac{1}{5} r \right) \quad (5.3)$$

where  $n$  is the index of refraction,  $\alpha$  the free particle polarizability,  $\rho$  is the particle density,  $M$  is the molecular weight of the glass,  $N_A$  is Avogadro's number, and the correlation term  $r$ , in cgs units, is given by,

$$r = 3\alpha \int_0^{\infty} g_{12}(r) \frac{dr}{r^4} \quad (5.4)$$

where  $g_{12}(r)$  is a two particle radial distribution function such that  $\alpha g(r)$  = average polarizability at  $\vec{r}$  given that a particle is at the origin (Chandler (1987)).

The first term of Equations (5.1) and (5.2) represents the change in the dielectric constant with density produced by the strain caused by the propagating phonons. This term does not appear in Equation (5.3) for  $P_{44}$ . This can be explained in the following way. For a longitudinal wave the average distance between atoms, in a localized region of the sample, changes as the wave moves through the material. We would then expect that the photo-elastic constants for compressional waves should depend on the density of the glass. On the other hand, the average distance between atoms does not change as a transverse wave moves through this same localized region and we would not expect the photo-elastic constant for the shear waves to be as density dependent. The second term in Equations (5.1) and (5.2) and the first term in Equation (5.3) is due to the anisotropic correction to the refractive index as a result of the elliptical distortion of the Lorentz cavity as a result of the strain produced by the phonons. The third term is the result of the additional polarizing effect of neighboring molecules on each other.

Schroeder (1980) measured the photo-elastic constants for a number of binary and ternary silicate based glasses. The density of a particular type of glass was

varied by changing the concentration of the modifying ion. Schroeder found that for the binary glasses,  $P_{44}$  showed some linear density dependence, decreasing slightly as the density increased, but not as much as for  $P_{12}$ . On the other hand for the ternary glasses,  $P_{44}$  showed no density dependence, consistent with Equation (5.3), while  $P_{12}$  decreased linearly with increasing density.

In order to test Carleton's expressions for the photo-elastic constants with our data, we first calculated  $r$  from Equation (5.3) using our values for  $P_{44}$ . Then using Equation (5.2) and our values for  $P_{12}$ , we calculated the first expression inside the brackets involving the molecular weight of the glasses  $M$ . From this we were able to obtain values for the average polarizability of each sample. Table XIV shows the measured values needed for each sample in order to do the calculations just described. In Table XV the results of these calculations are shown.

The average polarizability of the material shows an increase of about 20% in the direction Li to Cs. The polarizability is density dependent and one would expect that as the density increases the polarizability would decrease (Schroeder (1980)). However, the electronic polarizabilities of the isolated ions  $\text{Li}^+$ ,  $\text{Na}^+$ ,  $\text{K}^+$ ,  $\text{Rb}^+$ , and  $\text{Cs}^+$  show a large increase from Li to Cs (Kittel (1986)). At the same time, the density of our samples



Table XIV  
 QUANTITIES USED IN THE EXPRESSIONS  
 FOR THE PHOTO-ELASTIC CONSTANTS

Sample	n	$\rho$ (g/cm <sup>3</sup> )	M (g)	P <sub>12</sub>	P <sub>44</sub>	P <sub>11</sub>
Li <sub>2</sub> O-SiO <sub>2</sub>	1.604	3.22	75.87	0.191	-0.0518	0.087
Na <sub>2</sub> O-SiO <sub>2</sub>	1.583	3.21	80.69	0.230	-0.0520	0.126
K <sub>2</sub> O-SiO <sub>2</sub>	1.584	3.15	85.52	0.207	-0.0410	0.125
Rb <sub>2</sub> O-SiO <sub>2</sub>	1.573	3.47	99.43	0.244	-0.0428	0.158
Cs <sub>2</sub> O-SiO <sub>2</sub>	1.591	3.74	113.66	0.251	-0.0339	0.183
SiO <sub>2</sub>	1.462	2.207	60.08	0.279	-0.0792	0.121

TABLE XV  
 NUMERICAL VALUES FOUND IN THE EXPRESSIONS  
 FOR THE PHOTO-ELASTIC CONSTANTS

Sample	$\frac{(n^2-1)^2}{n^4}$	$\frac{M}{4\pi\alpha\rho N_A}$	$\alpha$ (X10 <sup>-24</sup> cm <sup>3</sup> )	$\Gamma$	$\frac{\Gamma}{3\alpha}$ (X10 <sup>23</sup> cm <sup>-3</sup> )
Li <sub>2</sub> O-SiO <sub>2</sub>	0.374	1.54	2.01	1.69	2.80
Na <sub>2</sub> O-SiO <sub>2</sub>	0.361	1.69	1.96	1.72	2.92
K <sub>2</sub> O-SiO <sub>2</sub>	0.362	1.54	2.32	1.57	2.26
Rb <sub>2</sub> O-SiO <sub>2</sub>	0.355	1.67	2.26	1.60	2.36
Cs <sub>2</sub> O-SiO <sub>2</sub>	0.366	1.60	2.51	1.46	1.94
SiO <sub>2</sub>	0.283	2.40	1.50	2.40	5.33

increases from K to Cs by about 16% which would act to decrease the polarizability from that which would be expected if the density were the same for each sample. The large increase in polarizability from Li to Cs should dominate over the density effect. As a result, the increase in average polarizability of our samples from Li to Cs, as determined from the Carleton relations, is not unreasonable.

The average polarizabilities of the samples are larger than the average polarizability of fused quartz. This should be expected since the polarizability of the modifying ions is larger than that of Si and O. Also, the polarizability of non-bridging oxygens is greater than bridging oxygens.

The correlation term  $r$ , as determined from  $P_{44}$ , shows a decrease in value of about 14% from Li to Cs. In order to understand the significance of this decrease in terms of structural changes in the glass, we rewrite Equation (5.4) as,

$$\int_0^{\infty} g_{12}(r) \frac{dr}{r^4} = \frac{r}{3\alpha} . \quad (5.5)$$

As was stated above,  $r$  decreases and  $\alpha$  increases in the direction from Li to Cs. The measurements of  $r$  and  $\alpha$  indicate that the integral in Equation (5.5) fluctuates slightly but overall decreases by 28% from Li to Cs. In fused quartz the value of the integral is almost twice as much as that for any of our glass samples. It is natural

to ask if these results are consistent with what is currently known about fused quartz and glass systems similar to ours. The  $r^{-4}$  in the integrand of the integral indicates that the integral will be significant only out to about next nearest neighbor distances. What short range structural changes, as alkali oxide is added to the  $\text{SiO}_2$  network, would lead to a decrease in the value of the integral of Equation (5.5)?

Tesar et al. (1987) studied the structure of  $\text{M}_2\text{O-SiO}_2$  ( $\text{M} = \text{Li, Na, K}$ ) glasses using the method of molecular dynamic computer simulation. Their results were reported to be consistent with x-ray and infrared experimental results on the same kinds of systems (Kreidl (1983)). They calculated and studied the radial distribution function  $g(r)$  and coordination numbers for the various ion pairs as a function of composition. They found that within a given system, increasing the amounts of alkali oxide had minimal effects on the structure. However, both the number of non-bridging oxygens and the oxygen coordination of the alkali ions increased with increased concentration of alkali.

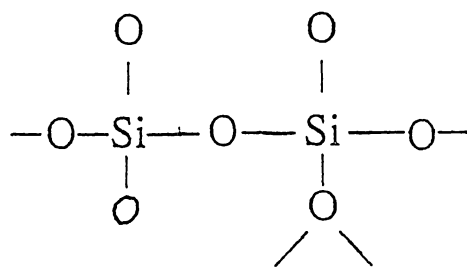
The peak corresponding to the shortest distance in their radial distribution function was attributed to the Si-O bond length and the peak with the second shortest distance was assigned to the M-Si bond length. In going from Li to K, they found that the bond lengths between the oxygens and the alkali ions increased. This would lead to

a decrease of the integral in Equation (5.5) consistent with our results.

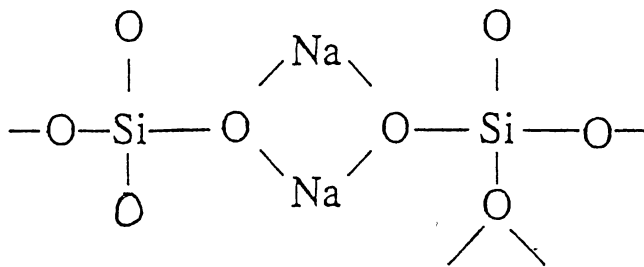
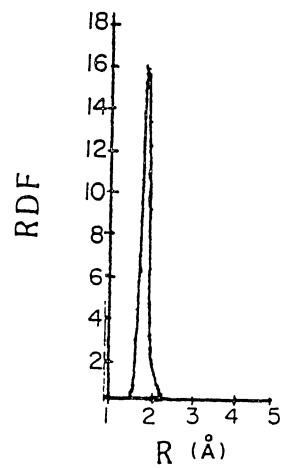
Murray et al. (1987) and Soules (1979) studied structural models of  $\text{NaO}_2\text{-SiO}_2$  glasses using computer simulations. They found that the radial distribution function changed significantly at small  $r$  as sodium oxide was introduced into the pure  $\text{SiO}_2$  network (Figure 16).

The first peak at  $1.62\text{\AA}$  corresponding to the Si-O bond length decreased indicating a decrease in Si coordination of O as a result of the creation of non-bridging oxygens. In addition, a new peak appeared at about  $2.4\text{\AA}$  corresponding to the Na bond length to the non-bridging oxygens. Both of these observations would give a smaller value for the integral in Equation (5.5) for the glasses containing alkali oxide. This again is consistent with our results.

Let's summarize the above discussion. In pure fused quartz the nearest neighbors are the Si-O pairs with a bond length of  $1.62\text{\AA}$ . Each Si ion has four O nearest neighbors and each O has two Si nearest neighbors. For each alkali oxide molecule  $\text{M}_2\text{O}$  added to the system two non-bridging oxygens are created. The oxygen coordination of Si does not change but the non-bridging oxygens now have only one Si nearest neighbor and two alkali ion next nearest neighbors at an increased bond length of about  $2.4\text{\AA}$ . The decreased Si coordination of oxygen and the corresponding new peak in  $g(r)$  at larger  $r$  would account



(a)



(b)

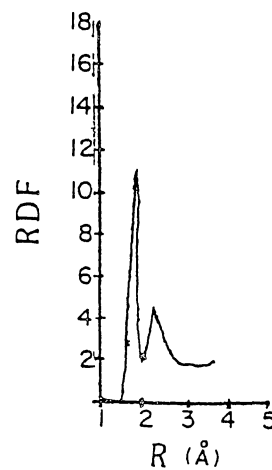


Figure 16. The Radial Distribution Function and Two-Dimensional Schematic of the Structures of (a) SiO<sub>2</sub> Glass and (b) M<sub>2</sub>O-SiO<sub>2</sub> Glass.

for the decrease in the integral in Equation (5.5) when alkali oxide is added to pure fused quartz.

Changing the type of alkali oxide from Li to Cs increases the M-O bond length due to the decrease in field strength of the alkali ion. This would account for the decrease in the integral in going from Li to Cs.

Brawer (1975) developed a theoretical model for the vibrational spectra of glasses and applied it to the experimental Raman spectra of binary alkali silicate glasses (Brawer (1975) and Brawer & White (1975)). They reported that the decrease in width of the  $1100\text{cm}^{-1}$  Raman line from Li to K was evidence of increased short-range order in the glass. The different types of disorder were defined as: fluctuating Si-O-Si angles, distorted tetrahedral angles and Si-O distances, and random relative orientations of tetrahedra. Except for the Si-O distance fluctuations, these kinds of fluctuations would not affect the radial distribution function for small  $r$  significantly. Thus our data does not conflict with their results.

Behrens et al. (1989) concluded from their four-wave mixing experiments on exactly the same glasses used in this study, that for the larger modifying ions the glasses showed an increase in local order. Again this does not contradict our results since an increase in order in going from Li to Cs is not inconsistent with an increase in M-O bond length with the non-bridging oxygens. It is this

increase in M-O bond length that we believe is primarily responsible for the decrease in the integral of Equation (5.5). in the series Li to Cs.

Within the framework of the Carleton theory, two conclusions can be made from our data at this point. The first is that  $r$  decreases as the mass of the modifying ion is increased. Referring to Equations (5.1), (5.2), and (5.3), the term outside the brackets of each equation, depending only on the index of refraction, shows no real tendency of increase or decrease with increasing size of the modifying ion (see Table XV). The same is true for the first term inside the brackets in Equations (5.1) and (5.2). However  $P_{12}$  increases by approximately 24% and  $P_{44}$  increases by 34%. We can conclude from this that the last term in each of the equations involving  $r$  must decrease to cause the photo-elastic constants to increase. Furthermore, it is this decrease of  $r$  as a result of the increase in the M-O bond length that is the main reason for the increase of  $P_{12}$  and  $P_{44}$  as the mass of the modifying ion is changed through the series Li to Cs.

The second conclusion is that  $P_{44}$  must be negative. If  $P_{44}$  were positive, then our measured values would show that  $P_{44}$  decreases rather than increases in value as the mass of the modifying ion increases. In this case it would be necessary for  $r$  to increase instead of decrease as it has to do in order to satisfy the equation for  $P_{12}$ .

Furthermore, as we have seen, an increase in  $r$  in the series Li to Cs would be inconsistent with known structural changes that take place as the size of the modifying ion is increased.

#### The Landau-Placzek Ratio

The Landau-Placzek ratio is defined as the ratio of the Rayleigh intensity to the total Brillouin intensity,

$$R_{LP} = \frac{I_R}{2I_B} \quad (5.6)$$

In the case of a single-component glass  $I_R$  is due mainly to frozen-in density fluctuations (Schroeder (1977)). In binary and more complicated glasses,  $I_R$  is attributed to frozen-in concentration fluctuations as well as density fluctuations. In pure  $\text{SiO}_2$ , where only density fluctuations are important,  $R_{LP}$  is equal to 21.6. In our glasses  $R_{LP}$  decreases from Li to Cs with a value of over 23,000 for the Li sample to 39 for the Cs sample. The high values of  $R_{LP}$  for the K, Na, and Li samples may indicate large frozen-in concentration fluctuations in these glasses.

#### The Density Derivative of the Optical Dielectric Constant

A quantity that appears in theories on light scattering in gasses, liquids and solids is the density derivative of the optical dielectric constant (Fabelinskii (1968)). An expression for this quantity can be derived



in terms of experimentally measured quantities by using Equation (3.12) and applying it to the case of a material under hydrostatic pressure. For cubic crystals and isotropic glasses the result is,

$$\left(\rho \frac{\partial \epsilon}{\partial \rho}\right)_{\text{obs.}} = \frac{n^4}{3}(3P_{12} + 2P_{44}) \quad (5.7)$$

where  $n$  is the index of refraction and  $P_{12}$  and  $P_{44}$  are the photo-elastic constants measured in Brillouin scattering experiments. The subscript obs. refers to the fact that this is the observed value from light scattering.

Other expressions for the density derivative exist based on different models. For example,

$$\left(\rho \frac{\partial \epsilon}{\partial \rho}\right)_{\text{L.L.}} = \frac{1}{3}(n^2-1)(n^2+2) \quad (5.8)$$

can be derived from implicit differentiation of the standard Loentz-Lorentz equation,

$$\frac{n^2-1}{n^2+2} = \frac{4\pi\alpha\rho N_A}{3M} \quad (5.9)$$

where  $\alpha$  is the average polarizability (assumed to be independent of density in this model),  $\rho$  is the density,  $N_A$  is Avogadro's number, and  $M$  is the molecular weight.

By treating the term  $n^2+2$  in Equation (5.9) as a constant when differentiating, the so called Drude equation results,

$$\left(\rho \frac{\partial \epsilon}{\partial \rho}\right)_{\text{Dr.}} = (n^2-1) . \quad (5.10)$$

The justification for setting  $n^2+2$  equal to a constant was given by Rocard (1928). He showed that the term

$n^2+2$  in Equation (5.8) is the result of the action of the molecules outside the Lorentz cavity. Furthermore, he showed that the fluctuation in the index of refraction for the material outside the cavity has little effect on the change in the field inside the cavity. As a result, the  $n^2$  in the term  $n^2+2$  can be treated as a constant when differentiating Equation (5.9) (Fabelinskii (1968)).

Table XVI shows the calculated values for the density derivative of the dielectric constant of the five glasses studied in this report in addition to fused quartz for comparison. As can be seen, neither form of the density derivative agrees with the measured values. The measured value of the density derivative of the optical dielectric constant shows an increase of 41% as the mass of the modifying ion is increased. At the same time it is lower by as much as 57% compared to that predicted by the corresponding Lorentz-Lorenz value and 34% lower than that predicted by the Drude model. Interestingly, the measured values approach those predicted by the Drude model for the heavier modifying ions.

The fact that the observed values do not agree with either form is not surprising in view of the fact that both equations were derived under the assumption that nearest neighbor atoms of the material are arranged in a completely random fashion. In silicate glasses this may not be the case. The fact that the observed density derivative approaches the Drude values for the heavier

TABLE XVI  
 VALUES FOR THE DENSITY DERIVATIVE  
 OF THE DIELECTRIC CONSTANT

Sample	$\left(\rho \frac{\partial \epsilon}{\partial \rho}\right)_{\text{obs.}}$	$\left(\rho \frac{\partial \epsilon}{\partial \rho}\right)_{\text{L.L.}}$	$\left(\rho \frac{\partial \epsilon}{\partial \rho}\right)_{\text{Dr.}}$
$\text{Li}_2\text{O}-\text{SiO}_2$	1.04	2.40	1.57
$\text{Na}_2\text{O}-\text{SiO}_2$	1.22	2.26	1.51
$\text{K}_2\text{O}-\text{SiO}_2$	1.13	2.27	1.51
$\text{Rb}_2\text{O}-\text{SiO}_2$	1.32	2.20	1.47
$\text{Cs}_2\text{O}-\text{SiO}_2$	1.46	2.31	1.53
$\text{SiO}_2$	1.03	1.57	1.14

modifying ions may indicate that as the mass of the modifying ion increases, the nearest neighbors are becoming less correlated. This is consistent with the observed decrease in  $r$ .

As was mentioned earlier, the polarizability probably should be taken as density dependent. Both the Lorentz-Lorentz and the Drude expressions for the density derivative of the dielectric constant were obtained assuming that the polarizability is independent of density. If we implicitly differentiate Equation (5.9) as was done to obtain Equation (5.8), but this time treating the polarizability as a function of density we obtain,

$$\left(\rho \frac{\partial \epsilon}{\partial \rho}\right) = \frac{1}{3}(n^2-1)(n^2+2)(1-\lambda_0) \quad (5.11)$$

where,

$$\lambda_0 = -\frac{\rho}{\alpha} \left(\frac{\partial \alpha}{\partial \rho}\right) \quad (5.12)$$

is called the strain polarizability constant. By comparing the observed and calculated values (Lorentz-Lorentz and Drude) of the density derivative we get,

$$\left(\rho \frac{\partial \epsilon}{\partial \rho}\right)_{\text{obs.}} = (1-\lambda_0) \left(\rho \frac{\partial \epsilon}{\partial \rho}\right)_{\text{L.L.}} \quad (5.13)$$

$$\left(\rho \frac{\partial \epsilon}{\partial \rho}\right)_{\text{obs.}} = (1-\lambda_0) \left(\rho \frac{\partial \epsilon}{\partial \rho}\right)_{\text{Dr.}} \quad (5.14)$$

The values for the strain polarizability constant determined from Equations (5.13) and (5.14) are shown in

Table XVII for the five glasses of this study in addition to fused quartz for comparison. Also shown are the values for the derivative of the polarization with respect to density. As can be seen the density derivative of the polarization decreases with increasing mass of the modifying ion. This may be understood by considering the following points. The change in the index of refraction with density in solids is caused by two competing effects (Babcock (1977)): (1) an increase in the number of scattering centers per unit volume will result in an increase in the refractive index with increasing density, and (2) the contraction of the electronic clouds of the atoms will reduce the polarizability and decrease the refractive index. This second effect should be largest for ions with small ionic radii and large charge (Schroeder (1980)). That is, the change in polarizability with density caused by an external stress should be the largest for the Li glass with small ionic radius ( $0.433\text{\AA}$ ) and smallest for the Cs glass with a large ionic radius ( $1.65\text{\AA}$ ). This is consistent with our observations.

In passing we point out that for most materials the first effect, discussed above, dominates over the second so that the density derivative of the dielectric constant is positive as it is for our glasses. But for diamond, ZnS, and MgO, the second effect is larger than the first and the density derivative is negative for these crystals (Babcock (1977)).

TABLE XVII  
STRAIN POLARIZABILITY CONSTANTS

Sample	$(\lambda_0)_{L.L.}$	$(\lambda_0)_{Dr.}$	$(\frac{\partial \alpha}{\partial \rho})_{L.L.}$	$(\frac{\partial \alpha}{\partial \rho})_{Dr.}$
$Li_2O-SiO_2$	0.57	0.36	0.34	0.22
$Na_2O-SiO_2$	0.46	0.28	0.19	0.11
$K_2O-SiO_2$	0.50	0.37	0.25	0.18
$Rb_2O-SiO_2$	0.40	0.26	0.11	0.069
$Cs_2O-SiO_2$	0.37	0.25	0.04	0.030
$SiO_2$	0.34	0.23	0.09	0.062

## Summary

In this dissertation we report the measurements of the elastic and photo-elastic constants of five silicate based glasses using Brillouin spectroscopy. Both elastic constants  $C_{11}$  and  $C_{44}$  were found to decrease as the size and mass of the modifying ion was increased. The decrease in elastic constants is an indication that the glasses are becoming softer and more elastic for the heavier modifying ions.

The photo-elastic constants were measured by comparing the scattered intensity of the glasses to that of the standard scatterer fused quartz. Both  $P_{12}$  and  $P_{44}$  showed a general increase as the size and mass of the modifying ion was increased. Within the framework of Carleton's equations for the photo-elastic constants, the increase in  $P_{12}$  and  $P_{44}$  may be due in part to the increased distance in the M-O bond length for the heavier modifying ions.

The photo-elastic data along with measurements of the index-of-refraction and density were used to test Carleton's theory of photo-elasticity in glasses for consistency with expected results. It was found that the observed photo-elastic constants could be described qualitatively by Carleton's theoretical expressions.

The observed density derivative of the optical dielectric constant is lower than that predicted by the

Lorentz-Lorenz and the Drude expressions. However as the size and mass of the modifying ion is increased in the base glass the observed values approach those of the Drude values.

The strain polarizability constant decreases as the size and mass of the modifying ion is increased. This decrease may indicate a decrease in the change in polarizability caused by strain.



## REFERENCES

- Babcock, C. L. (1977). Silicate Glass Technology Methods  
John Wiley & Sons, New York, NY.
- Behrens, E. G., Powell, R. C., & Blackburn, D. H. (1989).  
Unpublished.
- Behrens, E. G., Durville, F. M., Powell R. C., &  
Blackburn, D. H. (1989). Phys. Rev. B, 39, 6076.
- Born, M., & Huang, K. (1962). In Dynamical Theory of  
Crystal Lattices, For the Cauchy relation see  
pp. , Oxford University Press, London.
- Bouchalkha, A. (1989). Masters Thesis, Temperature  
Dependence of the LA[110] Brillouin Shift in the  
Structural Glass:  $\text{Rb}_{1-x}(\text{NH}_4)_x\text{H}_2\text{PO}_4$  .
- Brawer, S. (1975). Phys. Rev. B, 11, 3173.
- Brawer, S. A. & White W. B. (1975). J. Chem. Phys., 63, 2421
- Canberra (1988). In Series 35 Plus Multichannel Analyzer  
Operator's Manual, Version 2, Appendix D (pp. 162-166)  
Canberra Industries, Inc., One State Street, Meriden,  
CT 06450.
- Carleton, H. R. (1972). In Douglas, R. W., & Ellis, B.  
(Eds.), Amorphous Materials, (p 103) Wiley,  
Interscience, New York.
- Chandler, D. (1987). Introduction To Modern Statistical  
Mechanics, (p 197) Oxford University Press,  
New York, NY.
- Christman J. R. (1988). In Fundamentals of Solid State  
Physics, (p. 174-175) John Wiley & Sons, Inc., New  
York.
- Cummins, H. Z. & Schoen, P. E. (1972). Linear Scattering  
from Thermal Fluctuations. In Arecchi and Schultz-DuBois  
(Eds.), Laser Handbook, Vol. 2. (pp. 1029-1075)  
North-Holland Publ. Co., Amsterdam.

- Dixon, G. S. (1989). Private Communication.
- Durville, F.M., Behrens, E.G., & Powell, R.C. (1987). Phys. Rev. B, 35,4109.
- Fabelinskii, I. L. (1968). Molecular Scattering of Light Plenum Press, New York.
- Fixman, M. (1955). J. Chem. Phys., 23, 2074
- Gang, X., & Powell, R. C. (1985). J. Appl. Phys., 57, 1299.
- Hecht, E. & Zajac, A. (1975). In Optics, (p. 310-311), Addison-Wesley Publishing Company, Reading, MA.
- Kittel, C. (1986). Introduction to Solid State Physics Sixth Edition, John Wiley & Sons, Inc., New York, NY.
- Kreidl, N. J. (1983). In Uhlmann and Kreidl (Eds.), Glass: Science and Technology, Vol. 1. (pp. 105-299), Academic Press, New York, NY.
- Loudon, R. (1965). J. Physique, 28, 677.
- Marquardt, D.W. (1963). J. Soc. Indust. Appl. Math, 11,431
- Mueller, H. (1935). Physics, 6, 179.
- Mueller, H. (1935). Phys. Rev., 47, 947.
- Mueller, H. (1938). J. Am. Ceram. Soc., 21, 27.
- Murray, R. A., Song, L. W., & Ching, W. Y. (1987). J. Non-Cryst. Solids, 94, 133.
- Nye, J. F. (1981). In Physical Properties of Crystals, Clarendon Press, Oxford.
- Pan, Z. (1989). Private Communication.
- Pinnow, D. A. (1972). Linear Scattering From Thermal Fluctuations. In Arecchi and Schultz-DuBois (Eds.), Laser Handbook, Vol. 1. (pp. 995-1008), North-Holland Publ. Co., Amsterdam.
- Plotit (1989). Scientific Programming Enterprises, P.O. Box 669 Haslett, MI 48840.
- Powell, R. C. (1989) Private Communication.
- Rocard, Y. (1928). Ann. Phys. 10, 158.

- Schroeder, J. (1977). Light Scattering of Glass. In Tomozawa and Doremus (Eds.), Treatise on Materials Science and Technology, Vol. 12. (pp. 157-222) Academic Press, New York.
- Schroeder, J. (1980), *J. Non-Cryst. Solids*, 40, 549.
- Schroeder, J. (1985). *Opt Eng.*, 24, 697.
- Sigel, G.H. (1977). Optical Absorption of Glass. In Tomozawa and Doremus (Ed.), Treatise on Materials Science and Technology, Vol. 12 (pp. 5-89) Academic Press, New York.
- Sincerbox, G. T. & Roosen, G. (1983). *Appl. Opt.*, 22, 690
- Sipe, J. E. (1978). *Canad. J. Phys.*, 56, 199.
- Smart Integrated Software (1989). Innovative Software, Inc.
- Soules, T. F. (1979). *J. Chem. Phys.*, 77, 4570.
- Tanaka, K. & Odajima, A. (1981). *Appl. Phys. Lett.*, 38, 481.
- Tesar, A. A., & Varshneya, A. K. (1987). *J. Chem. Phys.*, 87, 2986.
- Vogel, W. (1985). In Chemistry of Glass, American Ceramic Society, Inc., Columbus, Ohio.

## APPENDIX A

### THE COMPUTER ANALYSIS PROGRAM

In this appendix we present some of the details of how the computer program used to analyze the Brillouin data works. The program is listed at the end of this appendix. Some of the algorithms used in the program were taken from the Canberra multichannel analyzer manual (Canberra (1987)).

#### Background

The background is calculated from the background region-of-interest (ROI) supplied by the user. For the experiments reported in this dissertation, the background ROI was taken from the lowest part of the spectrum and was usually about 10 to 20 channels wide. The background was calculated by summing the total number of counts in the ROI and then dividing by the number of channels in the ROI. This is done in lines 620 to 670 of the program. The equation for the background  $B$  is given by,

$$B = \sum_{i=B_1}^{B_2} \frac{Y(i)}{(B_2 - B_1 + 1)} \quad (\text{A.1})$$

where  $B_1$  and  $B_2$  are the first and last channel respectively of the background ROI and  $Y(i)$  is the number

of counts in the  $i^{\text{th}}$  channel. The "one" in the denominator of Equation (A.1) is needed so that the last channel in the (ROI) will be counted.

#### Peak Channel

The ROI for the Rayleigh, LA, and TA peaks of the spectrum are supplied by the user. To find the channel with the most number of counts  $Y_{\text{max}}$  in each ROI, the program simply scans through the ROI picking out the channel with the most counts. This is done in line 920. The peak channel,  $X_{\text{max}}$ , is the channel with the maximum number of counts in the ROI and may not be equal to the actual centroid of the peak. This would be the case if a peak was asymmetric. The centroid is calculated later in the program and will be discussed in turn.

#### Peak Area

The area is calculated in the same region of the program where the peak channel is calculated, lines 890 to 940. The area of a peak is equal to the sum of the total number of counts in each channel of the peak ROI minus the background,

$$\begin{aligned}
 A &= \sum_{i=S_n}^{E_n} [Y(i) - B] \\
 &= \left[ \sum_{i=S_n}^{E_n} Y(i) \right] - (E_n - S_n + 1)B
 \end{aligned}
 \tag{A.2}$$

where  $S_n$  is the start channel of the  $n^{\text{th}}$  ROI and  $E_n$  is the end channel.

### Full-Width at Half-Maximum

The full-width at half-maximum is the peaks width at half of its maximum amplitude. The peak channel,  $X_{\max}$ , is used to find one-half of the peak amplitude (half-maximum value)  $Y_{HM}$

$$\begin{aligned} Y_{HM} &= \frac{[Y(X_{\max}) - B]}{2} + B \\ &= \frac{[Y_{\max} + B]}{2} \end{aligned} \quad (A.3)$$

where  $Y(X_{\max})$  is the number of counts in the peak channel. This is done in line 980. In lines 990 to 1040, the program first scans down the right-hand side of the peak and finds the first channel  $X_{RHM}$  that has fewer counts than the half-maximum value  $Y_{HM}$ . The right full-width at half-maximum channel is then determined from the interpolated value between  $X_{RHM}$  and the channel just before it,

$$X_{RFWHM} = X_{RHM} - \frac{[Y_{HM} - Y(X_{RHM})]}{[Y(X_{RHM}-1) - Y(X_{RHM})]} \quad (A.4)$$

The same procedure is used to find the left full-width at half-maximum  $X_{LFWHM}$ . The full-width at half-maximum is then given by  $FWHM = X_{RFWHM} - X_{LFWHM}$ . The above algorithms are found in lines 1050 to 1070.

### The Centroid

The centroid is the channel that corresponds to the geometric "center of mass" of the peak. To find the

centroid  $X_c$  within a ROI, the program sums the products of the channel number relative to the left half-maximum channel and the number of counts in that channel. The above result is then divided by the area  $A$  of that ROI found earlier, and then added to  $X_{LHM}$

$$X_c = \frac{\sum_{i=S_n}^{E_n} [i - X_{LHM}] Y(i)}{A} + X_{LHM} \quad (A.5)$$

This routine is found in lines 1080 to 1120.

#### The Average Areas

As was mentioned in Chapter II, the Brillouin spectra taken for this study consisted of three orders. The average Rayleigh area was determined from the three Rayleigh peaks in the spectrum. The average LA and TA areas were determined from the five right most LA and TA peaks respectively. The first LA and TA peaks were not used due to small distortions in the spectrum that appeared occasionally under approximately the first 10% of the ramp.

#### The Free Spectral Range and the Finesse

The channel free spectral range (FSR) is the number of channels between the centroids of adjoining Rayleigh peaks. The free spectral range is calculated in line 1750. The finesse is a measure of the resolving power of the interferometer and is equal to the full-width at half-maximum divided by the channel free spectral range,

$$F = \frac{\text{FWHM}}{\text{FSR}} \quad (\text{A.6})$$

The program calculates separately the average finesse for the Rayleigh, LA, and TA peaks. That is, the value used for FWHM in Equation (A.6) in the Rayleigh peak finesse is the average value taken over the three Rayleigh peaks in the spectrum. For the LA and TA finesses the five right most peaks in the spectrum are used in the average. The FSR and the finesse are calculated in lines 1750 to 1810.

#### The Brillouin Shift and Plate Separation

The Brillouin shifts were determined using Equation (2.5) as described in detail in Chapter II and using the calculated centroids for each peak. The plate separation, used in the calculation, is supplied by the user and had been determined previously either using fused quartz as a standard or by using a traveling microscope. The Brillouin shifts are calculated in lines 1850 to 1860.

If the user chose to have the Fabry-Perot plate separation calculated by the program, the program does this in line 1870. The plate separation is determined using a fused quartz spectrum and using Equation (2.5). The value used for the LA Brillouin shift of fused quartz is  $0.801\text{cm}^{-1}$  the average value as determined from six separate spectra where the plate separation was measured using a traveling microscope.

The following is a listing of the program.



```

10 REM *****
20 REM *
30 REM *           Program for the Analysis of Brillouin           *
40 REM *           Scattering Data                               *
50 REM *
60 REM *****
70 REM
80 REM
90 REM ***** Input Routine *****
100 REM
110 SCREEN 0,1:WIDTH 80:COLOR 14,1:CLS
120 LOCATE 1,24:PRINT"Brillouin Data Analysis Program"
130 LOCATE 3,2:INPUT"Input File Name = ",FILE$
140 OPEN "1",#1,FILE$
150 LOCATE 4,2:INPUT"Memory Partition x/4, x = ",MP
160 LOCATE 3,40:INPUT"Input background start channel = ",B1%
170 LOCATE 4,40:INPUT"Input background end channel = ",B2%
180 LOCATE 5,2:INPUT"Calculate plate separation Y or N ? ",M$
190 REM
200 REM ***** Brillouin Shift for *****
210 REM ***** Fused Quartz *****
220 REM
230 IF M$="y" OR M$="Y" THEN DKQLA=.801:GOTO 250
240 LOCATE 5,40:INPUT"Input plate separation (cm) = ",D
250 LOCATE 7,2:PRINT"Input the ROI for 13 peaks in the spectrum"
260 LOCATE 9,2:INPUT" 1) Start = ",S1%:LOCATE 9,20:INPUT"End = ",E1%
270 LOCATE 10,2:INPUT" 2) Start = ",S2%:LOCATE 10,20:INPUT"End = ",E2%
280 LOCATE 11,2:INPUT" 3) Start = ",S3%:LOCATE 11,20:INPUT"End = ",E3%
290 LOCATE 12,2:INPUT" 4) Start = ",S4%:LOCATE 12,20:INPUT"End = ",E4%
300 LOCATE 13,2:INPUT" 5) Start = ",S5%:LOCATE 13,20:INPUT"End = ",E5%
310 LOCATE 14,2:INPUT" 6) Start = ",S6%:LOCATE 14,20:INPUT"End = ",E6%
320 LOCATE 15,2:INPUT" 7) Start = ",S7%:LOCATE 15,20:INPUT"End = ",E7%
330 LOCATE 16,2:INPUT" 8) Start = ",S8%:LOCATE 16,20:INPUT"End = ",E8%
340 LOCATE 17,2:INPUT" 9) Start = ",S9%:LOCATE 17,20:INPUT"End = ",E9%
350 LOCATE 18,2:INPUT"10) Start = ",S10%:LOCATE 18,20:INPUT"End = ",E10%
360 LOCATE 19,2:INPUT"11) Start = ",S11%:LOCATE 19,20:INPUT"End = ",E11%
370 LOCATE 20,2:INPUT"12) Start = ",S12%:LOCATE 20,20:INPUT"End = ",E12%
380 LOCATE 21,2:INPUT"13) Start = ",S13%:LOCATE 21,20:INPUT"End = ",E13%
390 REM
400 REM ***** Initialize Variables *****
410 REM
420 COUNTER1%=0
430 IF MP=1 THEN N2%=1023
440 IF MP=2 THEN N2%=2047
450 IF MP=3 THEN N2%=3071
460 IF MP=4 THEN N2%=4095
470 REM
480 REM ***** Dimension Arrays *****
490 REM
500 DIM X1%(4097),Y1(4097)
510 REM
520 REM ***** Input Data From Disk *****
530 REM

```

```

540 INPUT #1,X1%,Y1
550 FOR I%=0 TO N2%
560 INPUT #1,X1%(I%),Y1(I%)
570 NEXT
580 CLOSE #1
590 REM
600 REM ***** Calculate the Background *****
610 REM
620 B3%=B2%-B1%
630 B=0
640 FOR J%=B1% TO B2%
650 B=Y1(J%)+B
660 NEXT
670 B=B/(B3%+1)
680 REM
690 REM ***** Determine Which Peak to Consider *****
700 REM
710 COUNTER1%=COUNTER1%+1
720 ON COUNTER1% GOTO 730,740,750,760,770,780,790,800,810,820,830,840,850,1310
730 S%=S1%;E%=E1%;GOTO 890
740 S%=S2%;E%=E2%;GOTO 890
750 S%=S3%;E%=E3%;GOTO 890
760 S%=S4%;E%=E4%;GOTO 890
770 S%=S5%;E%=E5%;GOTO 890
780 S%=S6%;E%=E6%;GOTO 890
790 S%=S7%;E%=E7%;GOTO 890
800 S%=S8%;E%=E8%;GOTO 890
810 S%=S9%;E%=E9%;GOTO 890
820 S%=S10%;E%=E10%;GOTO 890
830 S%=S11%;E%=E11%;GOTO 890
840 S%=S12%;E%=E12%;GOTO 890
850 S%=S13%;E%=E13%;GOTO 890
860 REM
870 REM ***** Determine the Peak Channel and the Area *****
880 REM
890 Y=0;YMAX=Y1(S%)
900 FOR K%=S% TO E%
910 Y=Y1(K%)+Y
920 IF Y1(K%)>YMAX THEN YMAX=Y1(K%);XMAX%=K%
930 NEXT
940 AREA=Y-(E%-S%+1)*B
950 REM
960 REM ***** Calculate the FWHM and Centroid *****
970 REM
980 HALFMAX=(Y1(XMAX%)+B)/2
990 FOR I%=1 TO 100
1000 IF Y1(XMAX%+I%)<HALFMAX THEN HM2%=XMAX%+I%;GOTO 1020
1010 NEXT
1020 FOR J%=1 TO 100
1030 IF Y1(XMAX%-J%)<HALFMAX THEN HM1%=XMAX%-J%;GOTO 1050
1040 NEXT
1050 FWHM2=HM2%-(HALFMAX-Y1(HM2%))/(Y1(HM2%-1)-Y1(HM2%))
1060 FWHM1=HM1%+(HALFMAX-Y1(HM1%))/(Y1(HM1%+1)-Y1(HM1%))

```

```

1070 FWHM=FWHM2-FWHM1
1080 XC1=0
1090 FOR K%=S% TO E%
1100 XC1=XC1+(K%-HM1%+1)*Y1(K%)
1110 NEXT
1120 XC=XC1/AREA+HM1%
1130 ON COUNTER1% GOTO 1170,1180,1190,1200,1210,1220,1230,1240,1250,1260,1270,12
80,1290
1140 REM
1150 REM ***** Assign the Area, FWHM and Centroid to the Right Peak *****
1160 REM
1170 AREA1=AREA: XMAX1%=XMAX%:FWHM01=FWHM:XC01=XC:GOTO 1300
1180 AREA2=AREA: XMAX2%=XMAX%:FWHM02=FWHM:XC2=XC:GOTO 1300
1190 AREA3=AREA: XMAX3%=XMAX%:FWHM3=FWHM:XC3=XC:GOTO 1300
1200 AREA4=AREA: XMAX4%=XMAX%:FWHM4=FWHM:XC4=XC:GOTO 1300
1210 AREA5=AREA: XMAX5%=XMAX%:FWHM5=FWHM:XC5=XC:GOTO 1300
1220 AREA6=AREA: XMAX6%=XMAX%:FWHM6=FWHM:XC6=XC:GOTO 1300
1230 AREA7=AREA: XMAX7%=XMAX%:FWHM7=FWHM:XC7=XC:GOTO 1300
1240 AREA8=AREA: XMAX8%=XMAX%:FWHM8=FWHM:XC8=XC:GOTO 1300
1250 AREA9=AREA: XMAX9%=XMAX%:FWHM9=FWHM:XC9=XC:GOTO 1300
1260 AREA10=AREA: XMAX10%=XMAX%:FWHM10=FWHM:XC10=XC:GOTO 1300
1270 AREA11=AREA: XMAX11%=XMAX%:FWHM11=FWHM:XC11=XC:GOTO 1300
1280 AREA12=AREA: XMAX12%=XMAX%:FWHM12=FWHM:XC12=XC:GOTO 1300
1290 AREA13=AREA: XMAX13%=XMAX%:FWHM13=FWHM:XC13=XC:GOTO 1300
1300 GOTO 710
1310 REM
1320 REM ***** Calculate the Average Areas *****
1330 REM
1340 AREARAY=(AREA1+AREA6+AREA11)/3
1350 AREALA=(AREA3+AREA4+AREA8+AREA9+AREA13)/5
1360 AREATA=(AREA2+AREA5+AREA7+AREA10+AREA12)/5
1370 CLS
1380 REM
1390 REM ***** Print-out of Results *****
1400 REM
1410 LOCATE 1,19:PRINT"Analysis of";MP:LOCATE 1,32:PRINT "/4 Memory of File ";FI
LE$
1420 LOCATE 3,1:PRINT"Background:":LOCATE 3,12:PRINT USING "#####.##";B:LOCATE 3
,24:PRINT"Counts per dwell time"
1430 LOCATE 5,1:PRINT"Areas:"
1440 LOCATE 5,14:PRINT"Rayleigh ":LOCATE 5,25:PRINT USING "#####";AREA1,ARE
A6,AREA11
1450 LOCATE 6,14:PRINT"LA      ":LOCATE 6,25:PRINT USING "#####";AREA3,ARE
A4,AREA8,AREA9,AREA13
1460 LOCATE 7,14:PRINT"TA      ":LOCATE 7,25:PRINT USING "#####";AREA2,ARE
A5,AREA7,AREA10,AREA12
1470 LOCATE 9,1:PRINT"Averages:"
1480 LOCATE 9,14:PRINT"Rayleigh ":LOCATE 9,25:PRINT USING "#####";AREARAY
1490 LOCATE 10,14:PRINT"LA      ":LOCATE 10,25:PRINT USING "#####";AREALA
1500 LOCATE 11,14:PRINT"TA      ":LOCATE 11,25:PRINT USING "#####";AREATA
1510 LOCATE 13,1:PRINT"Peak "
1520 LOCATE 14,1:PRINT"Channels:":LOCATE 13,14:PRINT"Rayleigh ":LOCATE 13,25:PRI
NT USING "#####";XMAX1%,XMAX6%,XMAX11%

```

```

1530 LOCATE 14,14:PRINT"LA      ":LOCATE 14,25:PRINT USING "#####";XMAX3%,
XMAX4%,XMAX8%,XMAX9%,XMAX13%
1540 LOCATE 15,14:PRINT"TA      ":LOCATE 15,25:PRINT USING "#####";XMAX2%,
XMAX5%,XMAX7%,XMAX10%,XMAX12%
1550 LOCATE 17,1:PRINT"Peak"
1560 LOCATE 17,14:PRINT"Rayleigh ":LOCATE 17,25:PRINT USING "#####";Y1(XMAX
1%),Y1(XMAX6%),Y1(XMAX11%)
1570 LOCATE 18,1:PRINT"Intensities:"
1580 LOCATE 18,14:PRINT"LA      ":LOCATE 18,25:PRINT USING "#####";Y1(XMAX
3%),Y1(XMAX4%),Y1(XMAX8%),Y1(XMAX9%),Y1(XMAX13%)
1590 LOCATE 19,14:PRINT"TA      ":LOCATE 19,25:PRINT USING "#####";Y1(XMAX
2%),Y1(XMAX5%),Y1(XMAX7%),Y1(XMAX10%),Y1(XMAX12%)
1600 LOCATE 23,24:PRINT"Press the Space Bar to Continue"
1610 A$=INKEY$:IF A$=CHR$(32) GOTO 1620 ELSE 1610
1620 CLS
1630 LOCATE 1,19:PRINT"Analysis of";MP:LOCATE 1,32:PRINT "/4 Memory of File ";FI
LE$
1640 LOCATE 3,1:PRINT"FWMH's:"
1650 LOCATE 3,14:PRINT"Rayleigh ":LOCATE 3,25:PRINT USING "#####.#";FWMH01,FW
MH6,FWMH11
1660 LOCATE 4,14:PRINT"LA      ":LOCATE 4,25:PRINT USING "#####.#";FWMH3,FWH
M4,FWMH8,FWMH9,FWMH13
1670 LOCATE 5,14:PRINT"TA      ":LOCATE 5,25:PRINT USING "#####.#";FWMH02,FW
HM5,FWMH7,FWMH10,FWMH12
1680 LOCATE 7,1:PRINT"Centroids:"
1690 LOCATE 7,14:PRINT"Rayleigh ":LOCATE 7,25:PRINT USING "#####.#";XC01,XC6,
XC11
1700 LOCATE 8,14:PRINT"LA      ":LOCATE 8,25:PRINT USING "#####.#";XC3,XC4,X
C8,XC9,XC13
1710 LOCATE 9,14:PRINT"TA      ":LOCATE 9,25:PRINT USING "#####.#";XC2,XC5,X
C7,XC10,XC12
1720 REM
1730 REM ***** Calculate the Free Spectral Range and the Finesse *****
1740 REM
1750 FSR=(XC11-XC01)/2
1760 FWHMRY=(FWMH01+FWMH6+FWMH11)/3
1770 FWHMLA=(FWMH3+FWMH4+FWMH8+FWMH9+FWMH13)/5
1780 FWHMTA=(FWMH02+FWMH5+FWMH7+FWMH10+FWMH12)/5
1790 FINRAY=FSR/FWHMRY
1800 FINLA=FSR/FWHMLA
1810 FINTA=FSR/FWHMTA
1820 REM
1830 REM ***** Calculate the Brillouin Shifts *****
1840 REM
1850 DKLA=((XC13-XC9+XC8-XC4)/2)/(XC13-XC8+XC9-XC4)
1860 DKTA=((XC12-XC10+XC7-XC5)/2)/(XC12-XC7+XC10-XC5)
1870 IF M$="Y" OR M$="y" THEN D=DKLA/(2*DKBLA):GOTO 1930
1880 DK2LA=DKLA/(2*D)
1890 DK2TA=DKTA/(2*D)
1900 REM
1910 REM ***** Print-out the Results *****
1920 REM
1930 LOCATE 11,1:PRINT"FSR:"

```

```

1940 LOCATE 11,14:PRINT"Rayleigh":LOCATE 11,25:PRINT USING "#####.#";XC6-XC01
,XC11-XC6
1950 LOCATE 13,1:PRINT"Finesse:"
1960 LOCATE 13,14:PRINT"Rayleigh ":LOCATE 13,25:PRINT USING "#####";FINRAY
1970 LOCATE 14,14:PRINT"LA      ":LOCATE 14,25:PRINT USING "#####";FINLA
1980 LOCATE 15,14:PRINT"TA      ":LOCATE 15,25:PRINT USING "#####";FINTA
1990 LOCATE 17,1:PRINT"(1/L):"
2000 LOCATE 17,14:PRINT"LA ":LOCATE 17,25:PRINT USING "###.###";DKLA
2010 LOCATE 18,14:PRINT"TA ":LOCATE 18,25:PRINT USING "###.###";DKTA
2020 LOCATE 23,24:PRINT"Press the Space Bar to Continue"
2030 A%=INKEY$:IF A%=CHR$(32) THEN 2040 ELSE 2030
2040 CLS
2050 LOCATE 1,19:PRINT"Analysis of";MP:LOCATE 1,32:PRINT"/4 Memory of File ";FIL
E$
2060 LOCATE 3,1:PRINT"Brillouin "
2070 LOCATE 3,14:PRINT"LA      ":LOCATE 3,25:PRINT USING "###.###";DK2LA
2080 LOCATE 4,1:PRINT"Shift: ":LOCATE 4,14:PRINT"TA      ":LOCATE 4,25:PRINT USI
NG "###.###";DK2TA
2090 LOCATE 6,1:PRINT"Landau-"
2100 LOCATE 7,1:PRINT"Placzek:":LOCATE 7,25:PRINT USING "#####.#";AREARAY/(2*
AREALA)
2110 LOCATE 9,1:PRINT"Plate"
2120 LOCATE 10,1:PRINT"Separation: ":LOCATE 10,25:PRINT USING "#####.###";D;:PR
INT"cm"
2130 LOCATE 23,24:PRINT"Press the Space Bar to Continue"
2140 A%=INKEY$:IF A%=CHR$(32) THEN 2180 ELSE 2140
2150 REM
2160 REM ***** Print-out Background and ROI's *****
2170 REM
2180 CLS:LOCATE 1,19:PRINT"Analysis of";MP:LOCATE 1,32:PRINT"/4 Memory of File "
;FILE$
2190 LOCATE 4,2:PRINT"Background Start Channel = ";B1%
2200 LOCATE 5,2:PRINT"Background End Channel  = ";B2%
2210 LOCATE 7,2:PRINT"ROI's for the 13 Peaks"
2220 LOCATE 9,2:PRINT"1) Start = ",S1%:LOCATE 9,25:PRINT"End =      ";E1%
2230 LOCATE 10,2:PRINT"2) Start = ",S2%:LOCATE 10,25:PRINT"End =     ";E2%
2240 LOCATE 11,2:PRINT"3) Start = ",S3%:LOCATE 11,25:PRINT"End =     ";E3%
2250 LOCATE 12,2:PRINT"4) Start = ",S4%:LOCATE 12,25:PRINT"End =     ";E4%
2260 LOCATE 13,2:PRINT"5) Start = ",S5%:LOCATE 13,25:PRINT"End =     ";E5%
2270 LOCATE 14,2:PRINT"6) Start = ",S6%:LOCATE 14,25:PRINT"End =     ";E6%
2280 LOCATE 15,2:PRINT"7) Start = ",S7%:LOCATE 15,25:PRINT"End =     ";E7%
2290 LOCATE 16,2:PRINT"8) Start = ",S8%:LOCATE 16,25:PRINT"End =     ";E8%
2300 LOCATE 17,2:PRINT"9) Start = ",S9%:LOCATE 17,25:PRINT"End =     ";E9%
2310 LOCATE 18,2:PRINT"10) Start = ",S10%:LOCATE 18,25:PRINT"End =      ";E10%
2320 LOCATE 19,2:PRINT"11) Start = ",S11%:LOCATE 19,25:PRINT"End =     ";E11%
2330 LOCATE 20,2:PRINT"12) Start = ",S12%:LOCATE 20,25:PRINT"End =     ";E12%
2340 LOCATE 21,2:PRINT"13) Start = ",S13%:LOCATE 21,25:PRINT"End =     ";E13%
2350 LOCATE 23,24:PRINT"Press the Space Bar to Continue"
2360 A%=INKEY$:IF A%=CHR$(32) THEN 2370 ELSE 2360
2370 END

```

## APPENDIX B

### APPROXIMATIONS AND CORRECTIONS TO THE INTENSITY RATIO

In the first section of this appendix, the volume ratio that appears in Equation (3.25) is evaluated. In the next section the solid angle correction to the intensity ratio  $\beta$  is derived. The correction for the back reflection of the laser beam from the inside surface of the sample is derived in the third section and in the last section the uncertainty in the sound velocity due to the finite solid angle is determined.

#### The Volume Ratio

In our experiments, the sample is located at approximately two focal lengths from the collecting lens so that if the effects of refraction are neglected, the scattering volume image would be the same size as the object. In reality, the refraction of the scattered light, as it leaves the sample, serves to reduce the size of the scattering volume from what we would expect it to be if there was no refraction. Since the scattered intensity is proportional to the scattering volume, it is necessary to know the differences in this quantity as a

result of the differences in the index of refraction of the samples.

The quantity of interest here is the ratio of the scattering volume of fused quartz to that of the glass sample. This quantity appears in Equation (3.25) of Chapter III and it was stated there that the ratio was approximately equal to one. In this first section, the apparent scattering volume is derived and then corrected for the index of refraction of the sample. The scattering volume ratio is evaluated for all of the glass samples.

Figure 17 shows a top view of a sample of refractive index  $n$ , with a laser beam of width  $w$  incident from the top of the figure. The distance from the center of the beam to the front surface of the sample is  $r$ . The distance from the center of the laser beam to the collecting lens is  $R$  and the diameter of the pinhole is  $a$ . The left and right radii of the apparent scattering volume are  $d_1$  and  $d_2$  and the radii of the actual scattering volume are  $d'_1$  and  $d'_2$ . Finally,  $\theta_1$  is the angle of refraction of the marginal ray defined by the pinhole.

Approximating the shape of the scattering volume as a cylindrical cone with its apex cut off, the apparent scattering volume is easily derived using a triple integral and is given by,

$$V_{\text{app}} = \frac{1}{3}\pi w (d_1^2 + d_1 d_2 + d_2^2) \quad (\text{B.1})$$

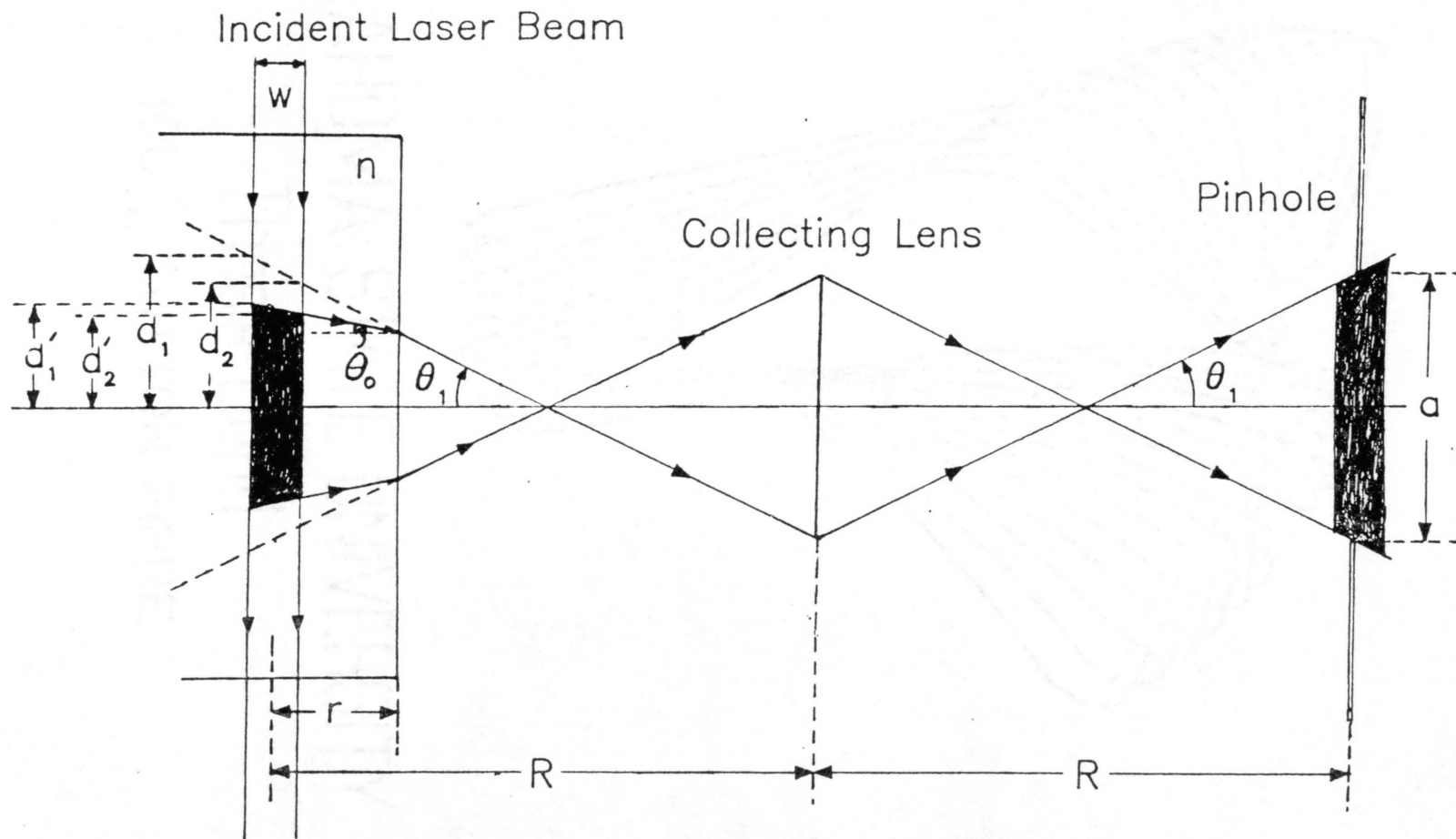


Figure 17. Top View of the Scattering Volume.



Referring to Figure 17 and keeping in mind that the scattering volume is two focal lengths from the collecting lens (i.e. the object distance equals the image distance which in turn equals twice the focal length), we see that  $\theta_1$  can be expressed in a number of ways,

$$\begin{aligned}\theta_1 &= \tan^{-1}\left(\frac{a}{R}\right) \approx \frac{a}{R} \\ \theta_1 &= \tan^{-1}\left[\frac{d_1}{\frac{1}{2}(R+w)}\right] \approx \frac{2d_1}{R} \\ \theta_1 &= \tan^{-1}\left[\frac{d_2}{\frac{1}{2}(R-w)}\right] \approx \frac{2d_2}{R}\end{aligned}\quad (\text{B.2})$$

Using these three expressions for  $\theta_1$ ,  $d_1$  and  $d_2$  become,

$$\begin{aligned}d_1 &= \frac{a}{2R}(R+w) \approx \frac{a}{2} \\ d_2 &= \frac{a}{2R}(R-w) \approx \frac{a}{2}\end{aligned}\quad (\text{B.3})$$

The apparent volume Equation (B.1) is then,

$$V_{\text{app}} = \frac{1}{4}w\pi a^2, \quad (\text{B.4})$$

To calculate the actual scattering volume we need expressions for  $d_1'$  and  $d_2'$ . Using Equation (B.3) we see that,

$$d_1 - d_1' = \frac{a}{2R}(R+w) - d_1' \quad (\text{B.5})$$

also from Figure 17,

$$d_1 - d_1' = \theta_1\left(r + \frac{W}{2}\right) - \theta_0\left(r + \frac{W}{2}\right) \quad (\text{B.6})$$

where  $\theta_0$  is the angle of incidence of the marginal ray defined by the collecting lens. Now  $\theta_0$  and  $\theta_1$  are related to each other through Snell's law for small angles,

$$\theta_0 = \frac{\theta_1}{n} \quad (\text{B.7})$$

Putting the first expression in Equation (B.2) and Equation (B.7) into Equation (B.6) and then equating the right hand sides of Equations (B.5) and (B.6), we arrive at an expression for  $d'_1$ ,

$$\begin{aligned} d'_1 &= \left(\frac{a}{R}\right) \left[ \frac{1}{2}(R+w) - \frac{n-1}{n} \left(r + \frac{w}{2}\right) \right] \\ &\approx \left(\frac{a}{R}\right) \left[ \frac{1}{2}R - \frac{n-1}{n} \left(r + \frac{w}{2}\right) \right] . \end{aligned} \quad (\text{B.8})$$

In a similar way  $d'_2$  is given by,

$$\begin{aligned} d'_2 &= \left(\frac{a}{R}\right) \left[ \frac{1}{2}(R-w) - \frac{n-1}{n} \left(r - \frac{w}{2}\right) \right] \\ &\approx \left(\frac{a}{R}\right) \left[ \frac{1}{2}R - \frac{n-1}{n} \left(r - \frac{w}{2}\right) \right] \end{aligned} \quad (\text{B.9})$$

Inserting Equations (B.8) and (B.9) into the expression for the volume Equation (B.1) and keeping only the first order terms, the actual volume becomes,

$$\begin{aligned} V &\approx V_{\text{app}} + \Delta V \\ V &\approx \frac{1}{4} w \pi a^2 - \left(\frac{r}{R}\right) w \pi a^2 \frac{(n-1)}{n} \end{aligned} \quad (\text{B.10})$$

The second term on the right hand side of Eq. (B.10) is an approximation for the correction to the scattering volume as a result of the refraction of the scattered light as it leaves the sample. The square root of the ratio of the scattering volume of fused quartz to that of the samples is the quantity that appears in the expression for the photo-elastic constants. In view of the above

discussion, this quantity becomes,

$$\left(\frac{V^0}{V}\right)^{\frac{1}{2}} = \left(\frac{V_{app} + \Delta V^0}{V_{app} + \Delta V}\right)^{\frac{1}{2}} \approx \frac{1 + 2\left(\frac{r}{R}\right)\frac{(n^0 - 1)}{n^0}}{1 + 2\left(\frac{r}{R}\right)\frac{(n - 1)}{n}} \quad (\text{B.11})$$

Where the quantities that have a superscript "o" are the fused quartz quantities.

Table XVIII lists the values of this ratio for the different glass samples where we have used  $r = 0.2\text{cm}$  and  $R = 10.5\text{cm}$ . As one can see, the ratio is very nearly equal to one for all of the samples.

#### Solid Angle Correction

Figure 18 shows a top view of the sample with the laser beam incident from the top of the figure.  $\theta_2$  is the angle of incidence between the optic axis and the marginal ray defined by the collecting lens of radius  $h$ .  $\theta_3$  is the angle between the optic axis and the imaginary line extending from a point within the scattering volume to the periphery of the collecting lens and  $\theta_4$  is the angle of refraction for the marginal ray.  $R$  is the distance from the point of scattering to the collecting lens and  $r$  is the distance from the scattering point to the front surface of the sample.

For small angles the tangents and the sines of the angles are approximately equal to the angles themselves. With this in mind, we can write,

TABLE XVIII  
CORRECTION FACTORS

Sample	n	$\left(\frac{V+\Delta V^0}{V+\Delta V}\right)^{1/2}$	$\left(\frac{n}{n^0}\right)^2$	$\gamma$	$\phi_1$ (degrees)
Li <sub>2</sub> O-SiO <sub>2</sub>	1.604	0.9977	1.204	1.017	4.618
Na <sub>2</sub> O-SiO <sub>2</sub>	1.583	0.9980	1.172	1.026	4.679
K <sub>2</sub> O-SiO <sub>2</sub>	1.584	0.9980	1.174	1.031	4.676
Rb <sub>2</sub> O-SiO <sub>2</sub>	1.572	0.9982	1.156	1.004	4.712
Cs <sub>2</sub> O-SiO <sub>2</sub>	1.591	0.9979	1.184	1.032	4.656
SiO <sub>2</sub>	1.462				5.066

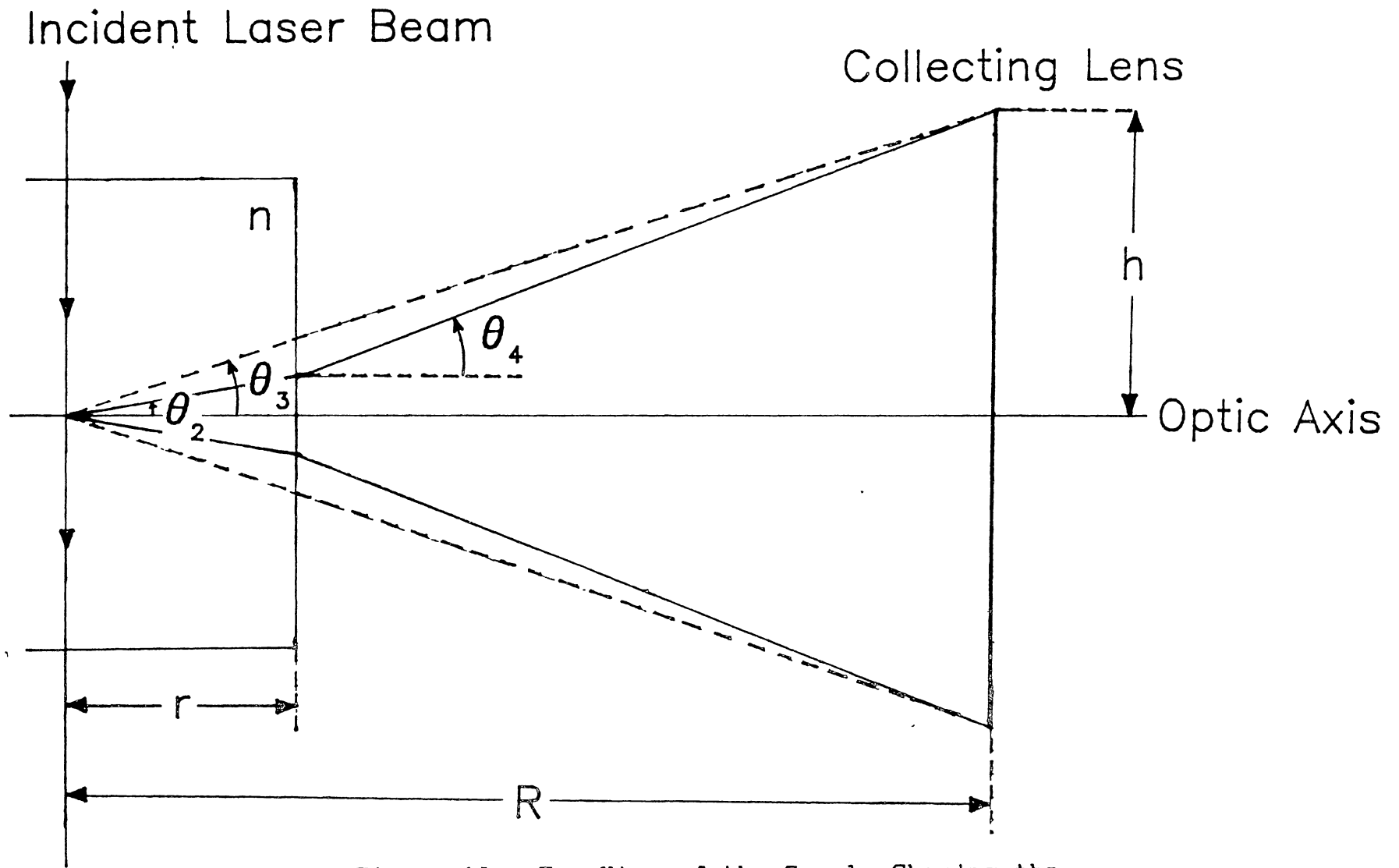


Figure 18. Top View of the Sample Showing the Collection Solid Angle.

$$R\theta_3 = r\theta_2 + (R-r)\theta_4$$

and

$$n\theta_2 = \theta_4 \quad (\text{B.12})$$

Solving for  $\theta_2$  we have,

$$\theta_2 = \frac{\theta_3}{\left[ n - \frac{r(n-1)}{R} \right]} \quad (\text{B.13})$$

This is the expression for the maximum angle, from the optic axis, for the bundle of rays leaving the scattering volume and still making it through the collecting lens. Any ray that leaves the point of scattering with an angle larger than  $\theta_2$  will not pass through the collecting lens.  $\theta_2$  clearly depends on the index of refraction of the sample. The larger the index of refraction, the smaller the amount of light that makes it through to the collecting lens.

The scattered intensity at the collecting lens is equal to the scattered power per unit area across the collecting lens. The ratio of the scattered intensity of the sample to that of fused quartz is proportional to,

$$\begin{aligned} \frac{I_S}{I_S^0} &\propto \frac{1/A}{1/A^0} = \frac{A^0}{A} \\ &= \left( \frac{\theta_2^0}{\theta_2} \right)^2 \end{aligned} \quad (\text{B.14})$$

where  $A = \pi h^2 \approx \pi R^2 \theta_2^2$  and  $A^0 \approx \pi R^2 (\theta_2^0)^2$ .

Using Equation (B.13), this ratio becomes,

$$\begin{aligned} \left( \frac{\theta_1^0}{\theta_1} \right)^2 &= \frac{\left[ n - \frac{r(n-1)}{R} \right]^2}{\left[ n^0 - \frac{r(n^0-1)}{R} \right]^2} \\ &\approx \left( \frac{n}{n^0} \right)^2 \end{aligned} \quad (\text{B.15})$$

As a result of the above solid angle correction the intensity ratio  $\beta$  that appears in Equation (3.25) becomes,

$$\beta = \beta_{\text{meas.}} \left( \frac{n}{n_0} \right)^2 \quad (\text{B.16})$$

That is, the actual intensity ratio is larger than that which is measured due to the fact that the refraction of the scattered light, as it leaves the sample, is greater for the glass samples than it is for fused quartz as a result of the relatively low index of refraction of fused quartz. This means that less light is received by the collecting lens from the glass samples compared to fused quartz than would be expected if the effects of refraction were the same for both materials.

#### Back-Reflection

When a laser beam is normally incident on the surface of polished glass, a small fraction of the incident intensity is reflected and the rest is transmitted. There is an additional reflection at the inside surface where the laser beam exits the material. If the entrance and exit surfaces are parallel, this back reflection contributes to the intensity of the laser beam within the sample. Furthermore, this contribution of the back-reflection nearly compensates for that fraction of the incident light lost due to reflection at the entrance surface. If the incident intensity is  $I_0$ , then the

transmitted intensity is  $TI_0$ , where  $T$  is the transmittance. The fraction of laser light, within the sample, that is reflected at the exit surface is  $RTI_0$ , where  $R$  is the reflectance. The total intensity inside the sample is the sum of these two quantities,

$$TI_0 + RTI_0 = I_0 T(1+R) \quad (\text{B.17})$$

If we take typical values for  $T$  and  $R$  of about 0.95 and 0.05 respectively, we find that the intensity inside the glass is  $0.998I_0 \approx I_0$ .

The above represents the situation in fused quartz. However, in those samples that are absorbing, the back-reflection does not compensate nearly as well for the fraction of light lost at the entrance surface. Referring to a coordinate system where the origin is located at the point where the laser beam enters the glass, the intensity of the laser beam is,

$$\begin{aligned} I(0, z) &= TI_0 (e^{-\alpha z} + R e^{-2\alpha L} e^{\alpha z}) \\ &= TI_0 e^{-\alpha z} (1 + R e^{2\alpha(z-L)}) \end{aligned} \quad (\text{B.18})$$

where  $z$  is the distance traveled by the laser beam through the sample,  $\alpha$  is the absorption coefficient and  $L$  is the length of the sample. Note that Equation (B.18) reduces to Equation (B.17) in the case  $\alpha = 0$ .

Since the scattered intensity is proportional to the intensity of the laser beam given by Equation (B.18), we can take the ratio of the intensity of the laser beam



inside the glass to that inside fused quartz in the limit as  $z \rightarrow 0$ ,

$$\frac{I}{I^0} \propto \frac{[1 + R e^{-2\alpha L}]}{[1 + R^0 e^{-2\alpha^0 L^0}]} \quad (\text{B.19})$$

In the above equation, we have not included the ratio of the transmittances as this was taken into account in Chapter III.

Since the absorption of the light in the high absorption glasses serves to reduce the intensity of the laser beam inside the material, we would expect the measured intensity ratio to be less than would be expected if absorption was not taking place. Thus, to cancel out the effects of absorption we need to multiply the measured intensity ratio  $\beta$  by the reciprocal of Equation (B.19),

$$\beta = \beta_{\text{meas.}} \gamma \quad (\text{B.20})$$

where,

$$\gamma = \frac{[1 + R^0 e^{-2\alpha^0 L^0}]}{[1 + R e^{-2\alpha L}]} \quad (\text{B.21})$$

Values of  $\gamma$  for the different samples are listed in Table XVIII. In most cases  $\gamma$  is on the order of about 3% of the measured value of  $\beta$ .

#### Uncertainty in the Velocity

The phonon wave velocity in terms of the Brillouin shift  $\Delta\omega$  is given by,

$$v = \frac{\lambda_0 c \Delta\omega}{2n \sin \frac{\phi}{2}} \quad (\text{B.22})$$

where  $c$  is the speed of light,  $n$  the index of refraction and  $\lambda_0$  the laser wavelength. The velocity clearly depends on the scattering angle  $\phi$ . In our experiments this angle is equal to  $90^\circ$ . However, as we have seen in the last few sections, the finite size of the collecting lens leads to a solid angle of rays emanating from the scattering volume. As a result, there is an uncertainty in the velocity due to this range of angles.

Using standard error analysis procedures, the fractional uncertainty in the velocity due to measurement errors is given by

$$\frac{\Delta v}{v} = \frac{\Delta(\Delta\omega)}{\Delta\omega} - \frac{\Delta n}{n} - \frac{\cos\frac{\phi}{2}}{2\sin\frac{\phi}{2}}\Delta\phi \quad (\text{B.23})$$

In order to evaluate this expression we need, in addition to the other values,  $\Delta\phi$ .

Figure 19 shows a top view of the sample with the laser beam incident from the top of the figure.  $L_1$  is the collecting lens of focal length  $f_1$ ,  $L_2$  the collimating lens with focal length  $f_2$  and PH is the pinhole. The Fabry-Perot triple pass entrance is shown at the right with radius  $a$ . The angle  $\phi_2$  is the angle of refraction of the marginal ray defined by the Fabry-Perot opening and is given by,

$$\phi_2 = \tan^{-1}\left(\frac{b}{f_2}\right) \approx \frac{b}{f_2} \quad (\text{B.24})$$

$\phi_1$  is the angle of incidence of the marginal ray and is related to  $\phi_2$  by Snell's law for small angles,

$$\phi_1 \approx \frac{\phi_2}{n} \quad (\text{B.25})$$

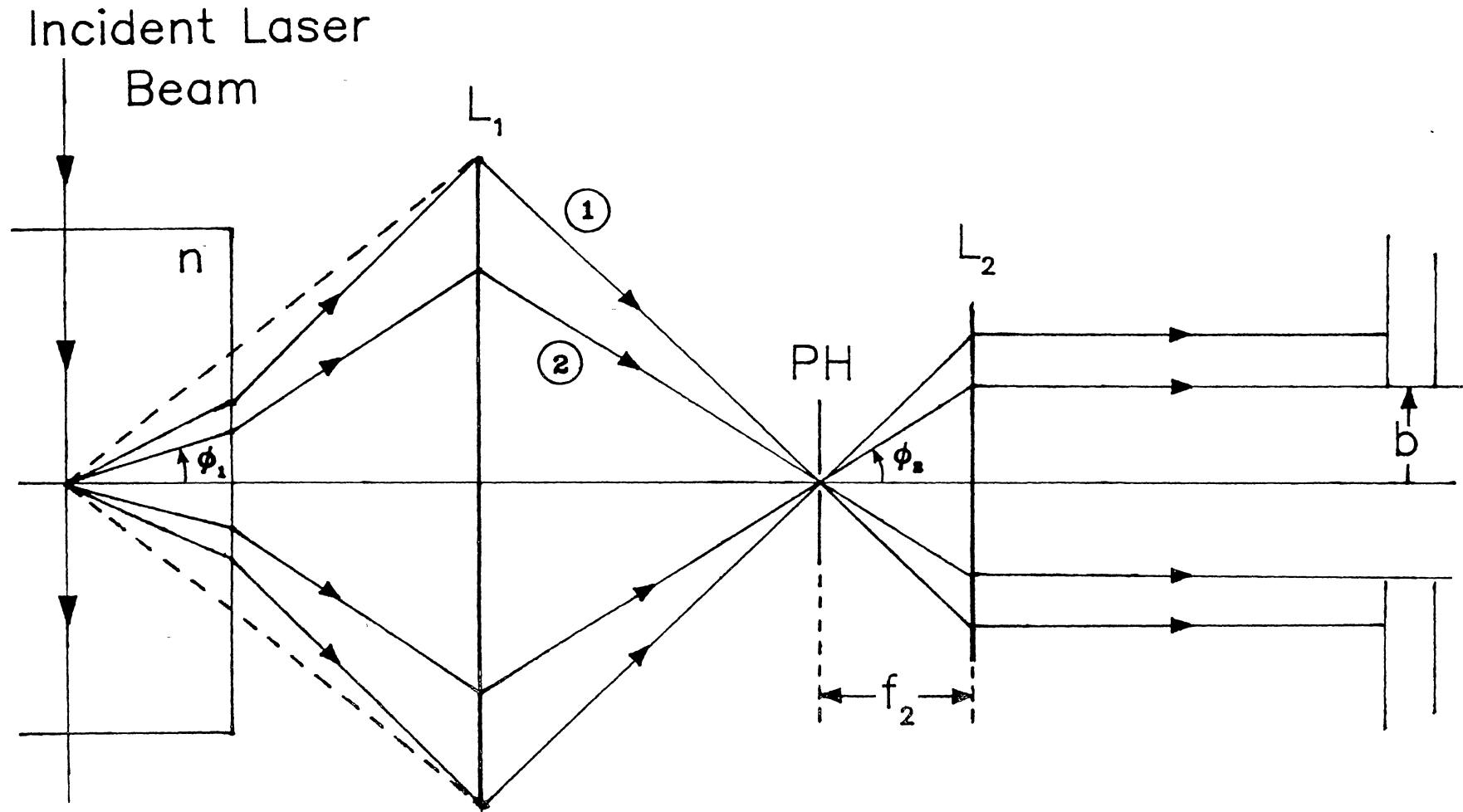


Figure 19. The Top View of the Sample for the Calculation of the Uncertainty in the Velocity.

Values of  $\phi_1$  for the glass samples are given in Table XVIII. The largest value is 4.7 degrees for  $\text{Rb}_2\text{O-SiO}_2$ . Converting this to radians, we have for the maximum uncertainty in the scattering angle  $\phi$ ,

$$\Delta\phi \approx \pm 0.082\text{rad} \quad (\text{B.26})$$

Comparing this with the fractional uncertainty in the index of refraction and the Brillouin shift, we see that  $\Delta\phi$  contributes the most to the uncertainty in the velocity.

VITA

George H. Gangwere

Candidate for the Degree of

Doctor of Philosophy

Thesis: BRILLOUIN SCATTERING IN  $\text{EU}^{3+}$ -DOPED  
ALKALI-SILICATE GLASSES

Major Field: Physics

Biographical:

Personal Data: Born in Kansas City, Missouri, January 10, 1948, the son of George H. and Blanche M. Gangwere.

Education: Received Bachelor of Science Degree in Physics and Mathematics from Southwest Missouri State University in Springfield, Missouri in May, 1976; received Master of Science Degree in Experimental Physics from Kansas State University in Manhattan, Kansas in December, 1981; completed requirements for Doctor of Philosophy degree in Experimental Physics at Oklahoma State University in December, 1990.

Professional Experience: Teaching Assistant, Department of Physics, Southwest Missouri State University, August 1976 to July 1977. Graduate Teaching Assistant, Department of Physics, Kansas State University, August 1977 to December 1980. Graduate Research Assistant, Department of Physics, Kansas State University, June 1979 to July 1980. Instructor and Head of Physics Department, Southwestern College, Winfield, Kansas, August 1980 to 1984. Head Tennis Coach for the men's team, Southwestern College, August 1983 to May 1985. Assistant Professor and Head of Physics Department, Southwestern College, August 1984 to 1985. Graduate Teaching Assistant, Oklahoma State University, Stillwater, Oklahoma, August 1985 to December 1986. Graduate Research Assistant, Oklahoma State University,

January 1987 to July 1989. Assistant Professor  
of Mathematics and Physics, Southwestern College,  
August 1989 to present.